

Understanding the Influence of Moisture on Fingerpad-Surface Interactions

Understanding the Influence of Moisture on Fingerpad-Surface Interactions

Dissertation

der Mathematisch-Naturwissenschaftlichen Fakultät

der Eberhard Karls Universität Tübingen

zur Erlangung des Grades eines

Doktors der Naturwissenschaften

(Dr. rer. nat.)

vorgelegt von

M.Sc. Saekwang Nam

aus Daegu/Südkorea

Tübingen

2022

Gedruckt mit Genehmigung der Mathematisch-Naturwissenschaftlichen Fakultät der
Eberhard Karls Universität Tübingen.

Tag der mündlichen Qualifikation:

12. Oktober 2022

Dekan:

Prof. Dr. Thilo Stehle

1. Berichterstatterin:

Dr. Katherine J. Kuchenbecker

2. Berichterstatter:

Prof. Dr. Martin A. Giese

Abstract

People frequently touch objects with their fingers. The physical deformation of a finger pressing an object surface stimulates mechanoreceptors, resulting in a perceptual experience. Through interactions between perceptual sensations and motor control, humans naturally acquire the ability to manage friction under various contact conditions. Many researchers have advanced our understanding of human fingers to this point, but their complex structure and the variations in friction they experience due to continuously changing contact conditions necessitate additional study. Moisture is a primary factor that influences many aspects of the finger. In particular, sweat excreted from the numerous sweat pores on the fingerprints modifies the finger's material properties and the contact conditions between the finger and a surface. Measuring changes of the finger's moisture over time and in response to external stimuli presents a challenge for researchers, as commercial moisture sensors do not provide continuous measurements.

This dissertation investigates the influence of moisture on fingerpad-surface interactions from diverse perspectives. First, we examine the extent to which moisture on the finger contributes to the sensation of stickiness during contact with glass. Second, we investigate the representative material properties of a finger at three distinct moisture levels, since the softness of human skin varies significantly with moisture. The third perspective is friction; we examine how the contact conditions, including the moisture of a finger, determine the available friction force opposing lateral sliding on glass. Fourth, we have invented and prototyped a transparent *in vivo* moisture sensor for the continuous measurement of finger hydration.

In the first part of this dissertation, we explore how the perceptual intensity of light stickiness relates to the physical interaction between the skin and the surface. We conducted a psychophysical experiment in which nine participants actively pressed their index finger on a flat glass plate with a normal force close to 1.5 N and then detached it after a few seconds. A custom-designed apparatus recorded the contact force vector and the finger contact area during each interaction as well as pre- and post-trial finger moisture. After detaching their finger, participants judged the stickiness of the glass using a nine-point scale. We explored how sixteen physical variables derived from the recorded data correlate with each other and with the stickiness judgments of each participant. These analyses indicate that stickiness perception mainly depends on the pre-detachment pressing duration, the time taken for the finger to detach, and the impulse in the normal direction after the normal force changes sign; finger-surface adhesion seems to build with pressing time, causing a larger normal impulse during detachment and thus a more intense stickiness sensation. We additionally found a strong between-subjects correlation

between maximum real contact area and peak pull-off force, as well as between finger moisture and impulse.

When a fingerpad presses into a hard surface, the development of the contact area depends on the pressing force and speed. Importantly, it also varies with the finger's moisture, presumably because hydration changes the tissue's material properties. Therefore, for the second part of this dissertation, we collected data from one finger repeatedly pressing a glass plate under three moisture conditions, and we constructed a finite element model that we optimized to simulate the same three scenarios. We controlled the moisture of the subject's finger to be dry, natural, or moist and recorded 15 pressing trials in each condition. The measurements include normal force over time plus finger-contact images that are processed to yield gross contact area. We defined the axially symmetric 3D model's lumped parameters to include an SLS-Kelvin model (spring in series with parallel spring and damper) for the bulk tissue, plus an elastic epidermal layer. Particle swarm optimization was used to find the parameter values that cause the simulation to best match the trials recorded in each moisture condition. The results show that the softness of the bulk tissue reduces as the finger becomes more hydrated. The epidermis of the moist finger model is softest, while the natural finger model has the highest viscosity.

In the third part of this dissertation, we focused on friction between the fingerpad and the surface. The magnitude of finger-surface friction available at the onset of full slip is crucial for understanding how the human hand can grip and manipulate objects. Related studies revealed the significance of moisture and contact time in enhancing friction. Recent research additionally indicated that surface temperature may also affect friction. However, previously reported friction coefficients have been measured only in dynamic contact conditions, where the finger is already sliding across the surface. In this study, we repeatedly measured the initial friction before full slip under eight contact conditions with low and high finger moisture, pressing time, and surface temperature. Moisture and pressing time both independently increased finger-surface friction across our population of twelve participants, and the effect of surface temperature depended on the contact conditions. Furthermore, detailed analysis of the recorded measurements indicates that micro stick-slip during the partial-slip phase contributes to enhanced friction.

For the fourth and final part of this dissertation, we designed a transparent moisture sensor for continuous measurement of fingerpad hydration. Because various stimuli cause the sweat pores on fingerprints to excrete sweat, many researchers want to quantify the flow and assess its impact on the formation of the contact area. Unfortunately, the most popular sensor for skin hydration is opaque and does not offer continuous measurements. Our capacitive moisture sensor consists of a pair of inter-digital electrodes covered by an insulating layer, enabling impedance measurements across a wide frequency range. This proposed sensor is made entirely of transparent materials, which allows us to simultaneously measure the finger's contact area. Electrochemical impedance spectroscopy identifies the equivalent electrical circuit and the electrical component parameters that are affected by the amount of moisture present on the surface of the sensor. Most notably, the impedance at 1 kHz seems to best reflect the relative amount of sweat.

Zusammenfassung

Menschen berühren Objekte häufig mit ihren Fingern. Die physikalische Verformung eines Fingers, der auf die Oberfläche eines Objekts drückt, stimuliert die Mechanorezeptoren und führt zu einer Wahrnehmung. Durch die Interaktion zwischen den Wahrnehmungen und der motorischen Kontrolle erwirbt der Mensch auf natürliche Weise die Fähigkeit, die Reibung unter verschiedenen Kontaktbedingungen zu steuern. Zahlreiche Forscher haben unser Verständnis über menschliche Finger bislang vorangetrieben, aber die komplexe Struktur des Fingers und die Variationen der Reibung, aufgrund von sich ständig ändernden Kontaktbedingungen, machen weitere Studien erforderlich. Feuchtigkeit ist ein wichtiger Faktor, der viele Aspekte des Fingers beeinflusst. Insbesondere der Schweiß, der aus den zahlreichen Schweißporen der Fingern austritt, verändert die Materialeigenschaften des Fingers und die Kontaktbedingungen zwischen dem Finger und einer Oberfläche. Die Messung von zeitlichen Veränderungen der Feuchtigkeit des Fingers durch äußere Anregung stellt für Forscher eine Herausforderung dar, da kommerzielle Feuchtigkeitssensoren keine kontinuierlichen Messungen liefern.

In dieser Dissertation wird der Einfluss der Feuchtigkeit auf die Interaktion zwischen Finger und Oberfläche aus verschiedenen Perspektiven untersucht. Erstens untersuchen wir, inwieweit die Feuchtigkeit auf dem Finger zu dem Gefühl der Klebrigkeit beim Kontakt mit Glas beiträgt. Zweitens untersuchen wir die repräsentativen Materialeigenschaften eines Fingers bei drei verschiedenen Feuchtigkeitsstufen, da die Weichheit der menschlichen Haut je nach Feuchtigkeit stark variiert. Die dritte Perspektive ist die Reibung. Wir untersuchen, wie die Kontaktbedingungen, einschließlich der Feuchtigkeit eines Fingers, die vorhandene Reibungskraft bestimmen, die aus dem seitlichen Gleiten auf Glas resultiert. Viertens haben wir einen transparenten In-vivo-Feuchtigkeitssensor für die kontinuierliche Messung der Feuchtigkeit auf dem Finger entwickelt und als Prototyp realisiert.

Im ersten Teil dieser Dissertation untersuchen wir, wie die wahrgenommene Intensität geringer Klebrigkeit mit der physikalischen Interaktion zwischen der Haut und der Oberfläche zusammenhängt. Wir haben ein psychophysisches Experiment durchgeführt, bei dem neun Teilnehmer ihren Zeigefinger aktiv mit einer Normalkraft von etwa 1,5 N auf eine flache Glasplatte drückten und ihn dann nach einigen Sekunden wieder abnahmen. Ein speziell entwickelter Apparat zeichnete die vektorielle Kontaktkraft und die Kontaktfläche des Fingers während jeder Interaktion sowie die Feuchtigkeit des Fingers vor und nach dem Versuch auf. Nachdem die Teilnehmer ihren Finger abgenommen hatten, beurteilten sie die Klebrigkeit des Glases anhand einer Neun-Punkte-Skala. Wir untersuchten die wechselseitige Beziehung von sechzehn physikalischen Variablen, die

aus den aufgezeichneten Daten abgeleitet wurden, und korrelierten diese mit den Einschätzungen der Klebrigkeit von den einzelnen Teilnehmern. Diese Analysen deuten darauf hin, dass die Wahrnehmung der Klebrigkeit vor allem von der Dauer des Drucks vor dem Ablösen, der Zeit, die der Finger zum Ablösen benötigt, und dem Impuls in der normalen Richtung nach dem Vorzeichenwechsel der normalen Kraft abhängt; es scheint so, dass die Adhäsion der Fingeroberfläche mit der Dauer des Drucks zunimmt, was zu einem größeren normalen Impuls während des Ablösens und damit zu einem intensiveren Klebegefühl führt. Außerdem fanden wir unter den Probanden eine starke Korrelation zwischen der maximalen realen Kontaktfläche und der maximalen Abziehungskraft sowie zwischen der Feuchtigkeit auf dem Finger und dem Impuls.

Beim Drücken einer harten Oberfläche durch ein Fingerkuppe ist die Entwicklung der Kontaktfläche abhängig von der Druckkraft und Geschwindigkeit. Wichtig ist, dass Kontaktfläche auch mit der Feuchtigkeit des Fingers variiert, vermutlich weil die Hydratation die Materialeigenschaften des Gewebes verändert. Für den zweiten Teil dieser Dissertation haben wir daher Daten von einem Finger gesammelt, der wiederholt unter drei Feuchtigkeitsbedingungen auf eine Glasplatte drückte. Wir haben ein Finite-Elemente-Modell konstruiert, welches wir optimiert haben, um die entsprechenden drei Szenarien zu simulieren. Wir stufen die Feuchtigkeit des Fingers jeder Testperson als entweder trocken, natürlich oder feucht ein und zeichneten fünfzehn Druckversuche unter jeder Bedingung auf. Die Messungen beinhalteten die Normalkraft über die Zeit sowie Bilder des Fingerkontakts, die verarbeitet wurden, um die Gesamtkontaktfläche zu ermitteln. Wir haben die Parameter des axial-symmetrischen 3D-Modells so definiert, dass sie ein SLS-Kelvin-Modell (Feder in Serie mit paralleler Feder und Dämpfer) für das Hauptgewebe sowie eine elastische Epidermisschicht umfassen. Mit Hilfe der Partikelschwarm-Optimierung wurden die Parameterwerte ermittelt, die die Simulation am besten mit den in den einzelnen Feuchtigkeitszuständen aufgezeichneten Versuchen übereinstimmen lassen. Die Ergebnisse zeigen, dass die Weichheit des Hauptgewebes mit zunehmender Feuchtigkeit des Fingers abnimmt. Die Epidermis des feuchten Fingermodells ist am weichsten, während das natürliche Fingermodell die höchste Viskosität aufweist.

Im dritten Teil dieser Dissertation konzentrierten wir uns auf die Reibung zwischen der Fingerkuppe und der Oberfläche. Das Ausmaß der Reibung zwischen Finger und Oberfläche, die zu Beginn des vollständigen Rutschens vorhanden ist, ist entscheidend für das menschliche Verständnis vom Greifen und Manipulieren von Objekten. Ähnliche Studien haben gezeigt, dass Feuchtigkeit und Kontaktzeit die Reibung verstärken. Aktuelle Forschungen haben außerdem gezeigt, dass die Oberflächentemperatur ebenfalls die Reibung beeinflussen kann. Die bisher berichteten Reibungskoeffizienten wurden jedoch nur unter dynamischen Kontaktbedingungen gemessen, bei denen der Finger bereits über die Oberfläche gleitet. In dieser Studie haben wir wiederholt die initiale Reibung vor dem vollständigen Gleiten unter acht Kontaktbedingungen mit niedriger und hoher Fingerfeuchtigkeit, Presszeit und Oberflächentemperatur gemessen. Sowohl die Feuchtigkeit als auch die Presszeit erhöhten unabhängig voneinander die Reibung zwischen Finger und Oberfläche bei unseren zwölf Teilnehmern, und die Wirkung der Oberflächen-

temperatur war abhängig von der Kontaktbedingungen. Eine detaillierte Analyse der aufgezeichneten Messungen deutet außerdem darauf hin, dass Mikro-Stick-Slip Bewegungen während der partiellen Gleitphase zur erhöhten Reibung beiträgt.

Für den vierten und letzten Teil dieser Dissertation haben wir einen transparenten Feuchtigkeitssensor für die kontinuierliche Messung der Hydratation der Fingerkuppe entwickelt. Da die Schweißporen auf den Fingerabdrücken durch verschiedene Reize zur Schweißabsonderung veranlasst werden, möchten viele Forscher diesen Fluss quantifizieren und seine Auswirkungen auf die Bildung der Kontaktfläche bewerten. Leider ist der gängige Sensor für die Hautfeuchtigkeit undurchsichtig und bietet keine kontinuierlichen Messungen. Unser kapazitiver Feuchtigkeitssensor besteht aus einem Paar interdigitaler Elektroden, die von einer isolierenden Schicht bedeckt sind und Impedanzmessungen über einen breiten Frequenzbereich ermöglichen. Der vorgeschlagene Sensor besteht vollständig aus transparenten Materialien, was es uns ermöglicht, gleichzeitig die Kontaktfläche des Fingers zu messen. Die elektrochemische Impedanzspektroskopie identifiziert das elektrische Ersatzschaltbild und die Parameter der elektrischen Komponenten, die von der Feuchtigkeitsmenge auf der Oberfläche des Sensors beeinflusst werden. Vor allem die Impedanz bei 1 kHz scheint die jeweilige Menge an Schweiß am besten widerzuspiegeln.

Acknowledgments

First and foremost, I would like to express my gratitude to my Ph.D. advisor, Katherine J. Kuchenbecker, for her selfless mentoring and dedication to her students. Every two weeks for nearly five years, she had a research meeting with me for at least forty-five minutes. During my initial period at MPI-IS, I met with her even more frequently. Her enthusiasm for research and desire to assist me and my studies impressed me. Moreover, I believe that her emphasis on soft skills, such as strengthening my English, giving clear presentations, communication, and formal paper writing, has made me a much better researcher than I was before starting this long journey.

I would like to express my special thanks to Martin A. Giese. As a member of the first generation of IMPRS-IS, my Ph.D. program at MPI-IS, I was unsure how to find my advisor on the university side, but he generously agreed to serve as my advisor. He had to make multiple trips from Tübingen to Stuttgart for my thesis advisory committee (TAC) meetings, for which I am truly grateful.

I would also like to thank Peer Fischer and Metin Sitti for their guidance as the other members of my IMPRS-IS TAC. Particularly, Metin Sitti kindly permitted me to speak with his research technicians about lithography. In addition, they allowed me to use their workstations for my research, which was connected to the paper acceptance and an award subsequently. When one of my studies was stuck, Peer Fischer was nice enough to meet with me in person. I appreciated his scientific approach to finding the scientific problem we had and his subsequent recommendations.

I could not have reached this stage without the encouragement of my darling wife, Hyemin Choi. She temporarily stopped her career, married, and moved to Germany with me. Although we have enjoyed living in Stuttgart, it may have been difficult for her to wait nearly five years for my degree and listen to my academic struggles. Moreover, in contrast to my promise to make her happy and wealthy, I had to work late almost every day for a limited payment. Having our precious Jihoo last year was my greatest pleasure in these difficult circumstances. Without you, no joyful memories could have been created. I love you.

I am grateful for the unconditional support of my parents (Chaewon Nam and Giyoung Lim) and in-laws (Byeongseop Choi and Sunog Lee). They have prayed for my success and encouraged my wife and me in numerous ways. Although it was not my fault, I regret that I could not take them to European tourist attractions due to the spread of COVID-19. I hope for another opportunity before leaving Europe.

My doctoral research was supported by the Max Planck Society and IMPRS-IS. Because it is not simple to support someone financially without expecting an economic re-

turn, I appreciate their philosophy and decision to support me for a long period of time. I would never have had such freedom to conduct research anywhere else. In addition, I am very grateful to Leila Masri and Sara Sorce for their tireless efforts in operating the IMPRS-IS Ph.D. program.

I do not believe I could have managed such a long and stressful doctoral period without the support of numerous Korean friends in Stuttgart. Sure Bak and Woojin Suh often invited my wife and me to their home and listened to our difficulties. Hyunhee Lee sincerely had hoped for our baby, who was later born and named Jihoo. Hyunjin Lim, her husband, led regular prayer meetings and helped us feel the mercy and grace of God. He also edited the German abstract of this dissertation. Furthermore, my wife and I truly want to thank the Lee family (Whan Lee, Su Ran Suk, Yul Lee, and Lila Lee) for their kind welcome whenever we visit Frankfurt. Beyond these wonderful individuals, I also express my gratitude to many other people I have met in Nambugemeinde, MPI-FKF, and MPI-IS.

I wish to express my gratitude to every member of the Haptic Intelligence Department. I could not conduct good research without their assistance and support. Particularly, Hyosang, who sat next to me in the lab and spent nearly four years with me, patiently listened to my research ideas and questions. Ben was my exercise and conversation mate during lunchtime. Paola, Bernard, Mayumi, and Ilona were always kind to me in various aspects, and Behnam, one of my office mates, also read and edited the German abstract of my dissertation.

And lastly, this dissertation could not have been finished without the cooperation of several other close colleagues. The following are the acknowledgments for each of the four research chapters in this dissertation:

- **Chapter 3:** I appreciate the significant contributions made by Yasemin Vardar, David Gueorguiev, and Katherine J. Kuchenbecker, who are the three co-authors of the published paper associated with this chapter. They helped to design the psychophysical experiment, gave input on data analysis, guided the creation of the figures, wrote short sections of text, and extensively edited the manuscript. Additionally, Katherine Kuchenbecker gave input on the apparatus design and supervised the project. Next, I thank Bernard Javot for support in building the apparatus, Maria-Paola Forte for suggestions about camera calibration, and Cem Balda Dayan and Dongha Tahk for helping attach the prism to the glass plate using PDMS. I also thank Hua-Chun Sun and Marie-Ange Bueno for reviewing our published manuscript and Sung-Phil Kim for editing this manuscript.
- **Chapter 4:** I thank Mayumi Mohan and Hyunkyung Park for their ideas about the possible optimization methods. I would also like to thank Metin Sitti and Peer Fischer for allowing the use of their workstations for computational studies in this chapter. Lastly, I appreciate the work of my co-author Katherine Kuchenbecker on guiding the research, plots, and writing reported in this chapter and the asso-

ciated paper. Lastly, I am grateful for the anonymous reviewers' contributions to improving this manuscript.

- **Chapter 5:** I first would like to show my gratitude to David Gueorguiev and Katherine Kuchenbecker. They contributed to the design of the human subject study and provided input on the analysis methodologies and data interpretations for this chapter. Furthermore, Katherine Kuchenbecker read and edited this chapter. Additionally, I would like to thank Bernard Javot for building the heating system with the Peltier element and a protection case for the entire apparatus. Lastly, Maria-Paola Forte gave helpful comments on tracking interest points, Mayumi Mohan commented about the statistical tests, and Peer Fischer shared his thoughts about designing the experiment.
- **Chapter 6:** I thank Joachim Gräfe, Gunther Richter, and Katherine J. Kuchenbecker. Joachim Gräfe allowed me to use his laboratory facilities and taught me how to use direct laser lithography, a sputtering system, and a wire bonder. He transferred his know-how and knowledge in laser lithography to me. Gunther Richter discussed material deposition processes and potential solutions for the ITO delamination problem. Katherine Kuchenbecker advised this research, helped me find solutions, and edited this chapter. Additionally, I would like to express my gratitude to Joachim Bill and Petia Atanasova for helping me select transparent materials. In addition, I thank Yawen Li for her excellent efforts on material deposition and its characterization. Frank Thiele contributed to the deposition of SiO₂ and ITO layers and measured sensor sample height profiles. Felix Groß and his labmates provided numerous helpful solutions to any challenges encountered with the fume hood and lithography processes. Meng Li from Zurich Instruments provided comprehensive explanations and recommendations concerning the impedance analyzer. Lastly, I would like to thank Kyungmi Lim, Jimin Oh, and Hyung-Man Cho for their extensive opinions about the theory of electrochemistry and interpretation of measured impedance.

Contents

1	Introduction	1
1.1	Outline	2
1.2	Relevant Publications and Honors	3
2	Background	5
2.1	Influence of Moisture on Stickiness Perception	5
2.2	Influence of Hydration on the Material Properties of the Finger	7
2.3	Effect of Moisture on Friction	8
2.4	Development of a Transparent Moisture Sensor	10
3	Influence of Moisture on Stickiness Perception	11
3.1	Materials and Methods	11
3.1.1	Apparatus	12
3.1.2	Participants	13
3.1.3	Ethics Statement	13
3.1.4	Experimental Procedure	13
3.1.5	Data Processing	15
3.2	Results	21
3.2.1	Physical Variables	21
3.2.2	Stickiness Perception Ratings	21
3.2.3	Correlation to Stickiness within Participants	21
3.2.4	Correlation across Participants	25
3.2.5	Effects of Frictional Forces on the Stickiness Ratings	25
3.3	Discussion	27
3.3.1	Main Perception Mechanism	27
3.3.2	Finger Size and Peak Pull-off Force	28
3.3.3	Finger Moisture and Impulse	28
3.3.4	Comparisons with Other Perceptual Studies	29
3.3.5	Experimental Limitations	29
4	Influence of Hydration on the Material Properties of the Finger	31
4.1	Methods	31
4.1.1	Data Collection	32
4.1.2	Post-processing	33
4.1.3	Finite Element Model	33

4.1.4	Parameter Search	36
4.2	Results and Discussion	36
4.2.1	Measured Gross Contact Area by Force and Time	37
4.2.2	Optimized Parameter Values	39
4.2.3	Limitations	41
5	Effect of Moisture on Friction	43
5.1	Materials and Methods	43
5.1.1	Apparatus	43
5.1.2	Capturing Fingerprint Images	45
5.1.3	Time Synchronization between Images and Forces	45
5.1.4	Extracting Contact Area from an Image	45
5.1.5	Displacement Fields and Stuck Ratios	47
5.1.6	Experimental Procedure	48
5.1.7	Ethics Statement	49
5.2	Results	50
5.2.1	Friction by Contact Conditions	50
5.2.2	Analysis between Skin Groups by Moisture	52
5.3	Discussion	56
5.3.1	Relationship between Friction and Stickiness Perception	56
5.3.2	Friction and the Surface Temperature	56
5.3.3	Importance of the Fingerprint	56
6	Development of a Transparent Moisture Sensor	57
6.1	Methods	57
6.1.1	The Design of the Sensor	57
6.1.2	Sensor Fabrication	59
6.1.3	Impedance Measurement and Circuit Optimization	62
6.1.4	Measurement with a Human Finger	63
6.2	Results	63
6.2.1	Finding the Equivalent Circuit	63
6.2.2	Impedance Measurements of a Human Finger during Pressing on the Sensor	64
6.3	Discussion	66
6.3.1	Interpretation of Optimized Parameters	66
6.3.2	Continuous Measurements	67
6.3.3	Preventing ITO from Delaminating	67
7	Conclusion	71
7.1	Summary	71
7.1.1	Influence of Moisture on Stickiness Perception	72
7.1.2	Influence of Hydration on the Material Properties of the Finger	72

7.1.3	Effect of Moisture on Friction	72
7.1.4	Development of a Transparent Moisture Sensor	73
7.2	Future Work	73
A	Correlation heatmaps within participants	75
B	Statistical analysis by the skin moisture group	81
	Symbols	85
	Abbreviations	87
	Bibliography	99

Chapter 1

Introduction

Humans perceive a variety of tactile signals as a result of physical contacts between the fingerpad and the surface of objects. To determine the subsequent actions, the peripheral and central nervous systems process the measured signals efficiently and rapidly. For instance, a person continuously controls the grip force used to grasp an object based on tactile signals obtained from mechanoreceptors (Westling and Johansson, 1984; Edin, 2004). The controlled force is sufficient to prevent the object from falling or slipping. When an object begins to slip from the engaged fingerpad, individuals actively respond and attempt to adjust their interaction strategies, such as increasing grip force or shifting finger position. I believe that detecting physical phenomena, such as friction and the direction of gripping force, during finger-surface interactions and correlating the measured data with these strategies would be helpful in engineering robots to be able to perform similar interactions with objects.

Unfortunately, the analysis of these prevalent finger-surface physical interactions is difficult due to the softness of the materials that constitute human fingers and the varying presence of moisture on the skin. First, eccrine sweat excreted from sweat pores located along the ridges of fingerprints modifies the interaction conditions. Depending on the amount of moisture, its presence in the microscopic gap between the fingerprint ridge and the contact surface will either increase or decrease friction (Pasumarty *et al.*, 2011). Second, the fluid within the skin also influences the change in interaction. For instance, fingers become stiffer during the winter season and then soften when the surrounding environment becomes humid. In determining the contact condition, the change in the finger's material properties is an unavoidable issue. In addition, there is no commercially available device capable of capturing the rapid excretion of sweat over time. Lastly, finger interactions are influenced by the physical conditions of the contact surface (Choi *et al.*, 2022).

This dissertation discusses extensive analyses of physical measurements taken between the human index finger and a flat glass surface in order to analyze the effect of moisture on physical contact interactions in both the normal and tangential directions. This dissertation also describes the development of a transparent moisture sensor that allows for continuous measurements.

1.1 Outline

This dissertation contains four research topics. First, we related moisture with the perception of stickiness. Second, we investigated the effect of hydration on the material properties of the finger. Third, we measured the friction created when the finger presses on a glass plate under various contact conditions. Fourth, we developed a transparent sensor that continuously measures the moisture of a fingerpad.

The first two chapters of this dissertation are the introduction and background, and the final chapter is the conclusion. The detailed outline of the intervening chapters is as follows:

- **Chapter 3: Influence of Moisture on Stickiness Perception.** This chapter examines the physical factors that influence the sensation of stickiness in a specific touch interaction. It begins by describing the apparatus we built and the procedure of the human-subject study. Next, we explain methods for processing the study's data. In the Results section, we present the measured physical data as well as the stickiness ratings based on perception. The Discussion section concludes with an explanation of the primary perception mechanism based on physical interpretations.
- **Chapter 4: Influence of Hydration on the Material Properties of the Finger.** This chapter studies how the material properties of a finger vary under different moisture conditions by identifying the lumped parameters that best simulate the pressing behavior of the finger. The Methods section explains how to obtain human finger contact area data, introduces our virtual finger model, and describes the optimization approach. The combined Results and Discussion section presents and interprets the optimized parameters.
- **Chapter 5: Effect of Moisture on Friction.** For the research described in this chapter, human participants pressed and laterally slid their fingers under contact conditions that varied in terms of finger moisture, contact duration, and surface temperature. The Materials and Methods section describes the experimental apparatus and study procedures. The Results section presents friction measurements followed by statistical analysis of the data set. Next, we interpret the observed variations in friction based on physical principles.
- **Chapter 6: Development of a Transparent Moisture Sensor.** This chapter describes methods for creating and evaluating a novel moisture sensor. The Methods section explains the design of the sensor, the fabrication steps, and a method for determining and optimizing its equivalent circuit. In the Results section, we show impedance measurements taken under various contact conditions. The interpretation of the measurements and the sensor's issues and potential solutions appear in the Discussion section.

1.2 Relevant Publications and Honors

This dissertation contains research based on the following publications:

1. Saekwang Nam and Katherine J. Kuchenbecker. Understanding the pull-off force of the human fingerpad. Work-in-progress paper (2 pages) presented at the *IEEE World Haptics Conference*, July 2019.
2. Saekwang Nam, Yasemin Vardar, David Gueorguiev, and Katherine J. Kuchenbecker. Physical variables underlying tactile stickiness during fingerpad detachment. *Frontiers in Neuroscience*, 14:235, 2020.
3. Saekwang Nam and Katherine J. Kuchenbecker. Sweat softens the outermost layer of the human finger pad: evidence from simulations and experiments. Work-in-progress poster presented at *EuroHaptics*, Leiden, the Netherlands, September 2020.
4. Saekwang Nam and Katherine J. Kuchenbecker. Optimizing a viscoelastic finite element model to represent the dry, natural, and moist human finger pressing on glass. *IEEE Transactions on Haptics*, 14(2):303–309, 2021. This journal article was also presented at the *IEEE World Haptics Conference*, July 2021.
5. Saekwang Nam, David Gueorguiev, Katherine J. Kuchenbecker. Finger Contact during Pressing and Sliding on a Glass Plate. Poster presented at the workshop on “Skin mechanics and its role in manipulation and perception” held at *EuroHaptics*, Hamburg, Germany, May 2022.

Some of these publications are associated with the following honors:

1. Best Work-in-progress Poster Award (with co-authors), *EuroHaptics*, 2020.
2. Finalist for the Best Video Presentation Award (with co-authors), *IEEE World Haptics Conference*, 2021.
3. Honorable Mention for the Best ToH Short Paper Award (with co-authors), *IEEE World Haptics Conference*, 2021.

Chapter 2

Background

2.1 Influence of Moisture on Stickiness Perception

Tactile interactions occur so often that humans rarely recognize their importance. Our daily tactile interactions start in the morning when we reach to turn off our alarm clock and continue during the day with physical contacts mediating our every action in the real world. They also give us a window into the digital: on average, a person touches his or her mobile phone 2657 times per day (Winnick, 2016), though the frequency of these actions often remains unnoticed. However, when one pays close attention, one may notice a relatively wide range of tactile sensations even when the finger is touching the same object in similar ways. For example, the surface of a screen or a cup can sometimes feel sticky and sometimes not. During dynamic touch, the stickiness of a surface is commonly related to the finger-surface friction and can depend on the touched material (Bensmaïa and Hollins, 2005), the characteristics of the fingerpad (Dinç *et al.*, 1991; Cornuault *et al.*, 2015), and exploratory parameters such as the sliding velocity and the contact force (Tang *et al.*, 2015a; Ben Messaoud *et al.*, 2016). However, the stickiness of a material can also be felt during static touch, probably through adhesion and micro-stretching of the skin (Bergmann Tiest, 2010). Variations in the mechanical properties of the finger are also known to significantly impact stickiness perception (Demartine and Cussler, 1975). Therefore, we believe the perceptual intensity of stickiness can be understood by investigating the physical interaction between the fingerpad and the surface.

The adhesion and detachment dynamics of a finger on a surface are mediated by the physiology of the finger and the physical bonds that are created. Therefore, research in physics and materials science can give us hints about the physical variables that affect the perception of stickiness. The American Society for Testing and Materials defined sticky or tacky materials as those that need additional force to separate from another item immediately after the creation of contact (Gay and Leibler, 1999). Many adhesion-based interpretations have also been proposed to explain stickiness (Gay, 2002; Pastewka and Robbins, 2014). Some adhesion theories, such as Derjaguin-Muller-Toporov (DMT) and Johnson-Kendall-Roberts (JKR), use fundamental principles to derive the force required to separate an elastic body from a hard body. These theories provide ways to calcu-

late the pull-off force based on the contact area, pressing force, and material properties of both objects (Barthel, 2008); their predictions were later supported by experimental measurements (Dorogin *et al.*, 2017, 2018). Johnson also extended these theories to the case of viscoelastic materials (Johnson, 1999). However, these approaches are not perfectly applicable to fingertip interactions because the finger's physical contact conditions change over time. For example, researchers recently found that moisture secretion from sweat glands softens the stratum corneum, the outermost layer of the fingerpad (Dzidek *et al.*, 2017a).

When it comes to the perception of stickiness, little is known about its perceptual dimensions, which makes it difficult to understand the underlying mechanisms. Zigler was one of the first to study stickiness perception using psychophysical experiments, where participants pressed their fingertips on sticky materials, such as liquid glue, prunes, molasses, and jelly (Zigler, 1923), and described their experiences. This experiment revealed that participants distinguished stickiness by expressing 'pull' in the case of strong stickiness and 'breakaway' for light, superficial stickiness. In later psychophysical experiments, Bensmaïa and Hollins suggested that the human perception of stickiness/slipperiness is mediated by intensive representations of the tactile signals, which are possibly encoded by the Pacinian tactile afferents (Bensmaïa and Hollins, 2005). More recently, Mith *et al.* (2008) conducted experiments where participants rated the tackiness intensity of a set of silicone elastomer sheets. They then measured the indentation force and depth when a probe pressed into the same samples, and they correlated the perceptual intensity judgments with the adhesion parameters, finding that human tackiness intensity is highly correlated with the full distance over which the probe separates from the elastomer. Even more recent studies have focused on the neural correlates of stickiness by observing neural activity in the human brain using functional magnetic resonance imaging (fMRI) (Yeon *et al.*, 2017). They discovered that the activated brain areas differ depending on the intensity of stickiness. In particular, two psychophysical experiments (method of constant stimuli, magnitude estimation) led them to divide sticky stimuli into three groups. These groups were used to conduct a contrast fMRI analysis that found that there are comparably more active brain areas during interactions with stickier surfaces. Kim *et al.* (2017) conducted multivoxel pattern analysis on the contrast analysis data and showed distinct neural activity patterns depending on the stickiness intensity.

In general, previous experiments on stickiness perception used highly sticky materials so that human subjects could perceive vivid signals. However, as far as we are aware, earlier studies did not explore the more subtle effect of how the perceived stickiness of a lightly sticky surface changes due to physical interaction conditions. To remove this discrepancy, Chapter 3 studies the physical variables that influence the perception of stickiness in a particular touch interaction wherein the finger detaches from smooth glass.



Figure 2.1: A soft finger's contact area develops in various ways depending on its material properties and how it is pressed into the surface (Photo by Nam and Kuchenbecker / CC BY).

2.2 Influence of Hydration on the Material Properties of the Finger

Roboticians can gain intuition about secure grasping mechanisms by understanding human fingers. One of the crucial factors to ensuring fingerpad friction seems to be increasing the contact area at initial contact; unlike many other types of non-lubricated contact, skin friction does not obey Amontons's empirical rules, which claim that the maximum static friction force is directly proportional to normal force and independent of the apparent contact area (Derler and Gerhardt, 2012). Such an argument has led researchers to have more interest in finger contact area (Fig. 2.1). For instance, Dzidek *et al.* (2017a) observed finger-contact evolution to explain how soft surfaces create the feeling of a secure grip. Additionally, Wiertelowski *et al.* (2016) experimentally confirmed that higher real contact area between a finger and a surface contributes to increasing frictional force.

The finger's contact area is highly dependent on its material characteristics. Viscoelasticity enables the finger skin to conform to the surface during contact and prevents a rapid return to its initial shape after detachment. Viscosity specifically causes the reaction force of the skin to depend on the indenter's pressing speed (Cârlescu *et al.*, 2019), and it increases the finger's mechanical impedance at higher tapping frequencies (Serina *et al.*, 1997). Traditionally, a lumped-parameter model has been used to characterize mechanical behavior like this. A four-parameter model adeptly represents the mechanical response of skin and muscle in mammals (Dinnar, 1970; Shimoga and Goldenberg, 1996). The simpler standard linear solid model with Kelvin presentation (SLS-Kelvin) can capture the initial dynamic response against an external force with only three parameters (two springs and one damper) (Dey and Basudhar, 2010).

The finger consists of living tissues whose material properties vary depending on internal states. Interestingly, the material characteristics obtained from finger experiments

with distinct conditions show a significant variation in values: Derler and Gerhardt reported that the elastic moduli of human skin in vivo vary over four to five orders of magnitude (4.4 kPa – 57 MPa) (Derler and Gerhardt, 2012). Sweat is thought to be a critical factor in altering these properties. When a finger is hydrated, the Young's modulus of its stratum corneum rises from that of glassy rubber to that of soft rubber (Adams *et al.*, 2007; Persson *et al.*, 2013). Therefore, the finger's material properties may depend significantly on hydration. Chapter 4 explores how the material properties of a finger vary under different amounts of moisture by identifying the lumped parameters that best represent the pressing behavior of the finger under each condition.

2.3 Effect of Moisture on Friction

Humans can reach out and grasp an object with minimal effort. This quick and precise ability comes from extensive reinforcement learning that occurs at a specific area of cerebral cortex in charge of the motor system (Rizzolatti and Luppino, 2001). However, this ability could not occur without friction information measured through finger-object interactions (Cadoret and Smith, 1996). A mismatch between the intrinsic properties of the object and the initially applied grip force to hold it will result in a slip. Once the slip starts, it is usually difficult to prevent the slip even though one applies higher grip force in a short time. Humans experience such cases many times in their daily life. For example, people may fail to hold a glass cup with the usual gripping force if there is an additional water layer on the surface of the cup because the water layer is the main factor for the mismatch. Similarly, someone who misjudges the fullness of an opaque container will be surprised when the desired motion does not occur as expected. Therefore, conditions at the initial interaction are crucial in determining the finger's friction.

However, finger friction has not been totally understood yet due to its major complexities. Most of all, fingers have fingerprints, each of which retains a unique pattern. Moreover, the nature of the living materials that make up the finger leads to a high level of difficulty in understanding the human finger's friction. One representative example is sweat; numerous factors, such as mental, emotional, and sensory stimuli, are entangled in the sweat secretion system and are difficult to quantify independently (Chalmers and Keele, 1952). Furthermore, sweat alters the material properties of the finger (Nam and Kuchenbecker, 2021). This complexity allows researchers to understand the characteristics of the friction only within a limited scope. Thus, most research results about the friction of human fingers have been extracted from human subject studies designed for their own purpose.

The major curiosity that fingertip tribologists have had is the role of sweat in creating friction. In general, when starting from a dry condition, friction increases until the finger becomes damp with moisture, but it drops if an excessive amount of moisture is present on the interacting surface (André *et al.*, 2009, 2010). Pasumarty *et al.* (2011) presented a similar trend of the friction shift as a function of moisture, and they additionally re-

ported the notion of contact occlusion (Adams *et al.*, 2013). Specifically, the ridges of the fingerprints press against the contact surface so that sweat excreted from these occluded ridges can accumulate quickly with minimal evaporation, resulting in a friction increase. For example, Pasumarty *et al.* (2011) presented that moisture and friction increase together over time when a participant keeps sliding an initially dry finger without detaching it. Taking the occlusion effect for granted, researchers additionally found that the furrows between the fingerprints help evaporate excessive non-occluded moisture, which regulates friction (Yum *et al.*, 2020).

The temperature of the interacting surface is another influential factor for friction. According to Choi *et al.* (2022), a surface with a higher temperature (23 – 42°C) brings about an increase in friction up to 50%. They reported that the friction increase became remarkable as the duration of the finger’s strokes increased, mainly because a long time stroking at a high temperature reduces the finger’s stiffness and expands the contact area. A similar temperature dependency in elastic modulus has separately been proven by experiments with rubber (Persson, 2001; Ludema and Tabor, 1966; Tiwari *et al.*, 2018).

Ever since Comaish and Bottoms revealed the importance of contact area in skin-surface friction (Comaish and Bottoms, 1971), researchers have suggested different optical instruments for capturing contact area based on light reflection. One approach attaches force sensors to record the direction and magnitude of the forces applied during the finger’s interaction (Bochereau *et al.*, 2017; Nam *et al.*, 2020), and another includes a vibrating plate to evaluate the change of contact area and friction across types of vibrations (Huloux *et al.*, 2021). Finally, a setup with a high-speed camera and vibrating plate demonstrated that the high amplitude of vibration reduces the finger’s contact area, and so does friction (Wiertlewski *et al.*, 2016). Moreover, this camera-based methodology has deepened scientific understanding of tactile perception (Willemet *et al.*, 2021) as well as fingerpad deformations for object manipulation (Delhayé *et al.*, 2016, 2021b).

Despite tremendous results regarding finger friction, conditions causing/preventing a slip on a fingerpad at its initial light contact have not been deeply studied and are even difficult to study. Due to the partial slip occurring at the fingerpad before the full slip (André *et al.*, 2011; Delhayé *et al.*, 2014), both static and dynamic contact contribute to friction, and their contributing ratio changes over time. Furthermore, as described above, factors determining friction (e.g., moisture, temperature, applied force magnitude, applied force direction, and sliding speed) are challenging to control. Several researchers have achieved beautiful insights about finger friction by overcoming these difficulties (André *et al.*, 2009, 2010; Pasumarty *et al.*, 2011; Choi *et al.*, 2022), but most results have been made under dynamic sliding tests, which are not highly relevant for understanding finger-surface slip at initial light touch after grasping an object.

In Chapter 5, we investigate friction at the finger’s initial slip on a glass surface. Based on previously reported research results, we defined three binary contact conditions (the finger’s moisture, the pressing time, and the temperature of the contact surface), and we tested all eight possible combinations. We asked participants to laterally slide their index finger under each combination, and we analyzed how the contact conditions affect

friction.

2.4 Development of a Transparent Moisture Sensor

People have paid more attention to the role of moisture on fingers after it was discovered that the volar region of the finger (and the toe) contains a greater concentration of sweat glands than other body locations (Taylor and Machado-Moreira, 2013). According to biotribologists, a damp finger generates greater friction than a dry or wet finger (André *et al.*, 2009, 2010; Pasumarty *et al.*, 2011; Adams *et al.*, 2013). In addition, the shape of the fingerprints permits accurate moisture regulation. In particular, eccrine sweat concentrates at the ridges of the contact fingerprint but dissipates over time through the furrows (Yum *et al.*, 2020). A change in emotion may also trigger perspiration. The finger is one of the body regions that is most sensitive to emotional stimulation (van Dooren *et al.*, 2012). Furthermore, in most natural situations, sweating is a continual process.

The continuous nature of eccrine sweat necessitates a sensor that continually monitors moisture-related signals. Unfortunately, no products offer continual measurements over time, which are necessary for understanding the time-varying response of sweat excretion to a stimulus. There are presently two representative moisture sensors on the market. One is the Corneometer (e.g., CM 825 w), which measures the capacitance of the skin in contact with its sensing area (Khazaka, 2005). It uses a pair of interdigital electrodes that produce fringing electric fields; the capacitance value between these two electrodes varies with the amount of moisture in the skin touching the sensor. The second product is Skicon-200EX, which is based on the conductance measurement (O’goshi and Serup, 2007). Conductance demonstrates a stronger link with the outer layer moisture of the skin than capacitance (Fluhr *et al.*, 1999). Both sensors require time to collect multiple measurements and provide a representative value, which limits their utility for measuring dynamic signals over time. Researchers have also created numerous sweat-monitoring sensors that provide continual readings, but the majority of them focused on detecting changes in the concentration of ions in the sweat rather than measuring the amount of sweat (Yeung *et al.*, 2021; He *et al.*, 2019; Xiao *et al.*, 2019; Gao *et al.*, 2016).

Recent advances in camera technology enable continual capture of a finger’s contact area. Using a force sensor, researchers have investigated the relationship between finger moisture and the perception of stickiness (Nam *et al.*, 2020), the significance of sweat in increasing the real contact area of a pressed finger (Dzidek *et al.*, 2017a), and the evaluation of the finger’s contact area or friction under dynamic loading (Bochereau *et al.*, 2017; Wiertelwski *et al.*, 2016; Huloux *et al.*, 2021). Transparency of the interacting surface is thus of great importance in identifying the role of moisture in determining contact area and friction. Chapter 6 describes the sensor we invented, prototyped, and evaluated for this purpose.

Chapter 3

Influence of Moisture on Stickiness Perception

Note: This chapter is based on Nam, Vardar, Gueorguiev, and Kuchenbecker’s article “Physical Variables Underlying Tactile Stickiness During Fingerpad Detachment” published in *Frontiers in Neuroscience* (Nam *et al.*, 2020) (licensed under CC BY 4.0). Some paragraphs in this dissertation’s Abstract, Acknowledgments, Introduction, Background, and Conclusion are also adapted from this publication.

We investigate the physical variables that affect the perception of stickiness in a particular touch interaction in which the finger detaches from a flat, hard glass surface. To understand the connection between perception and mechanics, we conduct a psychophysical experiment in tandem with physical measurements using a custom apparatus designed for active touch. Based on past research showing the factors that mainly affect adhesion between rigid and viscoelastic materials (Johnson, 1999), we define sixteen physical variables and explore correlations between these variables and the stickiness judgments of the participants.

This chapter is organized as follows: in Section 3.1, we describe our experimental apparatus, define sixteen physical variables of interest, and outline the methods for our human participant experiment. Section 3.2 presents the physical variables, the perceptual stickiness ratings, and how they both vary across trials and participants. Section 3.3 discusses the results, particularly which physical variables the participants considered when rating stickiness in this experiment.

3.1 Materials and Methods

In this section, we first introduce a custom-made apparatus for the measurement of three-degree-of-freedom (3-DoF) force and contact fingerprint images. Then, the statistics of the participants and the experimental procedures are described. Lastly, we explain how we process the raw data measured during each trial to derive the sixteen physical variables that we expect may relate to the perception of stickiness.

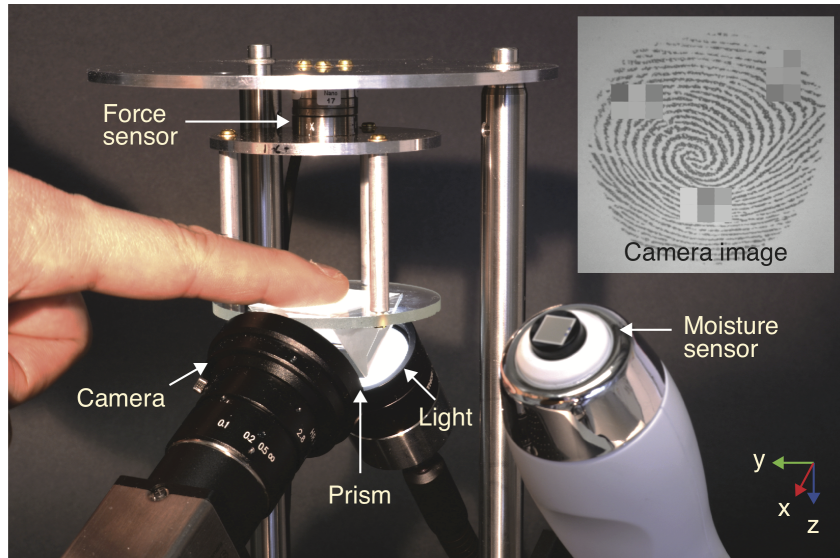


Figure 3.1: Apparatus for measuring the moisture content, contact force vector, and real contact area of a finger actively pressing on a glass plate. Note that three small rectangular regions were pixelated in the fingerprint image before publication to conceal the identity of this participant (Illustration by Nam, Vardar, Gueorguiev, and Kuchenbecker / CC BY).

3.1.1 Apparatus

We designed an experimental apparatus that can measure contact forces and finger contact area over time to test how these quantities are related to human stickiness perception (see Fig. 3.1). We also measured the moisture of the participant’s fingerpad, as moisture tends to change physical interactions between the skin and a surface (Gueorguiev *et al.*, 2017; Dzidek *et al.*, 2017a; Derler *et al.*, 2015; Tomlinson *et al.*, 2011). Moreover, we took the comfort of the participants into account by not attaching any fixtures to the finger and by making the finger-glass interaction direction downward.

A strain-based force sensor (Nano17 Titanium SI-32-0.2, ATI Inc.) was mounted above a glass surface to measure the contact force vector with a resolution of 1/171 N in all directions. The force data were collected by a data acquisition board (PCIe 6323, NI Inc.) with a sampling rate of 500 Hz. The non-coated soda lime silicate glass plate (Optifloat™ Clear, Pilkington Deutschland AG) had a thickness of 3 mm and a roughness less than 10 nm (Gläser, 1999). An optical monochrome image sensor (DCC2340M, Thorlabs Inc.) with a lens (MVL5M23, Thorlabs Inc.) was installed below the glass plate to measure the contact area of the fingerpad. The recording frame rate of the camera was set to 10 frames per second. The aperture size of the lens was minimized ($f/16$) to maximize the depth of field, providing a larger focused area.

The light intensity contrast between the contact and non-contact fingerprint areas was

emphasized by applying prism-based frustrated total internal reflection (FTIR) (Levesque and Hayward, 2003; Bochereau *et al.*, 2017). In this configuration, most of the light propagating through the prism is reflected at the top surface of the glass plate, but the light is scattered where contact occurs between the fingerprint and the glass surface, resulting in low light intensity (dark) at the contacted points in each image (see the inset image in Fig. 3.1) (Bochereau *et al.*, 2017).

The prism was glued beneath the glass substrate with cured polydimethylsiloxane (PDMS). For that, a mixture of a prepolymer and a cross-linker of Dow Corning[®] Sylgard 184 with a ratio of 10:1 was degassed and cured in an oven for one hour at 90°C. The contact surface was illuminated from below by a light source (KL 2500 LED, SCHOTT AG) shining through a light diffuser attached to the prism surface, yielding an evenly bright background. The fingerpad moisture was separately measured with a capacitive-type moisture sensor (Corneometer[®] CM 825 w, Courage + Khazaka electronic GmbH) installed next to the contact glass; this sensor measures the moisture value of the outermost layer of the fingerpad in arbitrary units (a.u.) between 0 and 130 (Constantin *et al.*, 2014).

Two custom-made LabVIEW programs (Version 2018 18.0f1) simultaneously collected the real-time data measured by the force sensor and the camera. The software was operated on 64-bit Windows 10 Enterprise 2016 LTSB installed on a computer with an Intel[®] Core[™] i7-7700 CPU and 32 GB RAM.

3.1.2 Participants

Ten people (three women, seven men) with a mean age of 29 years (standard deviation, SD: 6.4 years) participated in the experiments. None of them had current or past sensory or sensory-motor disabilities. All participants were right handed. The participants provided informed consent and received no compensation.

3.1.3 Ethics Statement

The Ethics Council of the Max Planck Society approved this research study under HI protocol 18-05B. Written informed consent was obtained from all participants. All research data were collected and analyzed according to the approved experimental protocol.

3.1.4 Experimental Procedure

Each participant took a seat after washing and drying their hands. First, participants familiarized themselves with the target interaction using the index finger of their dominant hand to touch a glass plate taped to the table. These interactions provided an opportunity to investigate the stickiness of the glass using their choice of exploratory procedures. It was the same material as the glass plate in the apparatus so that the participant could experience levels of stickiness similar to those of the experiment.

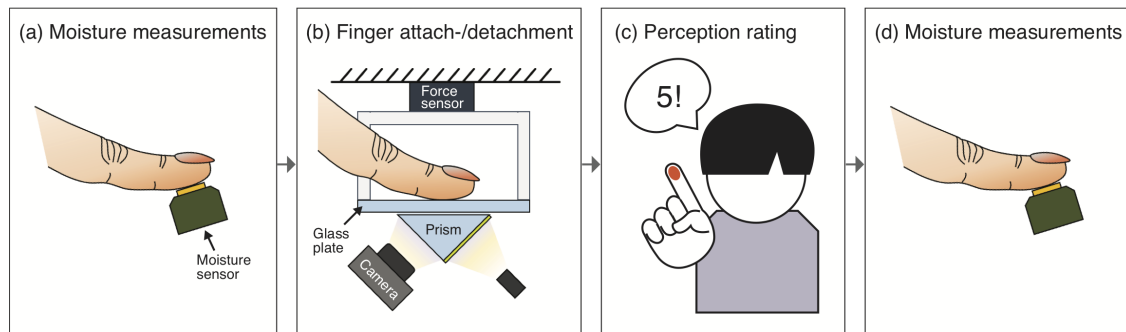


Figure 3.2: The chronological procedure of one trial of the experiment. After (a) three measurements of the fingerpad’s moisture, (b) the participant places his or her finger on a clean glass plate and reaches a normal force of 1.5 N. After a preprogrammed pressing duration (0, 1.5, or 3 s), a visual cue appears on the screen prompting the participant to detach the finger. (c) The participant detaches his or her finger and judges the stickiness of the glass using a nine-point scale. (d) The participant’s fingerpad moisture level is measured three more times (Illustration by Nam, Vardar, Gueorguiev, and Kuchenbecker / CC BY).

Once the participant was familiar with the stickiness of the glass plate, he or she started the experimental procedure. The participant’s dominant index fingerpad was wiped with isopropyl alcohol once at the start of the experiment to clean it, and the glass plate of the apparatus was cleaned before every trial. Then, the moisture level of the fingerpad was measured three times in quick succession (Fig. 3.2(a)). After that, the participant placed his or her finger at the center of the glass plate of the apparatus while watching a visual indicator of normal force (Fig. 3.2(b)). When they reached 1.5 N, which is considered a light pressing force in active touch (Papetti *et al.*, 2017), the computer pseudo-randomly selected an additional pressing time of 0.0, 1.5, or 3.0 seconds. These three pressing times were chosen because physical contact on the fingerpad is strongly affected by sweat secreted in the first 10 seconds after initial contact (Pasumarty *et al.*, 2011). After the additional pressing time, a visible cue appeared on the computer screen prompting the participant to detach his or her finger. After detaching, the participant verbally gave a stickiness rating ranging from 1 (not at all sticky) to 9 (highly sticky) (Fig. 3.2(c)). Lastly, the participant’s finger moisture level was again measured three times (Fig. 3.2(d)). Each participant repeated this same procedure for 42 trials (14 trials \times 3 different pressing durations). The average temperature in the laboratory was 21.7°C (SD: 1.1°C), and the average humidity was 50.3% (SD: 3.4%). The total duration of the experiment was about one hour per participant.

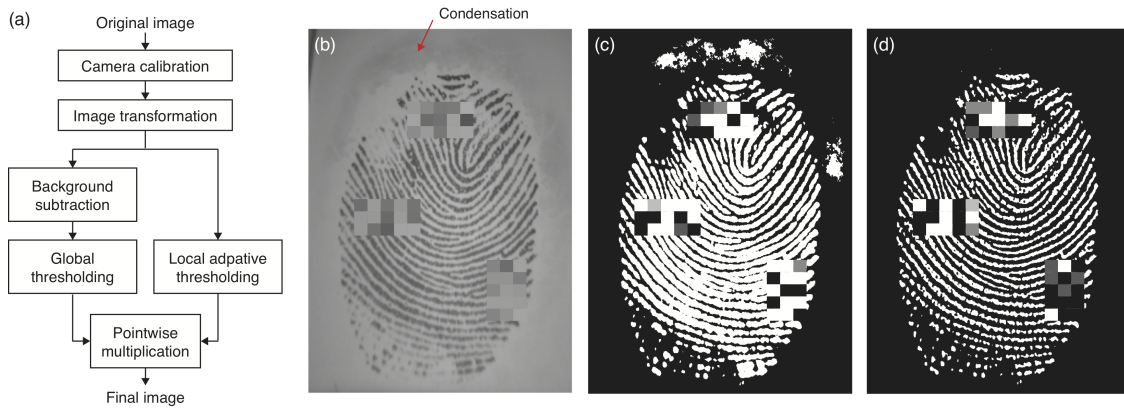


Figure 3.3: (a) Procedure for calculating the real finger contact area from a raw image. The camera calibration step corrects the lens distortion. Next, image transformation rectifies the slanted finger image. Two different threshold methods applied in parallel appropriately distinguish the finger contact area from the non-contact area without being confused by (b) condensed moisture around the finger. In such cases, taking (c) the global threshold identifies condensation as part of the contact finger area, but applying a local adaptive threshold removes the condensation area to produce (d) the final image. Note that three small rectangular regions were pixelated in each fingerprint image before publication to conceal the identity of this participant (Illustration by Nam, Vardar, Gueorguiev, and Kuchenbecker / CC BY).

3.1.5 Data Processing

The raw data collected from the force and image sensors were processed to compute the physical variables that we investigate in this study. First, time-stacked fingerprint image data underwent several processing steps for contact area extraction, and the obtained contact area was then synchronized with the recording of the finger-surface contact forces.

Calculating the real contact area

Real contact area is one of the main variables that might affect stickiness perception. To compute real contact area, we applied the series of image processing steps shown in Fig. 3.3.

An image recorded by the camera cannot be directly used to calculate the contact area because it is distorted by both the round shape of the lens and the viewing angle between the camera and the glass plate. The radial image distortion due to the lens was flattened using camera calibration. This process made use of the intrinsic camera parameters computed from several images of a printed checkerboard taken from different angles (MATLAB Camera Calibration Toolbox, 2018). Next, the flattened image was transformed to estimate the image that the camera would see if it was positioned per-

pendicular to the glass plate. For that, we first captured a 15 mm \times 15 mm image of a square rubber piece placed on the glass, and we then calculated the transformation matrix that converts the viewed shape to a square using the projective transformation method (Goshtasby, 1986). We used this same image to calculate the area per pixel (0.000986 mm²/pixel) by dividing the actual area of the square by the number of pixels it occupied in the transformed image.

The real finger contact area is usually calculated using global thresholding. In this method, the contact area is found by first subtracting what is seen before finger contact and then binarizing the image with a thresholding value. However, a highly moist finger causes the condensation of tiny liquid droplets around the finger (see Fig. 3.3(b)), which look like vague clouds and were also detected as contact points by global thresholding (Fig. 3.3(c)). We solved this issue by local adaptive thresholding (Fig. 3.3(d)) (Davies, 2012), which calculates different threshold values for different regions of the image. We used the intersection of the two logical (negative/positive) images based on each thresholding method to obtain a binarized image that reflects real contact. Finally, we calculated real fingerpad contact area by multiplying the number of pixels considered as contact by the area per pixel.

Extracting parameters from the force and contact area data

We extracted key parameters from the measured force and contact area data (see red dots in Fig. 3.4) after synchronizing the image and contact force data recordings. In order to extract quantitative measurements that relate to the physical variables under scrutiny, we decomposed the dynamics of pressing and detaching the finger into several qualitatively different time intervals. t_0 is defined as the time the finger starts to contact the plate. The time the normal force reaches 1.5 N is marked as t_1 . t_2 is the time the pressing finger starts to detach by reducing its normal force. The finger pulls off the stationary glass plate and usually generates negative force values for a short duration. This detachment phase occurs between t_3 and t_4 (inset in Fig. 3.4(a)), where t_3 is the time when the force is closest to 0 N during the detachment, and t_4 is the first time when the finger is completely detached. We define the peak pull-off force as the minimum contact force in the z-direction (\hat{F}). The maximum real contact area before detachment is defined as A_{real} .

Physical variables investigated for stickiness perception

Based on the parameters extracted from the measured raw data, we defined sixteen physical variables to be investigated in correlation with stickiness perception. These variables were selected based on contact-adhesion theories and related experiments found in the literature, as noted.

1. **The finger holding duration while the pressing force is kept around 1.5 N**
($t_{\text{hold}} = t_2 - t_1$)

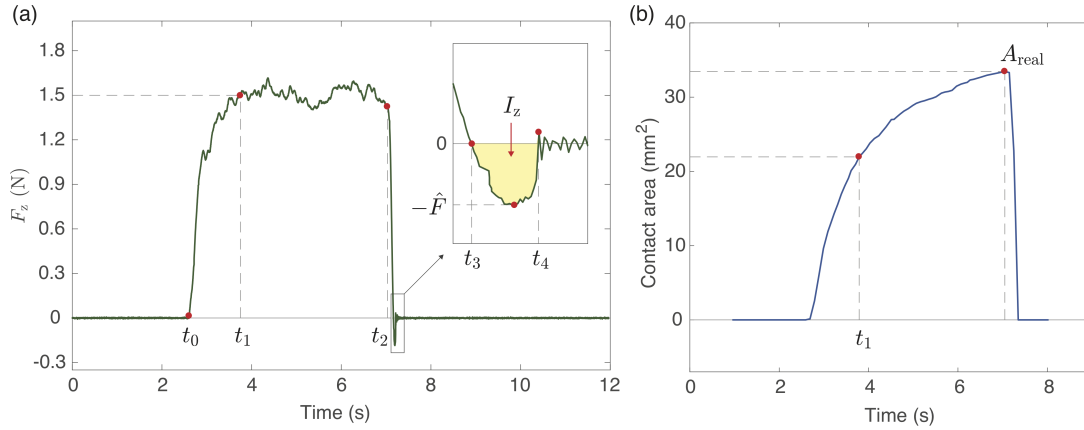


Figure 3.4: (a) The measured force in the z-direction and (b) the real contact area as a function of time from a sample trial, including parameter definitions (Illustration by Nam, Vardar, Gueorguiev, and Kuchenbecker / CC BY).

t_{hold} is the duration between the instant that the force in the z-direction reaches 1.5 N (t_1) and the time that the pressing force starts to decrease (t_2). This holding time leads to changes in physical phenomena such as sweat secretion, which is known to affect the softness of the fingerpad (Dzidek *et al.*, 2017a), and occlusion, which reduces water lost to the atmosphere (Zhai and Maibach, 2001; Pasumarty *et al.*, 2011).

2. Detaching duration of the finger after force changes sign ($t_{\text{pull}} = t_4 - t_3$)

Fast adapting (FA) mechanoreceptors are known to respond strongly when the applied mechanical stimulus changes (Vallbo and Johansson, 1984; Caldwell *et al.*, 1999). Therefore, we thought looking at the time it takes the finger to pull off the glass plate is particularly important. This value is obtained by subtracting t_3 from t_4 .

3. Detachment rate (\dot{F})

Researchers previously showed that a glass ball's peak pull-off force from a polyurethane surface depends on its detachment speed (Barquins and Maugis, 1981). Because the materials are similar, we anticipate a similar result in our study. Since our apparatus cannot measure finger motion in the normal direction, our analysis uses the detachment rate (\dot{F} (N/s)) as a similar variable. It shows how quickly the measured force decreases during finger detachment (from t_2 to t_3). To derive this value, we fit a linear function to the force data between the two time points, and we use the absolute value of the derivative of the function as the detachment rate.

4. Detachment rate at t_3 (\dot{F}_{t_3})

Although separation of a fingerpad from the glass plate happens very quickly, the instantaneous detachment rate often changes across this time span. Focused more at the moment of the separation (t_3), we define another variable regarding the detachment rate. It is calculated in the same way as \dot{F} , but we consider the force rendered in the last 0.01 seconds before t_3 .

5. Root mean square of force in the x-direction during the pull-off ($F_{x,rms}$)

As shown in Fig. 3.1, the x-axis points from the apparatus toward the participant's hand. Thus, the measured force in this direction is expected to come from friction between the finger and the glass. As this frictional force can affect stickiness perception (Yeon *et al.*, 2017), we define a representative force value by taking the root mean square (RMS) of the x-force while the finger is experiencing a negative normal force (from t_3 to t_4). Therefore, if there are n values of F_x between t_3 and t_4 , the variable is defined as $F_{x,rms} = \sqrt{\frac{1}{n}(F_{x1}^2 + F_{x2}^2 + \dots + F_{xn}^2)}$.

6. RMS of force in the y-direction during the pull-off ($F_{y,rms}$)

For the same reason mentioned above, we are also interested in the RMS of the interaction force in the y-direction. This value shows the strength of the frictional force a finger exerts to its left and right between t_3 and t_4 . Therefore, $F_{y,rms} = \sqrt{\frac{1}{n}(F_{y1}^2 + F_{y2}^2 + \dots + F_{yn}^2)}$.

7. RMS of force in the z-direction during the pull-off ($F_{z,rms}$)

The force in the z-direction shows the interaction between the finger and the plate in the normal direction. During pull-off, it highlights the additional force needed to separate the finger from the glass plate (Pastewka and Robbins, 2014). Like $F_{x,rms}$ and $F_{y,rms}$, the definition for the z-direction is $F_{z,rms} = \sqrt{\frac{1}{n}(F_{z1}^2 + F_{z2}^2 + \dots + F_{zn}^2)}$.

8. RMS of force during the pull-off (F_{rms})

People could perceive stickiness without considering the direction in which the force occurs (i.e., based on the magnitude of the force vector), particularly in the case when the interaction time is very short, such as finger detachment. Thus, comparing the RMS force in each direction ($F_{x,rms}, F_{y,rms}, F_{z,rms}$) with the RMS of the force vector's magnitude (F_{rms}) can tell us whether a particular force direction (such as frictional or normal) is crucial for people to feel stickiness. The value is calculated as $F_{rms} = \sqrt{\frac{1}{n}(F_1^2 + F_2^2 + \dots + F_n^2)}$, where each F is force vector magnitude.

9. Impulse in the x-direction during the pull-off (I_x)

The RMS force calculations average over time and therefore disregard the wide range of pull-off times (t_{pull}). We define the pull-off impulse as the integral of

force over time to reflect both the measured time and force; such a calculation is common in mechanics, but we have not found any prior use of impulse in stickiness research. Here, we consider only the x-direction, and we take the absolute value of the force because we believe forces in both directions may cause a sensation of stickiness. Therefore, I_x is calculated as $\int_{t_3}^{t_4} |F_x(t)| dt$.

10. Impulse in the y-direction during the pull-off (I_y)

Impulse in the other frictional direction is also considered as a physical variable. Therefore, I_y is $\int_{t_3}^{t_4} |F_y(t)| dt$.

11. Impulse in the z-direction during the pull-off (I_z)

The normal direction of impulse during the finger's detachment shows the total adhesive force applied to the finger. As the force in the z-direction during the pull-off is always negative, we flipped its sign so that the magnitude of the z-impulse is intuitively matched to the perception of stickiness. One example of the value is shown as the area shaded in yellow in the inset of Fig. 3.4(a). I_z is $\int_{t_3}^{t_4} -F_z(t) dt$.

12. Total impulse during the pull-off (I)

For the same reason that we set F_{rms} as one of the physical variables, we also define the impulse of the force vector magnitude to combine all three directions. Mathematically, this is $\int_{t_3}^{t_4} \sqrt{F_x(t)^2 + F_y(t)^2 + F_z(t)^2} dt$.

13. Maximum real contact area (A_{real})

Under the same conditions for the pressing force, time, and material properties of a viscoelastic finger, differences in the contact area are known to produce meaningful distinctions in contact adhesion (Barthel, 2008). The maximum value can be found from the measured contact area as a function of time (the red dot indicating A_{real} in Fig. 3.4(b)).

14. Peak pull-off force (\hat{F})

As adhesion theories have evolved based on the study of adhesive force between two contacting objects (Dorogin *et al.*, 2017; Barthel, 2008), we thought pull-off force could be highly related with stickiness. As shown in the inset of Fig. 3.4(a), F_z is negative when a finger is pulling off the glass plate. The most negative force in the inset is considered as the peak pull-off force (\hat{F}). Here, we made \hat{F} positive by flipping the sign of F_z so that larger values are intuitively connected to the magnitude of stickiness.

15. Mean moisture value (\bar{M})

Sweat secretion from the pores located along the fingerprint ridges can contribute to better grip by strengthening the coalescence process between the fingerpad and

the contact surface (Dzidek *et al.*, 2017a). Thus, moisture-related variables should be taken into consideration in our analyses. We measured the moisture value six times in each trial (three times before, three times after) using the moisture sensor. The mean moisture value comes from taking the average of the six measured values.

16. Change in moisture after finger detachment (ΔM)

The change in the amount of sweat on the skin might also influence the perception of stickiness. Here, ΔM of a given trial is the difference between the average moisture value measured after the trial and the average value before the trial, with positive variable values indicating an increase in moisture.

Stickiness ratings (Rating)

After each trial, the participant rated the stickiness they experienced using a nine-point scale (1 – 9), with larger values meaning a stickier interaction.

Data analysis

We applied Spearman's rank-order correlation to discover which of the sixteen calculated physical variables are perceptually related to stickiness and how these variables are correlated with each other. This method elucidates how closely the ranked values of one physical variable match the rank order of another variable. Given pairs of a measured value and a rating, where the measured values are sorted in ascending order, the correlation of the pairs is high ($\rho \approx 1$) if the order of the ratings is also close to ascending order. This coefficient (ρ) is 0 when there is no order similarity at all between the two lists of values, and it is -1 when they are anti-correlated. We visualize the correlations between all possible pairs of a participant's sixteen variables and ratings as a heatmap. An additional heatmap presents the correlations between the median values of the physical variables across participants.

The reliability of the correlation analysis presupposes that all physical conditions, such as the finger's temperature and material properties, do not change significantly across trials. Because the isopropyl alcohol used to clean the finger at the start of the experiment might affect the physical status of the finger, and also because fingers quickly adapt to the interaction condition by changing the speed of sweat secretion (Johansson and Cole, 1994), we discarded the data from the first 6 trials of each participant, leaving about 36 trials for the correlation calculation.

The total number of trials used for the correlation calculations is different from participant to participant. A participant sometimes touched the top plate of the apparatus after detachment, which negatively affects force data collection. In such cases, we asked the participant to conduct additional trials to make up for this error. Furthermore, we excluded all trials that had problems in data recording.

Subject removal We could not include any of the data collected from one female participant. In most of this individual's trials, the measured z-force did not smoothly converge to zero after detachment. Instead the signal persistently oscillated at a frequency that we suspect to be the resonance frequency of the force sensor and contact platform. We believe too much x-force (median $F_{x,rms} = 1.48$ N) was applied to the force sensor in an extremely short time (median $t_{pull} = 0.022$ s). These oscillations hindered the calculation of the parameters used to derive the physical variables for this subject, leaving a total of nine participants (two women, seven men).

3.2 Results

This section presents the results of our study, starting with the distributions of the measured physical variables and the reported stickiness ratings; the full data set can be viewed in Appendix A. The section then moves to correlation analyses both within and across participants, and it concludes with a detailed investigation of the effects of frictional forces in the studied interaction.

3.2.1 Physical Variables

Figure 3.5 presents the distributions of the sixteen physical variables calculated from the data of all nine participants. In the case of t_{hold} (Fig. 3.5(a)), the measured ranges are similar among participants because the signal to detach the finger appeared a random duration of either 0, 1.5, or 3 seconds after the participant reached a pressing force of 1.5 N. However, the ranges of all the other variables vary more because there were no external restrictions on these other aspects of the finger interaction.

3.2.2 Stickiness Perception Ratings

Participants also had different rating distributions. As shown in Fig. 3.6, one participant (S5) used the whole rating range, whereas another participant (S6) rated stickiness within a much more limited range (4 levels out of 9). The minimum and maximum ratings are also different between participants. For example, the rating range of S1 is from 3 to 8, but that of S3 is from 1 to 6. As we did not restrict any physical conditions except for the randomly allocated t_{hold} , it may have been difficult for participants to determine whether a given trial deserved the overall maximum (or minimum) stickiness rating.

3.2.3 Correlation to Stickiness within Participants

The correlations between the sixteen physical variable values and the stickiness ratings for each participant were calculated. 136 correlation coefficients (ρ) and corresponding probability values (p) were obtained per participant; all nine of these heatmaps can be

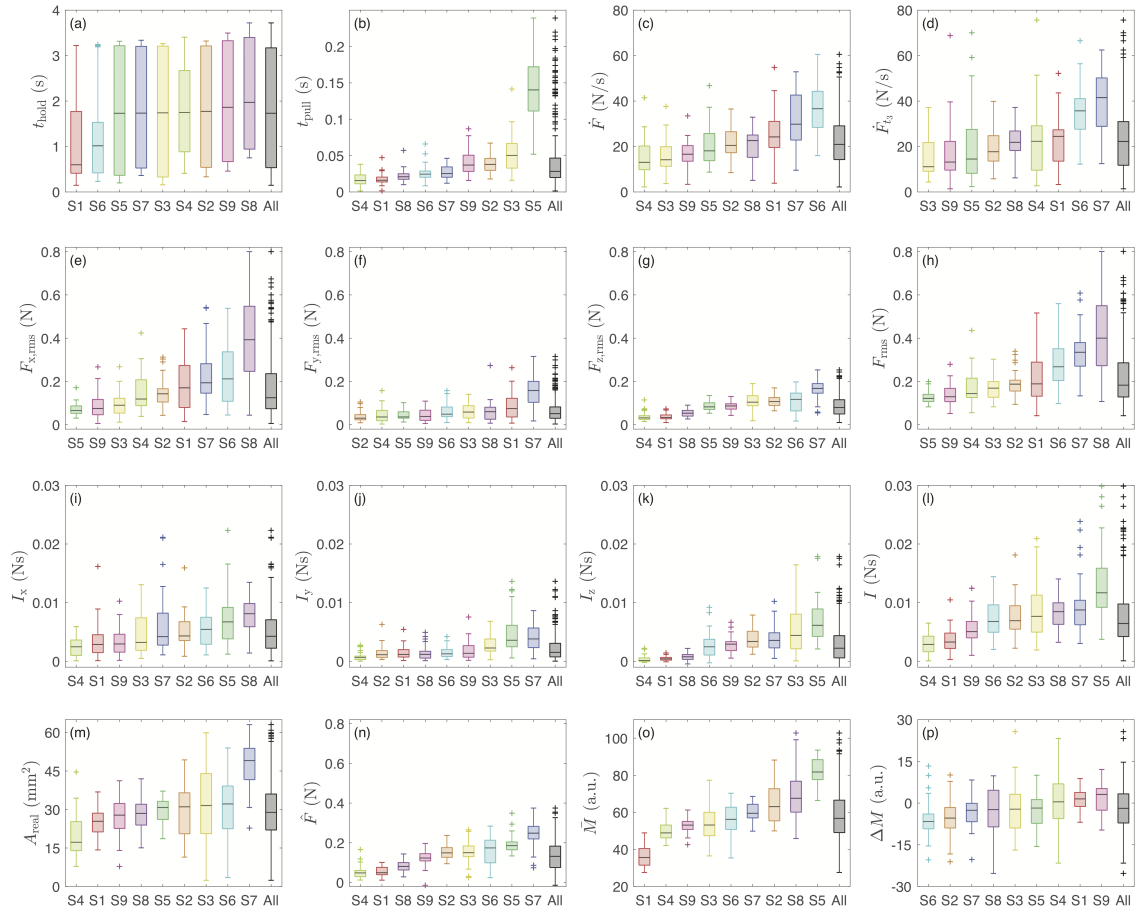


Figure 3.5: Boxplots of the sixteen physical variables calculated for each participant (S1 to S9), ordered by ascending median value with all subjects combined at the end. The data are color-coded by participant. In each distribution, the black line shows the median, the box shows the second and third quartiles, the whiskers show the range up to 1.5 times the interquartile range, and the + symbol indicates outliers. The plotted variables are (a) t_{hold} , (b) t_{pull} , (c) \dot{F} , (d) \dot{F}_3 , (e) $F_{x,\text{rms}}$, (f) $F_{y,\text{rms}}$, (g) $F_{z,\text{rms}}$, (h) F_{rms} , (i) I_x , (j) I_y , (k) I_z , (l) I , (m) A_{real} , (n) \hat{F} , (o) \bar{M} , and (p) ΔM (Illustration by Nam, Vardar, Georghiev, and Kuchenbecker / CC BY).

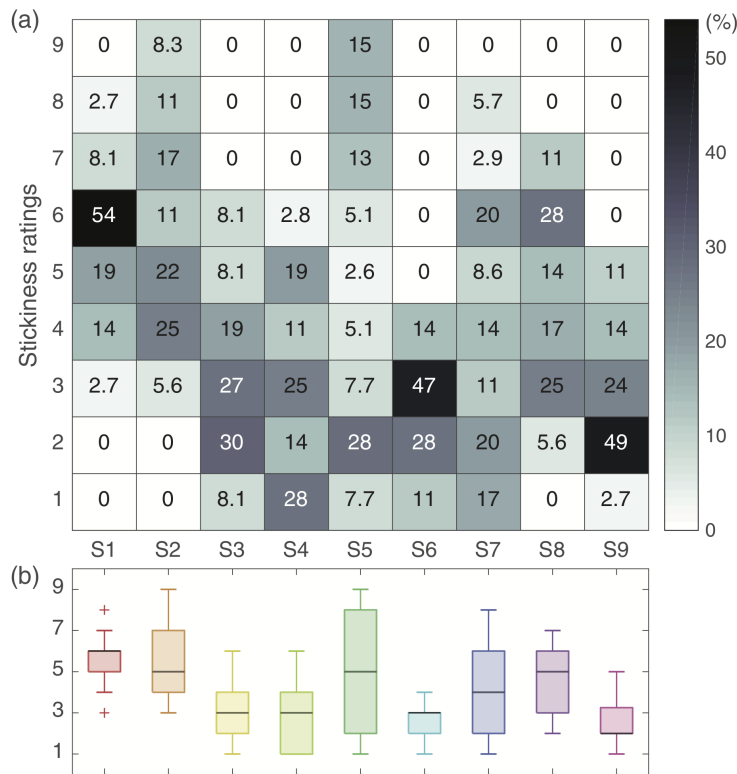


Figure 3.6: Distributions of stickiness ratings across participants. (a) The numbers in the heatmap represent the percentage of trials that received each rating. (b) The entire distribution of ratings per participant is shown as a boxplot (Illustration by Nam, Vardar, Gueorguiev, and Kuchenbecker / CC BY).

viewed in the supplementary materials. Figure 3.7 shows a heatmap representing the average of the nine participant-specific heatmaps, where the ratio shown at the bottom of each box indicates the proportion of participants for whom the given correlation was significant ($p < 0.05$).

The bottom row in the heatmap (Fig. 3.7) indicates how strongly each physical variable correlates with the stickiness rating. The means and standard deviations of the nine subject-specific correlation coefficients are plotted below the heatmap. Here, the pre-detachment pressing time (t_{hold} , $\bar{\rho} = 0.53$), the overall impulse during the normal direction during the finger detachment after normal force changes sign (I_z , $\bar{\rho} = 0.51$), the overall impulse during the same time span (I , $\bar{\rho} = 0.50$), the time taken for the finger to detach (t_{pull} , $\bar{\rho} = 0.43$), and the RMS of z-force ($F_{z,\text{rms}}$, $\bar{\rho} = 0.40$) are the main contributors to the perception of stickiness.

Considering the calculational similarity between I and I_z and the fact that I_z is more strongly correlated with stickiness than I is, we believe that the z-component of impulse may mainly influence the stickiness rating. Therefore, we seek to understand the two

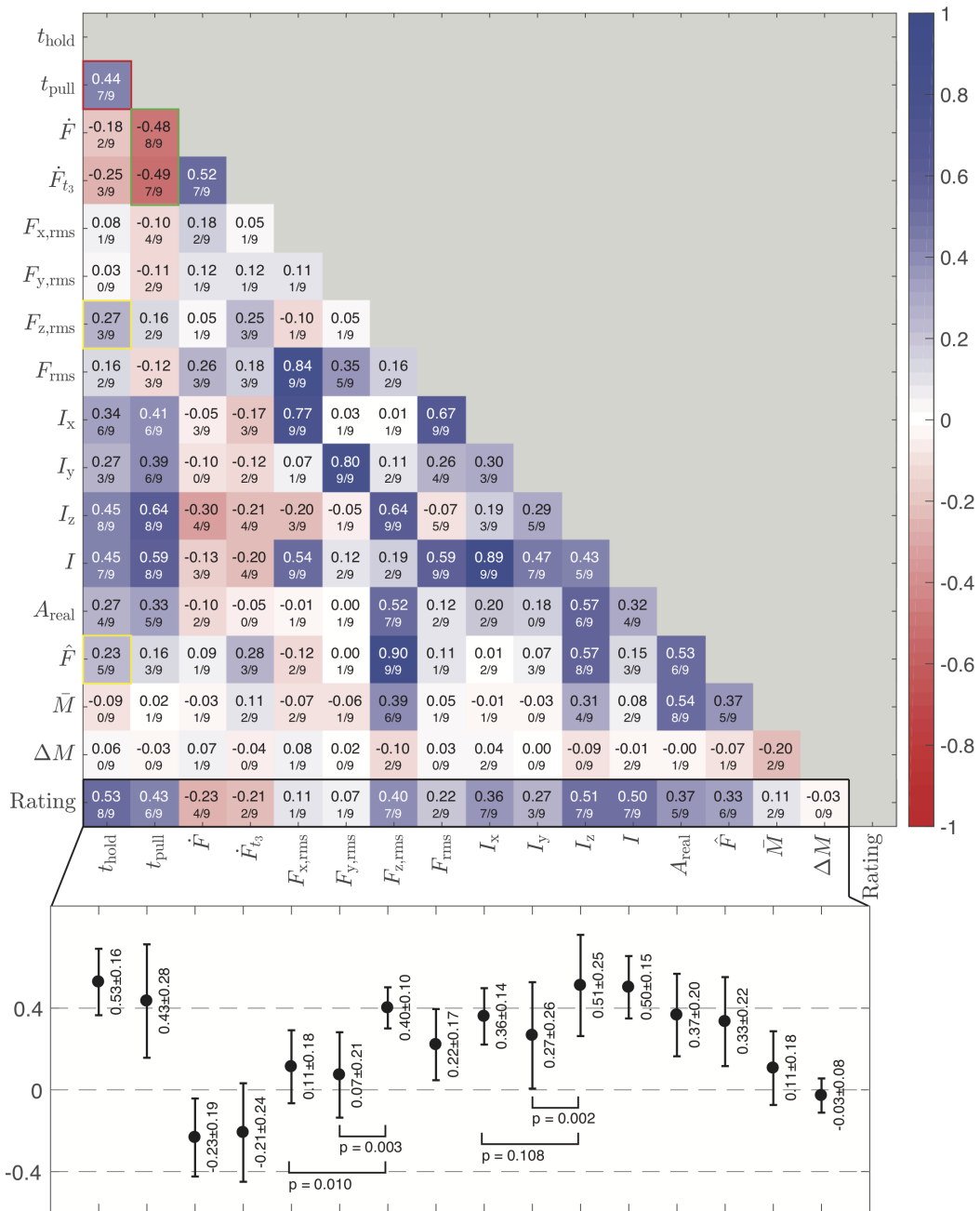


Figure 3.7: A heatmap showing the mean participant-specific correlation coefficients ($\bar{\rho}$) among the physical variables and the stickiness ratings. The second line of text in each cell lists the proportion of subjects whose correlations showed high significance ($p < 0.05$). The bar chart located below the heatmap shows the means and standard deviations of ρ across participants, plus the p-values of the four paired t-tests reported in the text (Illustration by Nam, Vardar, Gueorguiev, and Kuchenbecker / CC BY).

variables based on I_z .

The correlation of z-impulse (I_z) to the stickiness rating was higher than that of the RMS of z-force ($F_{z,rms}$) or that of the peak pull-off force (\hat{F}). This result indicates that the time taken for a finger to detach helps a person perceive stickiness; the fact that t_{pull} has a higher correlation coefficient to the stickiness rating than $F_{z,rms}$ supports the importance of time involvement to evoke the feeling of stickiness.

3.2.4 Correlation across Participants

We used the values of the sixteen physical variables to generate another heatmap that shows correlations between the median values of the variables across participants. The number in each cell of Fig. 3.8 indicates how close the participant order sorted in ascending median of one variable (visible in Fig. 3.5) is to that of another variable. These correlation coefficients are also calculated by Spearman's rank-order correlation method.

3.2.5 Effects of Frictional Forces on the Stickiness Ratings

The present study was performed in active touch conditions and did not prevent the participant from moving the finger laterally while pulling off. The lateral (frictional) components of the pull-off action therefore resulted in non-negligible forces generated in the x- and y-directions. Such forces primarily occurred in the x-direction, with larger measured forces along this axis compared to the y- and z-directions (Fig. 3.5(e), (f), (g)); the median RMS forces in the x-, y-, and z-directions were 0.1250 N, 0.0454 N, and 0.0800 N, respectively. This trend also appeared in the directional impulse values (Fig. 3.5(i), (j), (k)); the median impulse values were 0.0043 Ns, 0.0015 Ns, and 0.0022 Ns in the x-, y-, and z-directions, respectively.

However, we found that the vertical (normal) component of force and impulse evokes the feeling of stickiness more than the horizontal (frictional) component. To evaluate the perceptual value of stickiness cues generated in the vertical (z) direction, we tested how the RMS of the z-force and the z-impulse correlated with the perception of stickiness. For the RMS of the force, we found that $F_{z,rms}$ correlated significantly better with the stickiness ratings than $F_{x,rms}$ (paired t-test: $t = 3.358$, $df = 8$, $p = 0.010$) and $F_{y,rms}$ (paired t-test: $t = 4.292$, $df = 8$, $p = 0.003$; see the bottom plot in Fig. 3.7). For the impulse, I_z correlated significantly better with the stickiness perception than I_y (paired t-test: $t = 4.345$, $df = 8$, $p = 0.002$), but the difference with I_x did not reach statistical significance (paired t-test: $t = 1.805$, $df = 8$, $p = 0.108$).

We then tested which directional component provides a better correlation between stickiness ratings and the median impulse of the measurements (i.e., the median x- or z-impulse from the measurements of each participant). We found that z-impulse's correlation becomes stronger as the median z-impulse increases (Spearman's correlation: $\rho = 0.77$, $p = 0.02$; see Fig. 3.9(a)). On the contrary, the x-component did not show any sensory relevance (Spearman's correlation: $\rho = -0.23$, $p = 0.55$; Fig. 3.9(b)). The

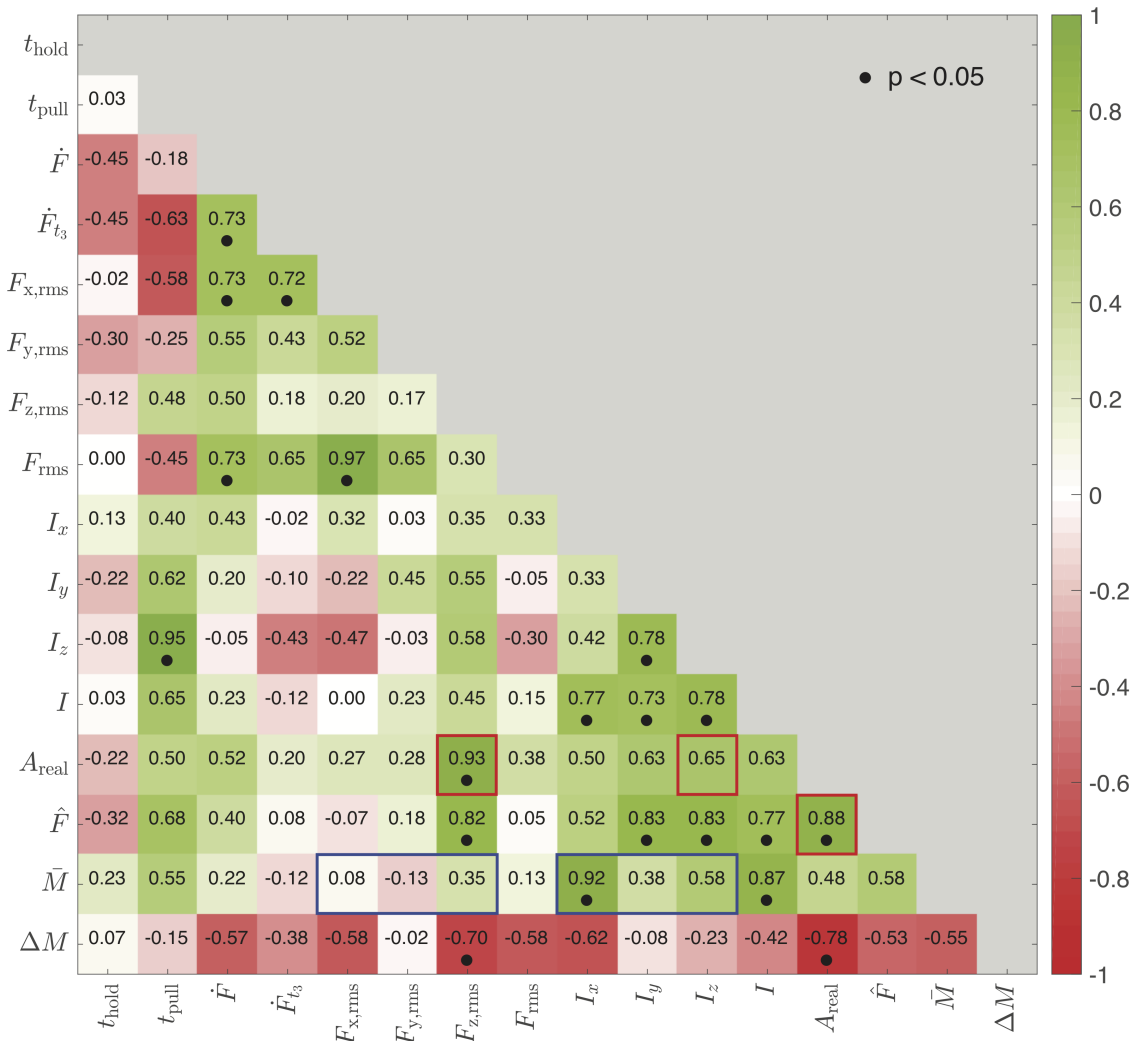


Figure 3.8: Correlations between the physical variables across participants based on the median variable value for each participant. A high value means that the nine participants are ranked in approximately the same order in the two corresponding subplots of Fig. 3.5. A dot appears under the coefficient when the correlation is significant ($p < 0.05$) (Illustration by Nam, Vardar, Gueorguiev, and Kuchenbecker / CC BY).

correlation of I_x to stickiness also did not increase in terms of the participant’s median I_z (Fig. 3.9(c)). These results suggest that the sensory cues used by participants to shape their perception were mostly related to the vertical (normal) component of detachment and not very influenced by simultaneously generated frictional cues.

3.3 Discussion

As anticipated, subjects assigned a wide range of stickiness ratings to their interactions with the glass plate. The mechanics of the interaction also varied significantly, allowing us to uncover the underlying mechanical sources of this perceptual variability.

3.3.1 Main Perception Mechanism

We found that the perceived stickiness of a glass plate is significantly affected by the values of t_{hold} , t_{pull} , and I_z . Simple logic and pieces of evidence found from the correlation heatmap (Fig. 3.7) indicate that the main flow of the variables is $t_{\text{hold}} \rightarrow I_z(t_{\text{pull}}) \rightarrow \text{Rating}$. The contact time (t_{hold}) is the variable that builds the adhesion between the fingerpad and the glass plate. This adhesion requires either a high normal force to pull off the glass or a high normal impulse; t_{pull} correlates more strongly with t_{hold} ($\bar{\rho}(t_{\text{hold}}, t_{\text{pull}}) = 0.44$, see red-bordered box in Fig. 3.7) than the z-forces do ($\bar{\rho}(t_{\text{hold}}, F_{z,\text{rms}}) = 0.27$, $\bar{\rho}(t_{\text{hold}}, \hat{F}) = 0.23$, see yellow-bordered boxes in Fig. 3.7). As t_{pull} is a component of I_z , the high correlation coefficient implies that t_{hold} contributes more to the creation of the z-impulse than the z-forces do. Therefore, we conclude that t_{hold} affects t_{pull} by establishing secure contact, which causes an increase in the z-impulse (I_z) and evokes a feeling of stickiness.

We believe that the time taken to break contact with the glass (t_{pull}) is important for participants to feel stickiness because the time-related variables (t_{pull} and I_z) are more

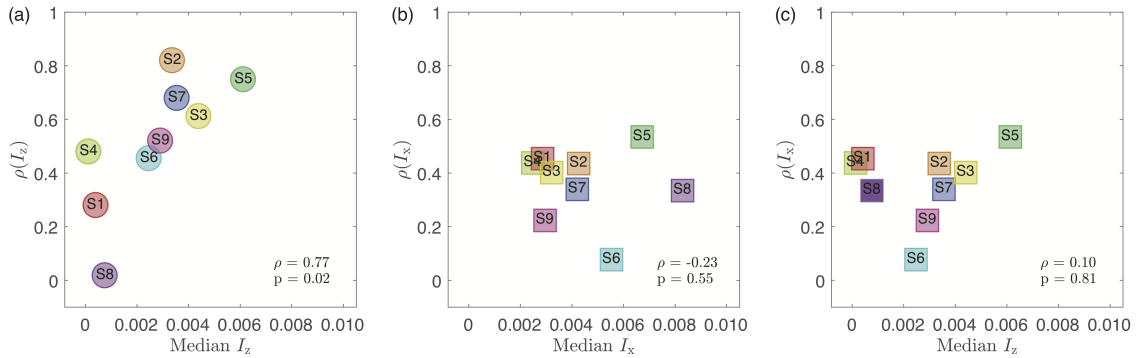


Figure 3.9: Sensory relevance between I_z and I_x by comparing correlations between stickiness and the impulse that participants felt. (a) A clear sensory relevance is shown by a high correlation between the directional correlation between stickiness and the z-impulse and the median z-impulse value experienced by participants. (b) There is no trend in the same correlation for the x-direction. (c) The correlation between stickiness and the x-impulse also does not correlate with the median x-impulse (Illustration by Nam, Vardar, Gueorguiev, and Kuchenbecker / CC BY).

strongly correlated with the stickiness ratings than the force-based variables are. According to Fig. 3.7, detachment rate anti-correlates with pull-off time t_{pull} ($\bar{\rho}(\hat{F}, t_{\text{pull}}) = -0.48$, $\bar{\rho}(\hat{F}_{t_3}, t_{\text{pull}}) = -0.49$; see the boxes with green borders in Fig. 3.7). In the case of viscoelastic material such as the fingerpad, the strategy of decreasing detachment speed contradicts the theoretical prediction for how to increase the force needed to separate two contacting objects (i.e., \hat{F}) (Barquins *et al.*, 1978). However, given that the perception of stickiness is more related to I_z than to \hat{F} , it seems people are sensitive to the finger's separation time when judging stickiness. Thus, slow detachment increases the sticky feeling as long as the contact between the finger and the glass plate has been strongly established.

3.3.2 Finger Size and Peak Pull-off Force

The difference in A_{real} across participants stems not only from contact conditions but also from the size of the participant's finger (see Fig. 3.5(m)). We note that the participant order based on the median A_{real} is highly similar to their order based on the median $F_{z,\text{rms}}$ values (see Fig. 3.5(m,g)); indeed, the order similarity between these two variables is 0.93 (see Fig. 3.8). Interestingly, the participant order by median A_{real} also has a close correlation to that by the median peak pull-off force ($\rho(\hat{F}, A_{\text{real}}) = 0.88$) but a much lower correlation to that by median z-impulse ($\rho(I_z, A_{\text{real}}) = 0.65$, highlighted with red boxes in Fig. 3.8). This close relationship between contact area (A_{real}) and pull-off force ($F_{z,\text{rms}}$, \hat{F}) across subjects provides good support for contact-adhesion theories (Gay, 2002; Barthel, 2008; Pastewka and Robbins, 2014). Since these variables were not strongly correlated with stickiness rating within subjects, it seems that perception of stickiness diverges somewhat from theory. Combined, our findings show that perceptual stickiness is distinct from mechanical stickiness; people base their ratings mainly on the impulse that they feel during detachment, not on the peak pull-off force.

3.3.3 Finger Moisture and Impulse

In the case of participant order by median impulse, another important variable is finger moisture; correlations of mean moisture to impulse are generally higher than to forces (highlighted with blue boxes in Fig. 3.8). The low correlation coefficients between moisture and forces are anticipated by Cornuault *et al.* (2015)'s previous study showing that the water descriptor index of human fingers is not significantly correlated with the coefficient of friction on sticky surfaces. The close correlation between the finger moisture and impulse seems to imply that an increase in moisture leads to longer detaching duration. However, this correlation did not appear in Fig. 3.7, which focuses on within-participant variations. In other words, the correlation to impulse is more pronounced at when considering a broad range of moisture levels across participants, rather than with the smaller variation of moisture within a participant (Fig. 3.5(o)). This comparison suggests that

substantial increases in finger moisture lead to longer detaching durations and consequently larger impulses.

3.3.4 Comparisons with Other Perceptual Studies

Other researchers have reported that rating distributions for roughness are similar to those for stickiness in experiments where the participant slides his or her finger across varied surface textures (Bensmaïa and Hollins, 2005). During such finger sliding, the perception of stickiness increases mainly due to the coefficient of friction (Bergmann Tiest, 2010), which is induced by the surface roughness (Tomlinson *et al.*, 2009) and/or by liquids on the finger (Tang *et al.*, 2015b). However, we showed that perceived stickiness can also vary in vertically active movements of a finger on a fixed surface, without any significant lateral motion.

Mith *et al.* (2008) showed that the human sensation of tackiness (stickiness) of an elastomer is similar to the full distance experienced between the fixed elastomeric sample and a pulling indenter, which is higher when the two materials stay attached for a longer duration of time. Interestingly, we found that the sensation of light stickiness made between a human finger and a hard surface also greatly depends on the time taken for the finger to detach, as well as on the impulse, which is intimately linked to detachment time. Although the surfaces being contacted in these two studies are quite different, we are encouraged by the alignment of these perceptual and mechanical results.

3.3.5 Experimental Limitations

Our conclusions are certainly limited by the population of participants in this study. We tested only a limited number of individuals in early-to-mid adulthood (29 ± 6.4), so we cannot know whether the significant mechanical and perceptual results we found would also hold for much younger or older populations, nor for a more diverse sample of individuals from the same age group. Given the design of our study, we also were not able to make conclusions about stickiness perception at normal forces that are lower or higher than 1.5 N.

Second, the test material was limited to one type of smooth glass. Because subjects knew that they were touching the same piece of glass in every trial, they might tend to report a constant value of stickiness that did not depend on trial-to-trial variations. We tried to minimize this bias by having each subject touch an identical glass plate under diverse pressing conditions before data collection began. In future research, it would be interesting to understand how important physical variables change depending on the test material. This comparison would give us a more profound understanding of the perceptual mechanism of light stickiness.

Third, research on this topic would benefit from an objective metric that can evaluate the perception strength against a stimulus. Our study could not elucidate how two independent people perceive the same interaction because the perception ratings were

different from participant to participant. One possible reason for these rating variations is that the fingerpad's physiological composition varies greatly across people (e.g., hydro lipid film composition (Cornuault *et al.*, 2015)). Another possible explanation is that individuals were free to decide how to interpret the nine-point rating scale. If the assessment of perception is based on objective indicators, such as the activation strength of a particular brain region (Kim *et al.*, 2017), physical variables measured from many people can be more efficiently used to derive an objective understanding of perception.

We were also limited by current moisture-sensing technology. There are no available transparent commercial sensors that can measure finger moisture. Thus, we placed a reliable commercial moisture sensor next to the glass plate. This configuration cannot prevent the loss of moisture on the fingerpad while the finger moves away from and to the sensor. In addition, measuring only before and after each trial did not let us study the effects of changes in the moisture over time due to sweat secretion and occlusion. To simultaneously measure the real contact area and the moisture of the finger during contact with the glass plate, we must develop a transparent moisture sensor.

Chapter 4

Influence of Hydration on the Material Properties of the Finger

Note: This chapter is based on Nam and Kuchenbecker’s article “Optimizing a Viscoelastic Finite Element Model to Represent the Dry, Natural, and Moist Human Finger Pressing on Glass” published in the *IEEE Transactions on Haptics* (licensed under CC BY 4.0) (Nam and Kuchenbecker, 2021). Some paragraphs in this dissertation’s Abstract, Acknowledgments, Introduction, Background, and Conclusion are also adapted from this publication.

This chapter investigates how a finger’s material properties vary across diverse moisture conditions by determining the lumped parameters that best reproduce the finger’s pressing behavior in each condition. As detailed in Section 4.1 and shown in the video associated with the respective article (Nam and Kuchenbecker, 2021), we record real finger deformations from one participant freely pressing on glass under three skin moisture conditions (dry, natural, and moist). The collected data are forces over time and finger-contact images that we post-process to obtain gross contact area. Such dynamic behaviors are simulated in a finite element finger model, where we set the thin outer layer to deform linearly and made the bulk tissue behave based on the SLS-Kelvin model. Optimization enables us to find lumped parameter values that closely represent the behavior of the studied finger in each condition. As described in Section 4.2, these analyses reveal that the bulk tissue gradually softens as the finger changes from dry to moist and that the outer skin layer (epidermis) becomes much softer for the moist finger alone. We also found that the bulk tissue’s damping is highest for the natural finger, low for the dry finger, and almost zero for the moist finger.

4.1 Methods

This section explains our data-collection procedures and how the data were post-processed for comparison with a finite element finger model. We then elucidate the finger model’s design and the numerical simulation conditions. Lastly, we describe how we search for the optimal lumped parameters to represent the finger in each moisture condition.

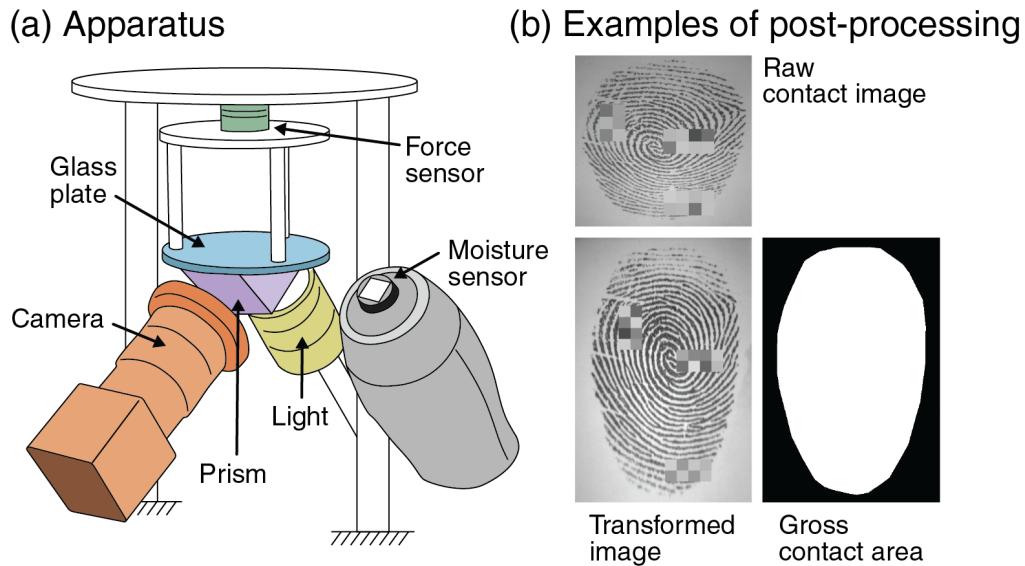


Figure 4.1: (a) Our apparatus for capturing normal forces and contact images over time while a finger is pressing the glass plate (Nam *et al.*, 2020). The nearby moisture sensor measures the fingerpad’s moisture level before and after contact. (b) The processing steps used to extract gross contact area from each raw contact image. Three regions of each fingerprint have been pixelized to prevent personal identification of the participant (Illustration by Nam and Kuchenbecker / CC BY).

4.1.1 Data Collection

We used the previously developed apparatus shown in Fig. 4.1(a) to record finger pressing force and contact area over time. During the finger contact, a strain-based force sensor (Nano17 Titanium SI-32-0.2 from ATI) measures the normal force at a high sampling rate (500 Hz) and resolution (1/171 N). An optical monochrome camera (DCC2340M from Thorlabs) installed below the contact plate captures fingerprint images at 10 Hz. The light intensity contrast between the contact and non-contact fingerprint areas was emphasized by applying the prism-based frustrated total internal reflection (FTIR) principle (Bochereau *et al.*, 2017). The methods by which this apparatus achieves highly contrasted fingerprint images are explained in more detail by Nam *et al.* (2020). Lastly, a capacitive-type moisture sensor (Corneometer CM 825 from Courage + Khazaka electronic) is installed near the contact platform to measure the fingerpad moisture; it measures the moisture value of the outermost layer of the fingerpad in arbitrary units (a.u.) between 0 and 130.

Experiments were conducted with the left index finger of one human subject. Procedures were approved by the Max Planck Ethics Council (HI protocol 18-05B), and the subject provided informed consent. Before each trial, the subject was asked to immerse his fingerpad in isopropyl alcohol and let it evaporate to decrease skin moisture (dry fin-

ger), to do nothing to maintain a moderate moisture level (natural finger), or to perform repetitive physical exercises to sweat naturally (moist finger). The subject placed his fingerpad on the moisture sensor three times at the start of each trial. He then pressed his finger perpendicular to the center of the clean contact platform until the normal force reached 1.35 N, keeping the contact finger nearly parallel to the platform. Of particular note is that we did not restrict the pressing speed or time. Then, a visible cue on a computer screen indicated when to detach the finger. After lifting his finger off the glass plate, the subject pressed three more times on the moisture sensor. This procedure was repeated 45 times (blocks of 15 trials in the order of dry, natural, and moist finger).

4.1.2 Post-processing

Each trial provides three types of data: the moisture measurements, an array of contact force vectors over time, and an array of finger contact images. The six moisture values from each trial were converted to one representative value by averaging. The small lateral forces were ignored, and each trial's normal force was down-sampled to match the frame rate of the camera. As summarized in Fig. 4.1(b), calculating an accurate gross contact area from a single raw contact image requires several processing steps that include geometric image corrections, the binarization of image pixels to identify contact pixels, and the extrapolation of gross contact area from the binary fingerprint image. The first step required camera calibration and the projective image transformation (Zhang, 2000). Next, the binarization was done by intensity thresholding (Davies, 2012), providing the real finger contact area. As the last step, the gross contact area was derived by extracting the convex hull of the pixels considered to be in contact and by multiplying the number of corresponding pixels with the pre-calculated area per pixel ($0.000986 \text{ mm}^2/\text{pixel}$).

4.1.3 Finite Element Model

To simulate the development of the contact area of the human finger pressing into a flat glass plate, we prepared a finite element (FE) finger model in COMSOL Multiphysics. Figure 4.2(a) presents the axially symmetric 3D finger design. This model simulates finger behavior with a much lower computational load than a non-symmetric 3D model, allowing us to repeat the simulations with diverse parameter combinations. The dimensions of its components come from measurements of the subject's finger and the literature, as summarized in Table 4.1. Note that the un-deformed finger was assumed to be an ellipsoid based on its length, width, and depth. The length and width were further turned into the semi-major radius of the ellipse model. The nail's dimensions were also obtained from the subject's finger. The bone's size and location were estimated using relative proportions seen in the X-ray images of a finger (Carver, 2016).

In general, the finger's inner material is soft and suffused with fluid, while the thin outer layer is relatively hard. This knowledge led us to divide the finger into two layers (bulk tissue and epidermis). As the epidermis layer is dense and rubber-like (Adams

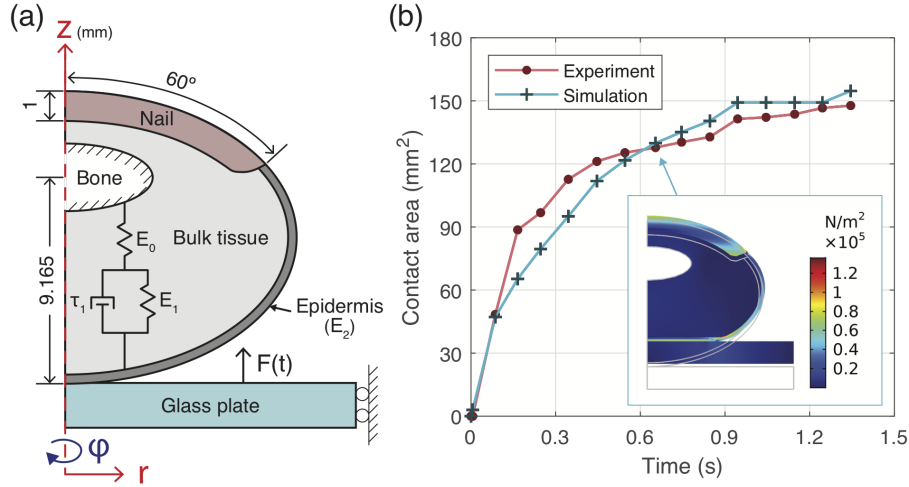


Figure 4.2: (a) Our axially symmetric 3D finger model with lumped parameters and the conditions used for the simulations. (b) One recording of gross contact area over time for a natural finger pressing (the red line) compared with a simulation of the finger model pressing (the cyan line). Here, the model was simulated with the parameters of $(E_0, E_1, \tau_1, E_2) = (140 \text{ kPa}, 20 \text{ kPa}, 0.5 \text{ s}, 2200 \text{ kPa})$; the inset image shows its deformation and von Mises stress at a time of 0.654 s (Illustration by Nam and Kuchenbecker / CC BY).

et al., 2007), we assumed it as linearly elastic (Wu *et al.*, 2008) and assigned it the parameter E_2 . The bulk tissue's material properties were defined to follow the SLS-Kelvin model, in which a linear element (E_0) is connected to a Kelvin-Voigt model (E_1 , τ_1) in series. We implemented this behavior within COMSOL using the SLS-Kelvin model (COMSOL Inc., 2022); we first specified the bulk tissue as a linear elastic material represented by E_0 and added an “external strain” component under the linear component. In one dimension, the external strain is defined via the following ordinary differential equation from the stress equilibrium equation:

$$\sigma = \sigma_{\eta_1} + \sigma_{G_1} = \eta_1 \frac{d\varepsilon}{dt} + G_1 \varepsilon \quad (4.1)$$

where η_1 and G_1 are respectively the viscosity and shear modulus, which allow us to calculate the model components $\tau_1 = \eta_1 / G_1$ and $E_1 = 2G_1(1 + \nu_1)$, where ν_1 is Poisson's ratio. Using the relaxation time τ_1 and $\sigma = \sigma_d / 2$ (half of the deviatoric stress (Marques and Creus, 2012)), Eq. (4.1) can be further transformed to

$$2G_1 \tau_1 \frac{d\varepsilon}{dt} = \sigma_d - 2G_1 \varepsilon. \quad (4.2)$$

Equation (4.2) finally expands to the axially symmetric case with r , ϕ , and z axes such that

Table 4.1: Constant parameter values for the FE finger model.

Entity	Parameter	Value [unit]	Source
Finger	Semi-major radius	10.3 [mm]	-
	Semi-minor radius	6.5 [mm]	-
	Poisson's ratio	0.48 [-]	Fung (2013)
	Density	1000 [kg/m ³]	Maeno <i>et al.</i> (1997)
	Bulk modulus	10 [kPa]	Ayyildiz <i>et al.</i> (2018)
Epidermis	Thickness	350 [μ m]	Fruhstorfer <i>et al.</i> (2000)
Nail	Young's modulus	170 [MPa]	Wu <i>et al.</i> (2002)
	Poisson's ratio	0.3 [-]	Wu <i>et al.</i> (2002)
Bone	Semi-major radius	3.914 [mm]	Carver (2016)
	Semi-minor radius	1.495 [mm]	Carver (2016)
	Poisson's ratio	0.3 [-]	Wu <i>et al.</i> (2002)
	Density	1960 [kg/m ³]	Fletcher <i>et al.</i> (2018)
Glass plate	Young's modulus	90 [GPa]	Gauthier (1995)
	Poisson's ratio	0.2 [-]	Gauthier (1995)

$$2G_1\tau_1I_6 \begin{bmatrix} \partial\varepsilon_r/\partial t \\ \partial\varepsilon_\phi/\partial t \\ \partial\varepsilon_z/\partial t \\ \partial\varepsilon_{r\phi}/\partial t \\ \partial\varepsilon_{rz}/\partial t \\ \partial\varepsilon_{\phi z}/\partial t \end{bmatrix} = \begin{bmatrix} \sigma_{dr} - 2G_1\varepsilon_r \\ \sigma_{d\phi} - 2G_1\varepsilon_\phi \\ \sigma_{dz} - 2G_1\varepsilon_z \\ \sigma_{dr\phi} - 2G_1\varepsilon_{r\phi} \\ \sigma_{drz} - 2G_1\varepsilon_{rz} \\ \sigma_{d\phi z} - 2G_1\varepsilon_{\phi z} \end{bmatrix}. \quad (4.3)$$

Eq. (4.3) was entered as the ‘‘Domain ODE interface’’ under ‘‘Mathematics’’ physics in COMSOL. We assumed all deformations are isotropic and all materials are incompressible.

For simulations, we set the glass plate to press up into the finger and made the bone stationary. This reverse force application provides better structural stability than a finger pressing on a fixed glass plate (Wu *et al.*, 2008). The friction coefficient created between the fingerpad and the glass surface was set as 0.25 (Pasumarty *et al.*, 2011). The actuation information (normal force over time) came from the force trajectory recorded in each of the 45 trials. Therefore, we could simulate the FE finger model with the same force and time conditions as each of the real trials collected in the experiment. At every time step, the software saved the finger's contact area (πr^2) by measuring the contact radius (r). For instance, Fig. 4.2(b) displays the simulated contact area compared with the measured gross contact area for a single trial.

4.1.4 Parameter Search

We seek the four lumped parameters (E_0 , E_1 , τ_1 , and E_2) that cause the model's simulated contact area to evolve in the same way as the contact area measured in each experimental condition. Mathematically, the simulated area at time t_k and normal force F_k is as follows:

$$\hat{A}_k = f(E_0, E_1, \tau_1, E_2, t = t_k, F_N = F_k). \quad (4.4)$$

After simulating the FE model with continuous time $\mathbf{t} \in \mathbb{R}^n$ and force $\mathbf{F} \in \mathbb{R}^n$ measured in the experiment, the area values would be $\hat{\mathbf{A}} \in \mathbb{R}^n$, where n is the number of measured data points for the selected finger pressing trial. We defined the cost function as the mean squared error ($\text{MSE} = \frac{1}{n} \sum_{i=1}^n (\hat{A}_i - A_i)^2$) between the simulated and measured areas ($\hat{\mathbf{A}}$, \mathbf{A}) and looked for the parameter values producing the minimum cost. Our target is to identify the three different parameter sets that represent the three studied moisture conditions (dry, natural, moist). For each one, the objective is to find the parameter values that achieve the lowest sum of MSE values across the fifteen recorded trials ($J_C = \sum_{j=1}^{15} \text{MSE}_C^j$, simulating with force and time input data from the j -th pressing trial in moisture condition C).

We first investigated possible ranges for the parameters by repeatedly simulating the FE model with diverse combinations. Possible values were chosen on the basis of known Young's moduli for the finger's layers (34 kPa for the fatty tissues and 80 kPa for the dermis (Maeno *et al.*, 1997)). We then manually tuned the parameters to identify extreme values for each parameter that caused the simulated area to generate a large MSE. Finally, we set the range of E_0 to be from 50 to 160 kPa, E_1 from 15 to 60 kPa, τ_1 from 0.01 to 0.80 s, and E_2 from 700 kPa to 2200 kPa. Furthermore, we confirmed the possibility of finding optimal parameter combinations within these ranges by computing J_C for each moisture condition at a brute-force grid of parameter combinations.

The search for the optimal parameter values was conducted with particle swarm optimization (PSO) (Kennedy and Eberhart, 1995). This heuristic algorithm is highly suitable for our case because we do not know if our optimization problem is convex. We set the upper and lower bounds as the above-stated ranges and generated five candidate swarms to find the optimal values leading to the lowest cost. The swarms' initial positions were specified near the values generating the lowest cost from the brute-force search at each moisture condition. We ran the PSO algorithm three times in total, where the optimized parameters after each run represent the mechanical behavior of the finger in the dry, natural, or moist condition.

4.2 Results and Discussion

This section first presents the measurements from the human-subject experiment and describes how the post-processed data differ across moisture conditions. Next, it provides

and discusses the sets of model parameters yielded by the optimization process for the three moisture conditions.

4.2.1 Measured Gross Contact Area by Force and Time

Figure 4.3(a) shows the average moisture values recorded from the 45 pressing trials. The means and standard deviations are 37.56 ± 3.34 , 69.31 ± 6.54 , and 105.33 ± 4.93 for the dry, natural, and moist fingers, respectively. The broad overall range and lack of overlap between the three conditions indicates that the experimental methods effectively modified the participant's finger moisture, as desired.

The moisture level was also seen to affect the finger's gross contact area. When compared at the same force levels, the gross contact area was larger when the fingerpad was moist compared to dry or natural (Fig. 4.3(b)). In an ideal case where the finger is modeled as a purely elastic sphere (with no layers, bone, fingernail, or friction), its contact area on a flat plate can be calculated from normal force using a power law such as $A = kF_N^m$, where A and F_N are the gross contact area and the applied normal force, respectively (Delhaye *et al.*, 2014; Johnson, 1987). We fit this equation to the aggregate data from each condition to understand the general trends; the coefficient k increased as the finger's state moved from dry to moist, allowing the moist finger to produce a larger contact area at the same force. The fitted exponent values m were 0.67, 0.68, and 0.50 for the pressing trials of the dry, natural, and moist finger, respectively. They are each close to the theoretical value of $2/3$ (Dzidek *et al.*, 2017b) or the value of 0.538 reported in a similar experiment on the index finger (Warman and Ennos, 2009).

The power law formulation makes sense only if the finger is purely elastic. However, fingers have viscoelastic material properties, so the development of the contact area depends on the rate at which the finger is pressed into the surface. Figure 4.3(c) shows that the participant pressed into the glass at widely varying speeds, taking between about 0.5 s and 2 s to reach the target normal force of 1.35 N across different trials in each condition. Visual inspection of Fig. 4.3(b) hints at lower contact area for the fast finger pressing trials (lines with fewer data points) in the dry and natural conditions, with little variation across the moist trials. For comparison with the optimized FE models, we also calculated the sums of MSE for the power-law fit to each moisture condition's contact area results: $J_{\text{dry}} = 2650 \text{ mm}^4$, $J_{\text{natural}} = 4767 \text{ mm}^4$, and $J_{\text{moist}} = 1807 \text{ mm}^4$.

Meanwhile, it is interesting to note that the theoretical exponent value ($m = 2/3$) is derived from the assumption that purely elastic spheres experience contact without adhesion. We believe that the critical difference in the fitted value for the moist finger ($m = 0.50$) from the other two values is due to a softer epidermis. At low normal force, a soft outer layer causes a larger contact area, decreasing m .

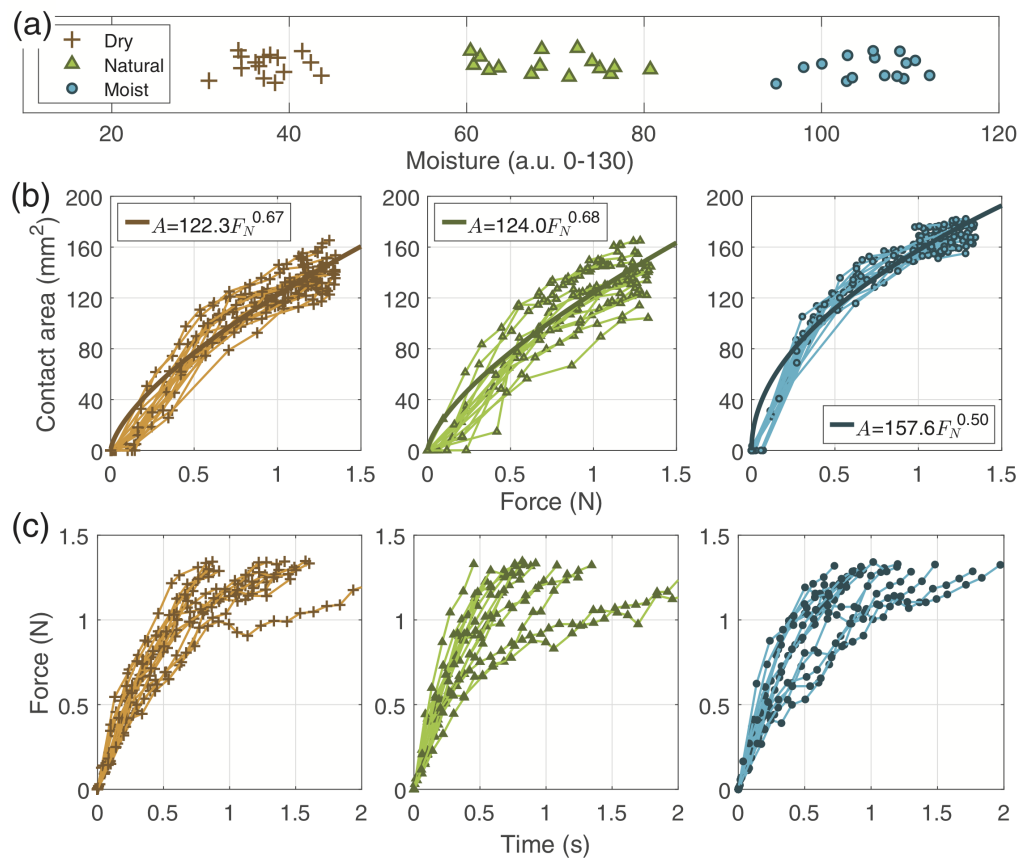


Figure 4.3: Measured data after the post-processing. (a) The moisture values from the 45 trials are clearly distributed into three groups. (b) The way the gross contact area increases as a function of pressing force differs somewhat across moisture conditions; the fitted equation is based on the theoretical relationship between contact area and normal force for an elastic sphere. (c) Within each condition, the subject sometimes pressed quickly and sometimes much more slowly (Illustration by Nam and Kuchenbecker / CC BY).

Dry finger					Natural finger					Moist finger				
E_0 (kPa)	E_1 (kPa)	τ_1 (s)	E_2 (kPa)	Σ MSE (mm ⁴)	E_0 (kPa)	E_1 (kPa)	τ_1 (s)	E_2 (kPa)	Σ MSE (mm ⁴)	E_0 (kPa)	E_1 (kPa)	τ_1 (s)	E_2 (kPa)	Σ MSE (mm ⁴)
95.2	44.3	0.07	1652	2135	155.0	22.0	0.44	1795	2886	160.0	15.0	0.01	700	1255
95.1	44.3	0.07	1652	2142	155.2	22.0	0.44	1800	2919	141.8	15.0	0.01	700	1271
95.0	44.3	0.07	1653	2150	156.7	22.0	0.45	1706	2933	104.7	15.0	0.01	700	1277
94.5	44.5	0.07	1660	2166	155.2	21.7	0.46	1739	2936	160.0	15.9	0.22	797	1350
93.4	46.2	0.04	1669	2293	155.8	22.6	0.44	1740	3050	64.0	15.4	0.03	1719	1352

Figure 4.4: Top candidates for the lumped parameter values found by the particle swarm optimization algorithm, as well as the resulting MSE sums. The dashed lines indicate the boundaries where the sum of the MSE increases substantially compared to the fitting error of the top candidates (Illustration by Nam and Kuchenbecker / CC BY).

4.2.2 Optimized Parameter Values

After running the PSO algorithm, we extracted the top five parameter sets for simulating the finger's pressing behavior in each of the three studied moisture conditions, as shown in Fig. 4.4. The sums of MSE values are all at least 500 mm⁴ lower than the corresponding best-fit power laws shown in Fig. 4.3(b), showing that our finite element model was able to represent the experimental results better than standard theory.

Looking at the optimized parameter values, we found that the bulk tissue's composite steady-state elasticity ($E = 1/(1/E_0 + 1/E_1)$) decreases as the finger becomes hydrated ($E = 30.23$ kPa for dry, 19.27 kPa for natural, and 13.71 kPa for moist). These three values are consistent with those from an experiment by Maeno *et al.* (1997), who found the integrated Young's modulus considering both fatty tissue (34 kPa) and the dermis layer (80 kPa) is around 23.9 kPa. We expect the finger softening may be caused by water filling in the eccrine sweat glands as the finger becomes moister. It is known that sweat gland density in the finger's volar region is the second-highest in the body (after the toe) (Taylor and Machado-Moreira, 2013); the permeated liquid may allow deformations of the surrounding solid tissue mainly in the dermis layer.

The moist finger model had the lowest value (700 kPa) for the Young's modulus of the epidermis layer (E_2), whereas the corresponding moduli for the dry (1652 kPa) and natural (1795 kPa) fingers were similar. It is imaginable that the sweat excreted from the moist finger greatly softens that layer of skin. However, wiping the fingerpad with alcohol seems to reduce the epidermis layer's stiffness only slightly. Nonetheless, it may somewhat harden the bulk tissue, which is much softer than the epidermis. Considering that the sweat glands are located in the dermis, which is part of the bulk tissue in our model, we speculate that the alcohol may remove the sweat not only from the skin's surface but also from the sweat glands themselves. Alternatively, the alcohol may remove skin oils that naturally soften the interior tissue of the finger, or it may cool off the finger enough to change its internal material properties.

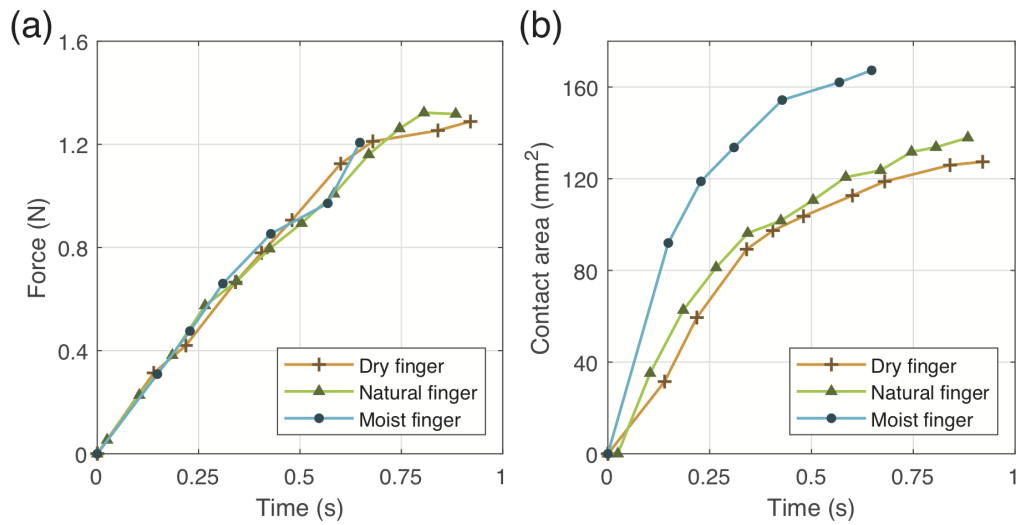


Figure 4.5: One selected trial from each experimental condition. (a) The subject increased his pressing force in a very similar way for all three trials. (b) The resulting contact area over time differs across conditions (Illustration by Nam and Kuchenbecker / CC BY).

To better elucidate the optimal parameter sets chosen for the three conditions, we selected and plotted three experimental trials that had very similar force trajectories over time, as seen in Fig. 4.5. Although the subject pressed in almost the same way, the contact area trajectories differ, with the dry finger showing a slightly lower contact area than the natural finger, and the moist finger achieving a much higher contact area than the other two conditions. Although this plot might lead one to believe that the dry and natural finger have similar parameter values, our optimization results showed distinct optimal parameter sets. The bulk tissue of the dry finger is stiffer (higher composite stiffness from E_0 and E_1) and much less damped (lower τ_1) than the natural finger. The same observation can be seen in Fig. 4.3; although the distributions of pressing force over time are similar for the dry and natural fingers (Fig. 4.3(c)), the distribution of the contact area is broader for the natural finger (Fig. 4.3(b)), implying a higher value of τ_1 . In other words, the natural finger's behavior seems to depend more on pressing rate than the artificially dried finger's behavior does. In contrast, the moist finger's behavior is almost rate independent, with optimization yielding the minimum possible value for τ_1 . Indeed, the contact area trajectories for the moist finger are closely clustered together in Fig. 4.3(b) despite the different pressing force trajectories applied by the subject. We speculate that the repeated exercise performed in the study caused a significant increase in the circulation of blood through the subject's body, such that his finger's tissue rebounded almost instantly after deformation in the moist condition.

4.2.3 Limitations

Although encouraging, this research has some limitations that should be acknowledged. There are non-negligible differences between our FE model and the real finger. First, our axially symmetric 3D finger model cannot precisely simulate the contact area development made by a real finger. This limitation comes from our assumption that the real finger's shape is an axially symmetric ellipsoid, which enabled us to use a more computationally efficient model. Second, the contact angle of the finger varied slightly across trials; our experimental apparatus cannot measure this source of variation, nor does it record the downward movement of the finger itself. Third, the epidermis layer's thickness could be locally different from that of the real finger; we used an average value based on prior research (Fruhstorfer *et al.*, 2000).

Next, there are challenges in precisely calculating gross contact area from our experimental data. Basing the area on a convex hull, which consists of many straight lines connecting neighboring pixels considered to be in contact, can cause a relatively large error compared with the true area if only sparse areas of the skin are contacting. This limitation especially arises at the initial phase of finger pressing. For instance, Fig. 4.5(b) shows that the initial contact area of the natural finger is nearly zero even though the force sensor is registering a small force. We found that this issue happens when the measured force is less than 0.2 N. However, only a few data points were measured in this range, so they had little effect on the MSE sum used for optimization. For higher forces, the number of straight lines defining the gross contact area for the dry finger was almost identical to that for the natural finger, even though the measured areas were somewhat different. We therefore believe that our approach accurately estimates gross contact area even for dry fingers.

Including more measurement data might have enabled us to obtain better-optimized parameter values. Another option could be to conduct the same experiment with more human subjects. However, we encountered a severe time bottleneck running the PSO algorithm, as it conducts hundreds of COMSOL simulations to find the optimized parameter values for only one subject. Although we did our best to decrease the computing time, including running simulations in parallel, it took nearly three weeks of computation to obtain the values reported in this chapter ($2 \text{ minutes/trial} \times 15 \text{ trials/condition} \times 3 \text{ conditions} \times 5 \text{ swarms/round} \times 60 \text{ rounds} = 27,000 \text{ minutes} \approx 19 \text{ days}$). Nevertheless, examining data from other subjects would definitely increase the reliability of the trends observed in our optimized values.

Chapter 5

Effect of Moisture on Friction

This chapter investigates the initial lateral slip between the human finger and a glass surface. Based on previously reported research results, we select three binary contact conditions: the finger's moisture, the pressing time, and the temperature of the contact surface. Under each of the eight resulting contact conditions, the thirteen invited participants repeatedly pressed the index finger of their dominant hand at 0.2 N on a smooth glass plate and then slid it laterally. After the data processing and analysis, we explain the physical differences observed in our friction and contact area measurements as a function of the contact conditions.

Section 5.1 explains the experimental setup, data processing methodologies, and study procedures. In Section 5.2, friction data are shown by contact conditions, and the physical interpretations for the differences in friction by conditions are presented in Section 5.3.

5.1 Materials and Methods

5.1.1 Apparatus

We have built an apparatus that simultaneously records the force vectors and contact images of a finger pressing and laterally sliding on glass over time. As shown in Fig. 5.1, the apparatus mainly consists of a strain-based force sensor (Nano17 Titanium SI-32-0.2, ATI Inc.), a camera (DCC2340M Thorlabs Inc.) with a lens (LM50HC Kowa corp.), a 2.7 mm-thick glass plate (SCHOTT BOROFLOAT[®] 33 (SCHOTT Technical Glass Solutions GmbH, 2020)), a Peltier element, and an LED diode. In the apparatus, we additionally installed a commercial moisture sensor (Corneometer[®] CM 825 w, Courage + Khazaka electronic GmbH), providing a value of sensing between 0 (highly dry) to 130 (highly moist).

Force sensor

The force sensor records force vectors in three degrees of freedom over time by sensing strains between the upper and lower parts. As long as the upper part of the sensor is fixed

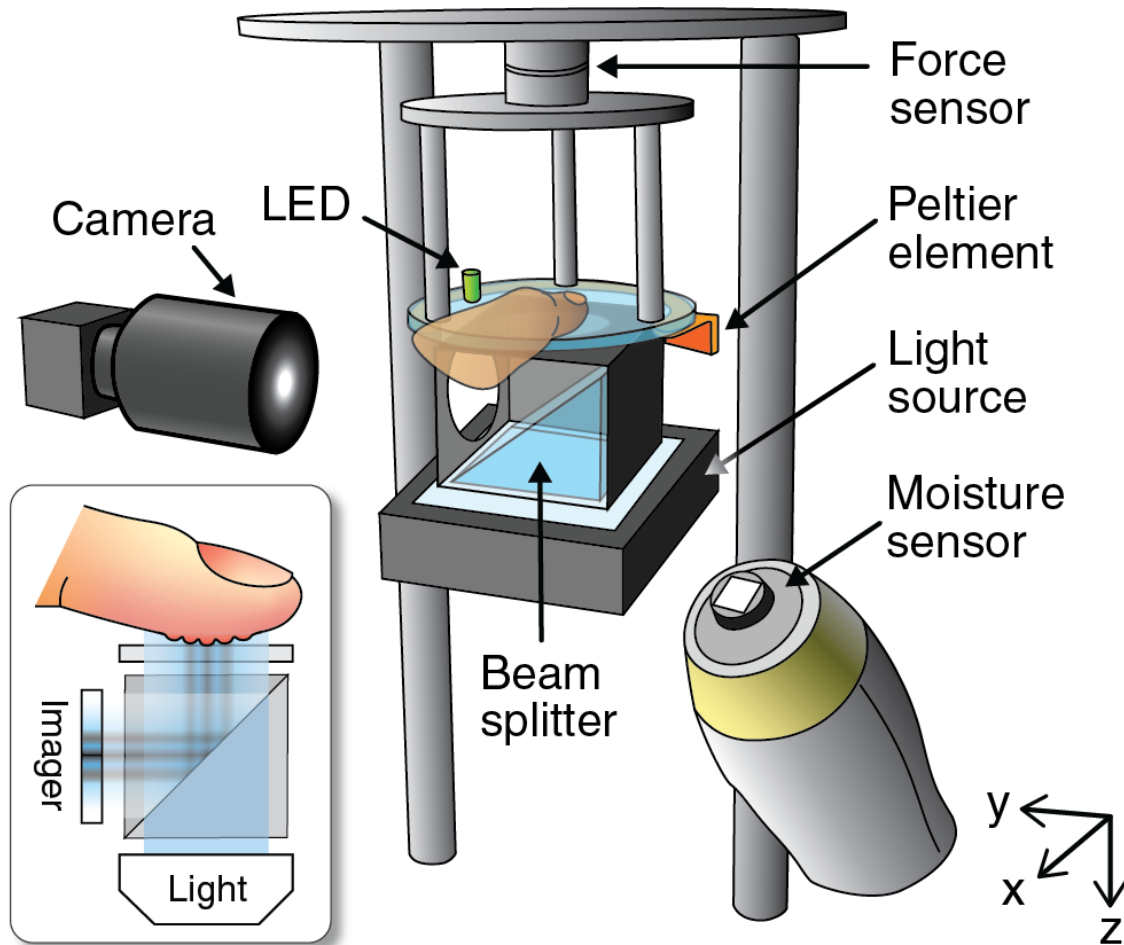


Figure 5.1: A custom-built apparatus to capture the contact images and force vectors during the finger-surface interaction. The inset illustrates the working principle for how this apparatus captures contact area.

to the metal plate above it, a press at the contact platform (a glass plate with three pillars) leads the sensor to record forces based on the measured strains. The sensor was connected to a data acquisition board (PCIe-6321 National Instruments Corp.) installed in the experiment PC, which enabled a custom-made LabVIEW program to record pressing force vectors about 500 times per second.

Heater

We prepared a Peltier element ($12.3 \times 6.2 \times 2$ mm from Laird Thermal Systems), a heat sink, and a custom-designed aluminum plate in the c-shape. The heat sink-attached Peltier element was glued to an extended corner of the aluminum plate (Fig. 5.1), and all elements were tightened to the bottom surface of the glass plate using plastic bolts and

nuts. Finally, we connected the power lines of the Peltier element to a 4.5 V DC adaptor.

5.1.2 Capturing Fingerprint Images

Capturing the images of a finger contacted to the glass plate is based on light reflection and scattering at the contact surface. A controlled amount of light from a light source (KL 2500 LED, SCHOTT AG) shines a finger through a beam splitter and a glass plate. While the finger does not make any contact, the light reflects over the fingerpad and heads toward the camera with the help of the beam splitter. As the distance between the camera and locations on the fingerpad generally decides the light intensity, the center area of the fingerpad produces a brighter intensity than any of its peripheral area (see Fig. 5.2(C)). However, as soon as a contact is made between the fingerpad and the glass plate, the shined light scatters, and therefore, almost no light can get into the camera, producing relatively dark pixels. Binarizing these pixels from a whole fingerprint image will eventually allow us to estimate the real contact area.

To record a video of fingerprint images, we used the software (ThorCam) provided by the image sensor manufacturer. The frame rate has been set to 25.1 frames per second, and the recorded video includes a monochrome image over time with a resolution of 1280×1024 pixels in which the intensity ranges from 0 to 255. In our setup, the area of one pixel corresponds to 0.000687 mm^2 .

5.1.3 Time Synchronization between Images and Forces

The two separated recordings for capturing a finger's pressing forces and the corresponding fingerprint images require data synchronization. To do this, we connected an LED diode to an analog output channel of the data acquisition board and located the LED near the contact platform such that the camera could capture the LED. The LabVIEW program for recording the force vectors was additionally customized to turn on and off the LED periodically. As images captured from the camera contain the LED's on/off status over time, we corrected the time of the recorded images so that the timing of the LED's lighting aligns over time across the two different sources.

5.1.4 Extracting Contact Area from an Image

Our algorithm to extract the contact area from captured fingerprint images is tricky and complicated compared to other previously proposed methods (Nam *et al.*, 2020; Willemet *et al.*, 2021). The main reason for the difficulty comes from the principle of capturing fingerprint images. Our apparatus is taking advantage of light reflection occurring on the fingerpad's surface. Therefore, the closer the fingerpad is to the glass plate, the more light is reflected and goes into the image sensor. This principle helps identify the general deformation of a finger pressed on a plate, but it also causes inequality in

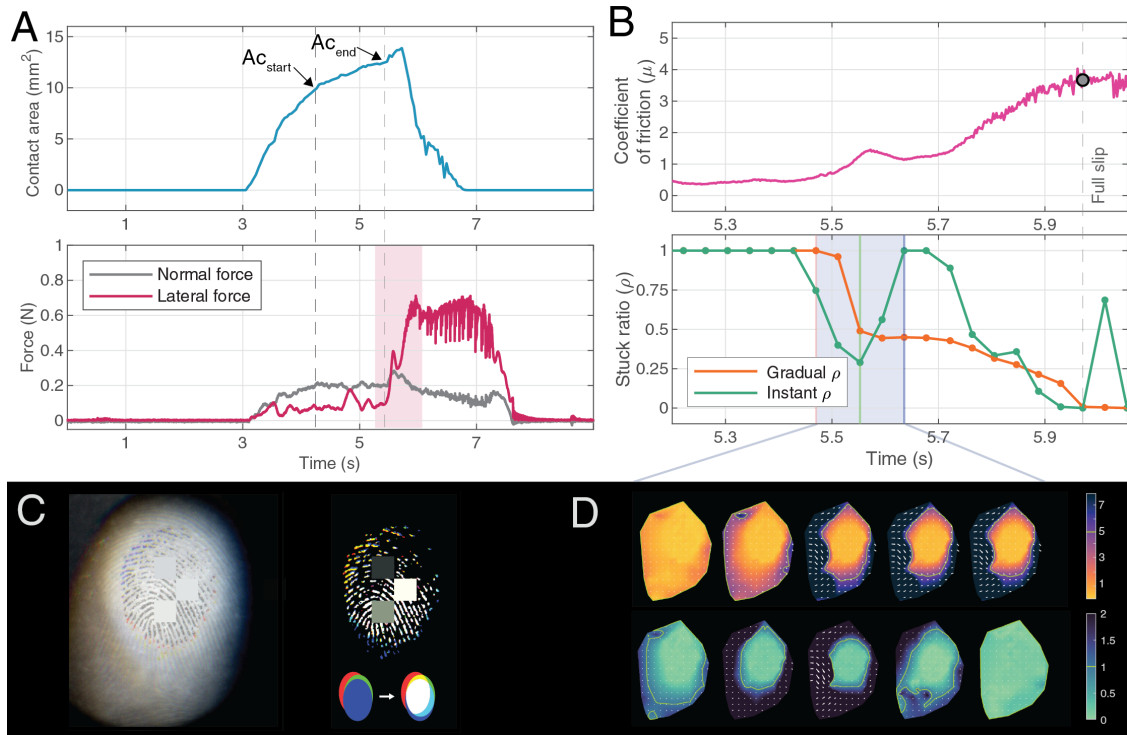


Figure 5.2: Key processed data from measurements of a finger sliding laterally. (A) The change of the real contact area and forces over time, (B) the flow of friction and two types of stuck ratios (ρ_g for gradual stuck ratio and ρ_i for instant stuck ratio), focused at the time of the finger's sliding (the area shaded in pink in the bottom plot of (A)), (C) the captured images and processed contact area images showing the finger's shift across frames, and (D) displacement fields in the five contiguous frames that are shaded in blue-gray in the bottom plot of (B). The fingerprint image on the left side of (C) is composed of three intensity images captured at frames marked with red, green, and blue vertical lines in the bottom plot of (B). In accordance with the color scheme, the first, second, and third images are color-coded in red, green, and blue, respectively. The same method is used to compose the binary fingerprint image in (C) (see the illustration in the bottom right). Note that the color configuration seems opposite between the two images because the contact area's color intensity is inverted. To protect the identity of the participant, three sections were pixelated in the fingerprint images.

intensity. For example, the center of the contact finger appears brighter than its periphery. With this problem, a relatively dark pixel in the center of the finger (i.e., a pixel that should be considered as a contact) is brighter than a relatively bright pixel in its periphery (i.e., a pixel that should not be considered as a contact).

We loaded a recorded video in the form of stacked images over time. The contact area was extracted frame by frame by processing each image. First, we created a two-

dimensional array containing the mean intensity values at each pixel over time for the initial frames when a finger was not yet contacting the glass. Then, this array was further smoothed with a Gaussian filter. Subtracting this array from a stack of original images will produce a stack of images showing relative intensity changes (we call one image in the stack a “relative image”).

In addition to the relative image, we prepared another image indicating the locations of a large gradient in intensity. To produce the image, we used the “imgradient” MATLAB function and binarized it by setting the cut-off value, producing a binary image called “large gradient array.”

Next, for each true pixel in the large gradient array, a small subset of the relative image is created centering at the pixel. Any pixels whose relative intensity is lower than the relative intensity value at the center are considered candidate pixels to be contact pixels. According to our candidate searching algorithm, some pixels near a series of large gradient pixels obtained multiple chances to be considered tentative contact areas. To resolve the problem of the non-even chances, we created a new probability array representing the number of “true” decisions among the total number of the binarization tests.

The final binary array indicating the contact area was extracted from the probability array by taking true for any pixels above a threshold value. In usual cases, the probability gets high if the denominator (the total number of the binarization tests in this case) is small, meaning that the pixel has a higher chance to be detected as a contact. Therefore, we set an adaptive threshold value depending on the value of the denominator. The value is a power function of the denominator, allowing a higher threshold value for the low value of the denominator. After applying the adaptive threshold, the true values in the array indicate where intimate contact is constructed. Lastly, we filled any tiny holes in the detected contact ridge area.

This algorithm is applied to all regions of a captured image. Typically, several regions unrelated to the finger are detected as contacts. To remove these false-positive cases, we investigated only the region where the finger is close to or in contact with the glass plate. Based on the principle that such a region shines brighter due to the short distance to the camera, we took this region and considered binarizing images for the contact area only within it. Lastly, we converted the number of true pixels in the image into a value in square millimeters with the conversion ratio of $0.000687 \text{ mm}^2/\text{pixel}$.

5.1.5 Displacement Fields and Stuck Ratios

We set and track interest points over manually selected image frames. They are from the frame where the finger begins to slide to the frame where it has reached the edge of the contact plate. First, we used the “detectMinEigenFeatures” MATLAB function to find the interest points on the initial image in the selected frames. Then, we tracked the points over frames with “vision.PointTracker” function based on the Kanade-Lucas-Tomasi algorithm (Lucas and Kanade, 1981; Tomasi and Kanade, 1991). Due to the fact

that not all interest points are successfully tracked across frames, only valid points for all frames were used to generate the displacement field. Therefore, we used only points that are valid for all frames in creating the displacement field. To remove trivial noisy movements of the points, we smoothed the position of the points across frames.

We produced two types of the displacement field. The first one is a field map presenting how much each interest point has moved from the first frame to the current frame. The change of this displacement field implies the gradual movement of the contact fingerpad. The second type of field is to show the movement of the points from the previous frame to the current frame, implying the instantaneous movement of the contacting fingerpad. By binarizing each displacement field with a cut-off value, we were able to extract its stuck area. The threshold was selected to be 5 pixels (131 μm) for the gradual displacement field and 1 pixel (26.2 μm) for the instant displacement field. The stuck ratio was then calculated by dividing the stuck area by the whole area encompassing the interest points. The ratios for the gradual movement and the instant movement are symbolized as “Gradual ρ (ρ_g)” and “Instant ρ (ρ_i)”, respectively.

We took three-dimensional force information for the first image frame for which both gradual and instant stuck ratios dropped to near zero ($\rho_g < 0.05$, $\rho_i < 0.10$). Thus, the following image frame is the frame presenting full slip. Because the frame rate of the force sensor is higher than that of the camera, we found ten frames before and after one image frame prior to the full-slip frame and took the mean value. The friction coefficient μ was calculated at this time point as $\sqrt{F_x^2 + F_y^2}/F_z$.

5.1.6 Experimental Procedure

The experiment took place in a temperature-controlled laboratory (at 25°C). First, the participant washed his/her hands with soap and water to remove dirt, oil, and other skin contaminants. We did not treat the fingerpad with anything to make the natural finger. For the dry finger, we developed a custom method for reducing skin moisture. The testing finger was placed in hot water (49°C); the participant waited like this for ten minutes, and then the experimenter wiped the water off the finger. Shortly after this procedure, the finger became very dry due to the moisture evaporation from the finger. With the finger in the natural or the dry condition, the participant measured the moisture level of the testing fingerpad three times with a commercial moisture sensor. Next, the finger pressed the cleaned glass plate up to 0.2 N and continued pressing for the predetermined pressing time (1 s or 10 s). Once the pressing time passed, a signal on the screen notified the participant to slide the finger to the right at 1 cm/s. The average of the measured normal forces before full slip was 0.195 N (SD: 0.098 N). A trial ends with three additional moisture measurements with the moisture sensor. The average temperature in the laboratory was 24.9°C (SD: 0.5°C), and the average humidity was 43.7% (SD: 6.5%). The total duration of the experiment was about 2.5 h per participant.

Thirteen participants (nine women, four men) with a mean age of 33.3 years (stan-

dard deviation, SD: 9.6 years) pressed the glass plate in the apparatus with the index finger of their dominant hand and actively slid their fingers under diverse contact conditions. We carefully selected three binary contact conditions; the finger's moisture (natural or dry finger), the presence of glass heating (about 24.9°C for non-heated glass or about 38.2±1.9°C at the center for heated glass), and the pressing time (1 or 10 seconds) (Fig. 5.3(A)). Therefore, there were eight combinations in total.

The experiment order, including the finger-drying process, was as follows:

1. The **natural finger** pressing for **1 s** on the **non-heated plate**,
2. The **natural finger** pressing for **10 s** on the **non-heated plate**,
3. The **natural finger** pressing for **1 s** on the **heated plate**,
4. The **natural finger** pressing for **10 s** on the **heated plate**,
5. Drying the finger,
6. The **dry finger** pressing for **1 s** on the **non-heated plate**,
7. The **dry finger** pressing for **10 s** on the **non-heated plate**,
8. Drying the finger,
9. The **dry finger** pressing for **1 s** on the **heated plate**, and
10. The **dry finger** pressing for **10 s** on the **heated plate**.

Each participant repeated this procedure five times in each of the eight combinations.

Subject removal

For the data analysis, we could not include the friction data from one female participant. Unlike all other participants, her finger created more sweat after she put it in hot water. We guess that emotional or physiological phenomena led to creating an excessive amount of sweat in this one individual.

5.1.7 Ethics Statement

This research study was approved by the Ethics Council of the Max Planck Society under the Haptic Intelligence Department's framework agreement (F023A). Following an explanation of the procedure, all participants signed a consent form. Participants whom were not employed by the Max Planck Society were compensated 10 € per hour.

5.2 Results

5.2.1 Friction by Contact Conditions

A natural finger pressing for 10 s on the non-heated plate presented the highest friction, and a dry finger pressing for 1 s on the heated plate presented the lowest friction (Fig. 5.3(B)). The longer pressing time led to an increase in friction across all participants. However, the glass heating's influence on friction did not show a straightforward pattern. The three-way analysis of variance (ANOVA) presented that the pressing time and finger's moisture are significant factors affecting friction, as shown in the inset of Fig. 5.3(C).

The long pressing time produces tighter contact between the fingerprint's ridges and the glass plate than the short pressing time. The long-time pressure causes the fingerprint's ridges to conform to the smooth glass plate. Therefore, the roughness of the ridge surface will decrease over time, producing more micro contacts. In addition, the long pressing time contributes to the ridge's occlusion. The occluded ridges allow the sweat to evaporate less and then accumulate, helping increase friction (André *et al.*, 2008; Pasumarty *et al.*, 2011). These interpretations can be related to an increase in friction ($\Delta \text{mean} < 0$) in all of the contact conditions where only the pressing time differs (highlighted with black solid-line boxes in Fig. 5.3(C)).

Furthermore, drying the finger decreases friction consistently in all other contact conditions. In Fig. 5.3(C), the mean of friction has dropped ($\Delta \text{mean} > 0$) if the finger's moisture level becomes dry (highlighted with black dashed-line boxes). This drop is definitely due to a decrease in moisture. The contact area measured by our apparatus highly depends on the amount of moisture, and the area is higher for the natural finger than for the dry finger (Fig. 5.5). It has been reported that the role of moisture on/in the fingerpad reduces the elastic modulus of the stratum corneum (Pasumarty *et al.*, 2011; Nam *et al.*, 2020; Nam and Kuchenbecker, 2021) and even plasticizes it, resulting in the flattening of the ridges (Adams *et al.*, 2013).

However, we could not find a consistent change in friction due to heating of the glass plate, as shown in the black dotted-line boxes in Fig. 5.3(C). For example, there was no heating effect ($\Delta \text{mean} \approx 0$) when a natural finger pressed for 1 s, but for a long pressing duration, friction was reduced by the glass heating. A larger reduction occurred when a dry finger pressed for only a short time ($\Delta \text{mean} = 0.83$). Surprisingly, a long duration of pressing with a dry finger presented the opposite trend ($\Delta \text{mean} = -0.41$). This subtle and complicated effect can be understood better by comparing results of the posthoc tests between subject groups clustered based on the moisture level of their natural fingers.

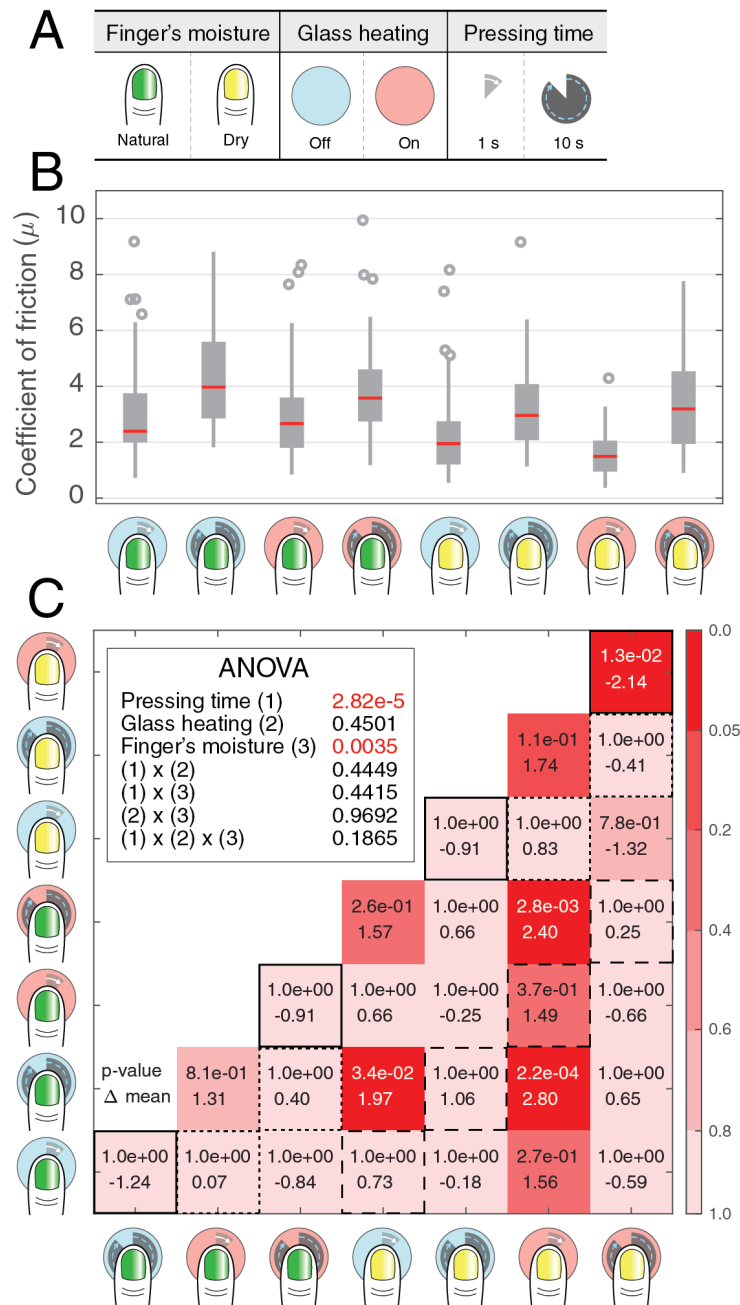


Figure 5.3: Measured coefficient of friction and the associated statistical analyses. (A) Symbols indicating the two conditions for each of three variables. (B) The box plots of measured friction data by the contact conditions. (C) The p-values from the three-way ANOVA test (inset) and the posthoc tests, where the top values in the confusion matrix indicate p-values from Student's t-distribution after applying Bonferroni correction, and the bottom values are the difference between the mean friction coefficient in the y-axis condition and the mean friction coefficient in the x-axis condition.

5.2.2 Analysis between Skin Groups by Moisture

Short pressing with a natural finger

The moisture level of the natural finger varied across participants because they held different amounts of moisture in their skin at the steady-state condition of their bodies. Therefore, we divided the participants into three skin groups (dry skin, typical skin, and moist skin), and each skin group consisted of four participants. The groups are significantly separated from each other in terms of the contact area ($1.56 \pm 1.87 \text{ mm}^2$ for dry skin, $10.91 \pm 7.43 \text{ mm}^2$ for typical skin, and $39.93 \pm 15.75 \text{ mm}^2$ for moist skin) and in terms of the moisture value measured by the Corneometer (30.81 ± 8.20 for dry skin, 51.59 ± 14.04 for typical skin, and 74.46 ± 20.47 for moist skin). When we performed the same analysis presented in Fig 5.3 by the skin group, the ANOVA and posthoc tests revealed analogous patterns to those by all participants (Figs. B.1, B.2, B.3). Figure 5.4(A) presents the changes in the coefficient of friction within each skin group for all the contact conditions, where the last column was extracted from the black dotted-line boxes in Fig. 5.3(C). Likewise, we produced each column by taking the posthoc test with subjects in each skin group and extracting data from the dotted-line boxes of Figs. B.1, B.2, B.3.

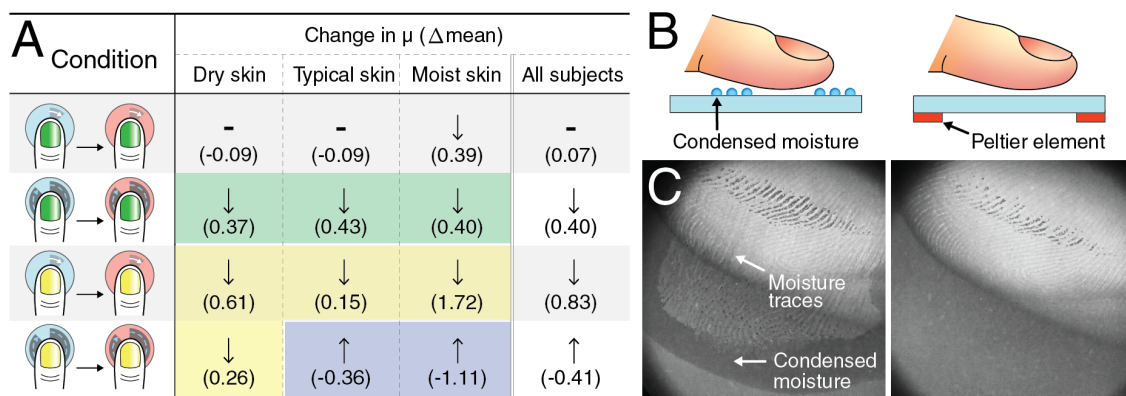


Figure 5.4: (A) Changes in the coefficient of friction caused by heating the glass plate within each skin group are shown as a symbol and a value in parenthesis; the pictograms for the contact conditions are explained in Fig. 5.3(A). (B) Working principle of moisture condensation. (C) Images captured when sliding a highly moist natural finger on the non-heated surface (left) and the heated surface (right).

As shown in Fig. 5.4(A), friction was not influenced by heating the plate when a natural finger pressed briefly, except that the finger from the moist skin group did the same. We believe that a short contact time does not produce a meaningful adaptation of a finger to a heated plate. However, the heating affects friction even in a brief interaction if the contacting finger is highly moist. Because the hot plate continuously evaporates the ambient moisture, the moisture trapped in the occluded ridges of the fingerprints quickly evaporated when the ridges were sliding (see the right figure in Fig. 5.4(C)). On the

other hand, the moisture evaporates much less from the non-heated plate; the condensed moisture trapped in the occluded ridges seems to help increase friction (see the moisture traces shown on the left in Fig. 5.4(C)).

Effect of surface heating

According to our analysis, heating the interaction surface generally decreased the friction. This phenomenon is highly related to the existence of moisture condensed on the glass plate. In principle, moisture condensation occurs if the ambient air is substantially saturated with vapor or it has decreased to its dew point (National Geographic, 2022). Therefore, the condition without surface heating is prone to experiencing moisture condensation on the top surface due to the saturation of vapor from the user's skin and the relatively cooler surface temperature (illustrated on the left side in Fig. 5.4(B)). However, as soon as the Peltier element heats the plate, the heated ambient air causes dew-point-free moisture evaporation, where any moisture present on the surface evaporates, and new moisture does not condense on the glass (the right illustration in Fig. 5.4(B)). The condensation that occurs without surface heating was easily captured by our camera when a natural finger with typical or moist skin pressed on the non-heated glass plate; also as expected, our system did not observe condensed moisture on the glass when it was being heated (Fig. 5.4(C)).

The heating effect contributes to a more dramatic friction decrease if the sliding finger is dry. The small contact area due to the finger's dryness (Fig. 5.5(B)) is already an unfavorable condition to produce friction. Furthermore, the friction reduces with the dry surface by heating. This explanation supports the cases shaded in yellow in Fig. 5.4(A).

Micro stick-slips during partial slip

Surprisingly, the cases shaded in blue in Fig. 5.4(A) present an increase in friction due to heating of the plate, which is the opposite of the pattern in the previously explained cases. First, the dry finger's long pressing time increased the contact area. This situation was observed in the typical and moist skin groups, shown in Fig. 5.6(B). Furthermore, the long pressing time contributes to the tight contact between the ridges and the surface. These two alterations generate a condition for the micro stick-slips of the contacted fingerprints. Figures 5.2(B-D) show fingerprints' micro stick-slips during partial slip. Specifically, the shaded area in the bottom figure of Fig. 5.2(B) is when the partial slip (orange line) starts, where the micro slip and stick (the decrease and increase in the instant ρ) are shown in the green line. Two series of heat maps in Figure 5.2(D) present the visualization for partial slip (top) and the micro stick-slip (bottom) at the respective data points in the shaded area. We found that friction can increase if micro stick-slip occurs during sliding. Its presence was counted more times in the heated plate than in the non-heated plate at the contact condition shaded in blue in Fig. 5.4(A) (15/20 to 13/20 for typical skin and 14/20 to 11/20 for moist skin), and the long pressing time with dry

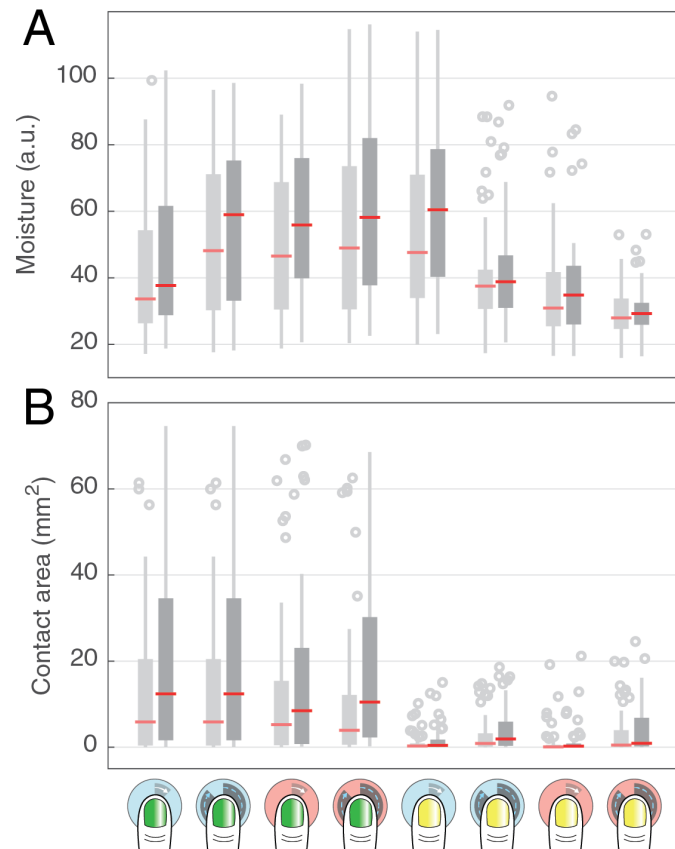


Figure 5.5: (A) The mean moisture values measured by the Corneometer immediately before (left boxplot in each pair) and after (right boxplot in each pair) finger-contact with the glass plate, plotted for all eight conditions. (B) The real contact area is separately shown at the starting time of the finger’s pressing (left boxplot in each pair; $A_{C_{start}}$ in Fig. 5.2) and at the end time (right boxplot in each pair; $A_{C_{end}}$ in Fig. 5.2).

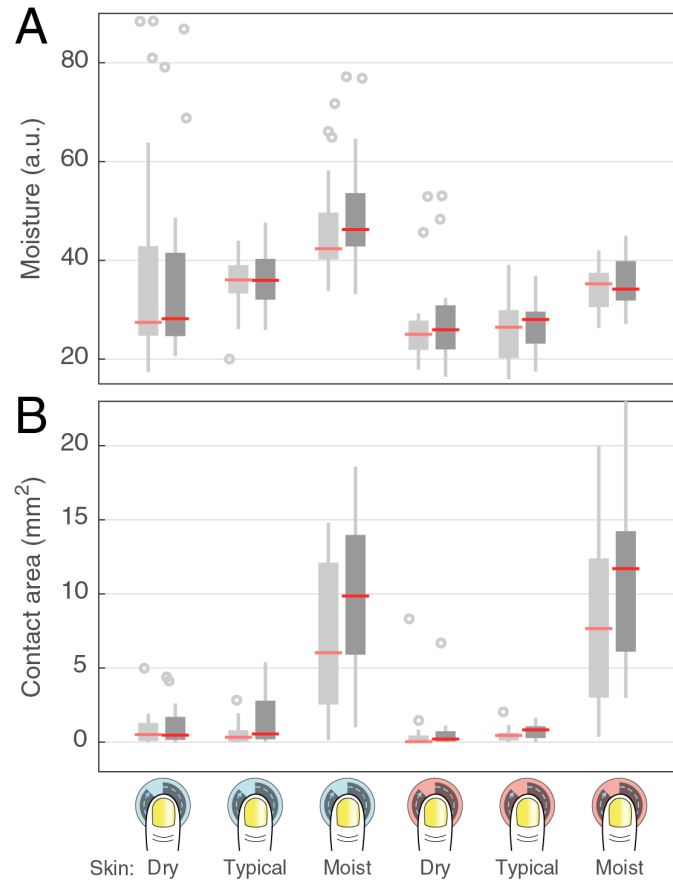


Figure 5.6: (A) The mean moisture values measured by Corneometer, representing the pre (preceding boxplot) and post finger-contact to the glass plate (following boxplot), plotted for the dry finger's three skin groups when pressing for 10 s on non-heated and heated plates. (B) The real contact area separately shown at the starting time of the finger's pressing (preceding boxplot; Ac_{start} in Fig. 5.2) and at the end time (following boxplot; Ac_{end} in Fig. 5.2).

fingers presented the situation more times than the short pressing time (24/20 to 15/20 for dry skin, 28/20 to 18/20 for typical skin, and 25/20 to 21/20 for moist skin). Here, the presence of micro stick-slip was counted if ρ_i fluctuated during the decrease in ρ_g .

Micro stick-slip also occurred in the natural finger's long pressing condition (the green-shaded area in Fig. 5.4(A)). With the help of the micro stick-slip, the measured friction under the natural finger's long pressing is generally higher than the friction under any other conditions. Furthermore, if we compare only the effect of heating, sliding on the non-heated plate provided the micro stick-slip more times than sliding on the heated plate (16/20 to 8/20 for dry skin, 15/20 to 13/20 for typical skin, and 10/20 to 5/20 for moist skin). The reason for the lower friction on the heated plate can be attributed to the effect of moisture traces, as explained in Section 5.2.2.

5.3 Discussion

5.3.1 Relationship between Friction and Stickiness Perception

Our data analysis revealed that a natural finger pressing for a long time can most likely increase friction. According to participants' verbal expressions in the middle of the experiment, most reported that a long pressing time produced higher friction than a short pressing time. The representative expression for the high friction was "sticky", whereas they frequently said "slippery" for the sliding that produced low friction. The contact condition causing the "sticky" expression is well-aligned with the results of our previously published journal paper about the perception of stickiness (Nam *et al.*, 2020) (Chapter 3). Specifically, we found that a long pressing time contributes to creating high impulse, by which people feel stickiness. Similarly, we saw an increase in friction if the contact time was long before lateral sliding of the finger.

5.3.2 Friction and the Surface Temperature

The influence of high temperature on the surface seems to produce different friction changes depending on the interaction conditions. Choi *et al.* (2022) have reported that friction increases when a finger repeatedly slides on a heated surface, mainly due to the reduced stiffness at the stratum corneum. However, our analyses generally revealed opposite results, except for two cases that easily bring about micro stick-slips (Fig. 5.4(A)). Our study focused on the finger's initial slide, where friction largely depends on the initial contact condition. However, Choi *et al.* (2022) have measured the dynamic friction when a finger repeatedly slides over time. This condition can provide the fingerpad with more flattened ridges due to a long time of pressure and accumulated sweat by the occlusion.

5.3.3 Importance of the Fingerprint

The role of fingerprints has long been one of the major curiosities for researchers in haptics, tribology, and neuroscience. The vibrations generated by the fingerprints during surface exploration can help people figure out fine textures (Scheibert *et al.*, 2009; Fagiani *et al.*, 2011). Also, it has been reported that fingerprint furrows can efficiently evaporate excessive moisture and therefore regulate friction (Yum *et al.*, 2020). Our study additionally reveals the role of fingerprints as providing relatively higher friction with the help of micro stick-slips.

Chapter 6

Development of a Transparent Moisture Sensor

In this chapter, we invented and fabricated a sensor to continually measure the moisture level of a fingerpad pressing on a transparent surface. Such a capability would enable creation of a device that simultaneously detects the finger moisture, contact area, and pressing force over time.

Specifically, Section 6.1 describes the sensor's design and fabrication procedures. In the Results section (Section 6.2), the measured impedance under finger contact and non-contact situations is presented. This section also includes measurements of impedance under different finger moisture conditions and pressing forces. Finally, Section 6.3 discusses the data's interpretability and ideas to improve the sensor.

6.1 Methods

6.1.1 The Design of the Sensor

We have built an apparatus for measuring three-dimensional finger contact forces and contact images over time while pressing a finger to a flat glass plate, as shown in Fig. 6.1. Consequently, if the general shape of our sensor matches that of the glass plate, we can measure all of the aforementioned data (i.e., moisture, contact area, and contact force) during finger-surface interactions by substituting the glass plate with the sensor. Taking into account the limited space around the glass substrate, we designed the PCB with a diameter of 78 mm.

The next step is to select an appropriate sensing principle. Most biosignal measurements have been based on resistance (or conductance) or impedance. We choose to utilize impedance-based measurement, taking both resistive and capacitive characteristics into account. Due to its high dielectric constant (Uematsu and Frank, 1980), quantifying the amount of moisture largely affects the capacitive value, and the charge transfer in an electrolyte (e.g., sweat) is best explained by a resistive phenomenon (Mei *et al.*, 2018).

The electrodes are designed to be thin and flat on the glass plate so that they do not interfere with the physical interaction between the finger and the surface. Therefore,

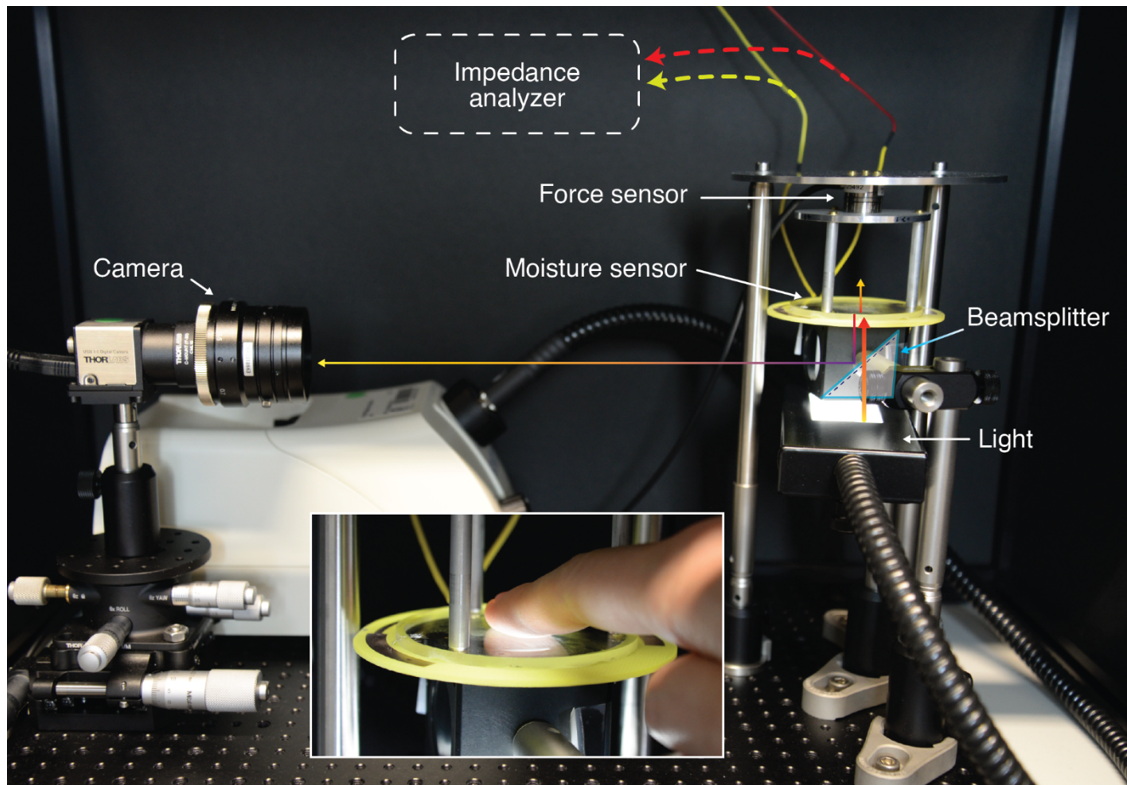


Figure 6.1: The entire characterization system for the moisture sensor. The developed moisture sensor is attached to the previously built apparatus that captures the contact images and force vectors during the finger's pressing. When a finger touches the sensor, as shown in the inset, the wire-connected impedance analyzer measures impedance across a wide frequency range.

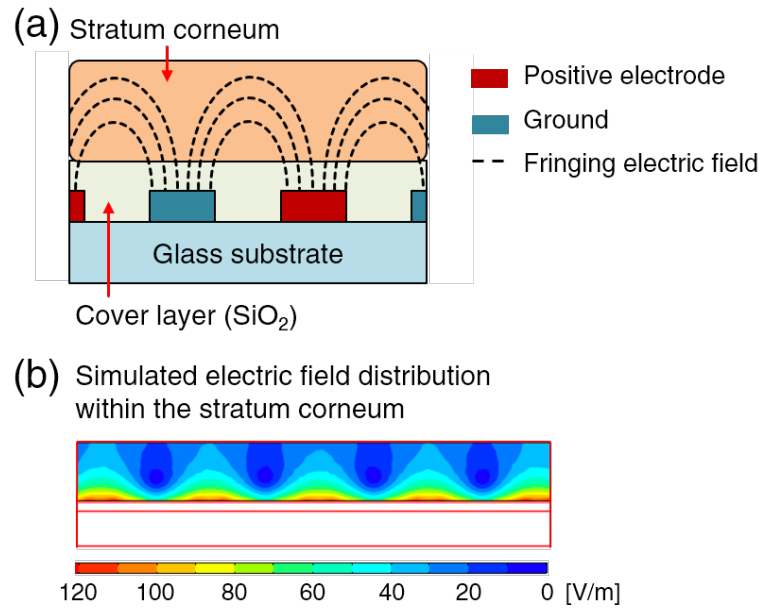


Figure 6.2: (a) The sensing principle based on fringing electric fields formed between electrodes and (b) a simulation of the field distribution in COMSOL Multiphysics.

we fabricate planar inter-digital electrodes (IDEs) and seek to measure the impedance induced by the electric fields at the IDEs (Fig. 6.2). In addition, the size and distance between the electrodes must be determined to capture the finger’s moisture level accurately. First, the sensing area is $6\text{ mm} \times 6\text{ mm}$, which is small enough to be covered by the fingers of people of all ages (Fig. 6.3(a, c)) (Blackstone and Johnson, 2007; Dandekar *et al.*, 2003). This size matches that of another hydration assessment sensor (Constantin *et al.*, 2014). Second, the distance between the parallel electrodes is fixed to $100\text{ }\mu\text{m}$ so that the fringing electric field is less than the ridge width of fingerprints ($350 - 450\text{ }\mu\text{m}$) (Nayak *et al.*, 2010).

6.1.2 Sensor Fabrication

The sensing area consists of two thin, transparent IDEs. First, we prepared a 6 cm-diameter glass plate with a thickness of 2.7 mm (SCHOTT BOROFLOAT[®] 33). This glass has uniform transmission rates of up to 90% across a broad wavelength range (400 – 2000 nm) (SCHOTT Technical Glass Solutions GmbH, 2020). Then, after cleaning the glass plate with ultrasonication, 150 nm-thick IDEs were designed to measure the impedance of a fingerpad. To shield the IDEs and prevent a contact finger from generating an electrical short, we placed an insulating layer (300 nm-thick SiO₂) over the sensing area.

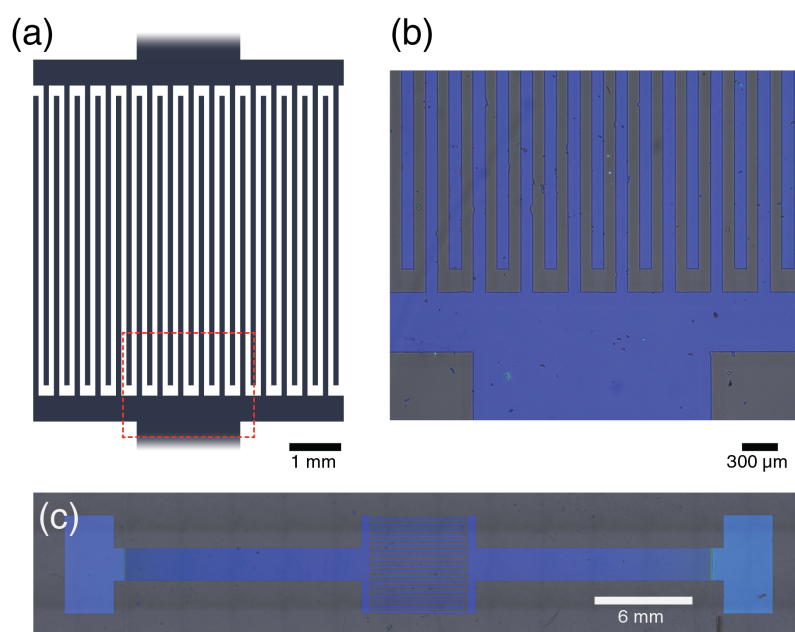


Figure 6.3: (a) An illustration of the sensing area, (b) a microscopic image of the fabricated electrodes, and (c) a top view of the whole fabricated electrodes, where the relative brightness of the two terminals indicates the absence of a cover layer.

The micropattern of IDEs can be created using direct laser lithography. Figure 6.4(a)-(f) illustrates all the steps for the positive photo-resist (PR) mask preparation. The mask is composed of two PR layers (Fig. 6.4(a)). The bottom layer is a lift-off resist (LOR 3A from Micro CHEM), making removing the two resists easier. The resist uniformly spread out on the substrate by spinning the substrate at 5200 rotations per minute (rpm) for 45 s with an acceleration of 10000 rpm/s. The resist and the substrate were then baked on a hotplate for two minutes at 190°C (Soft-baking process). For the upper resist layer, AZ ECI 3027 (Micro chemicals) was spin-coated at 4500 rpm for 30 s with 12000 rpm/s acceleration and then baked on a hotplate for two minutes at 120°C. Later, these PR layers would be dissolved solely in the laser-exposed region. The laser tip passed the preset area designed using a drawing program (KLOÉ's design software) (Fig. 6.4(b)). After the laser exposure, we placed the sample again on the hotplate for two minutes at 100°C (post-exposure baking step). After that, the sample was immersed for 120 s in AZ 726 MIF developer. After the sample was rinsed with deionized water and dried with nitrogen, only the light-exposed regions were etched (Fig. 6.4(c, g)). When placed on a hotplate at 170°C for two minutes, the PR structure became rigid (hard bake). Note that the sidewalls of the lift-off layer are more eroded than the upper layer, resulting in the separation of the indium tin oxide (ITO) material deposited subsequently on top (Fig. 6.4(h)) (KAYAKU Advanced Materials, 2019). Next, a sputter uniformly

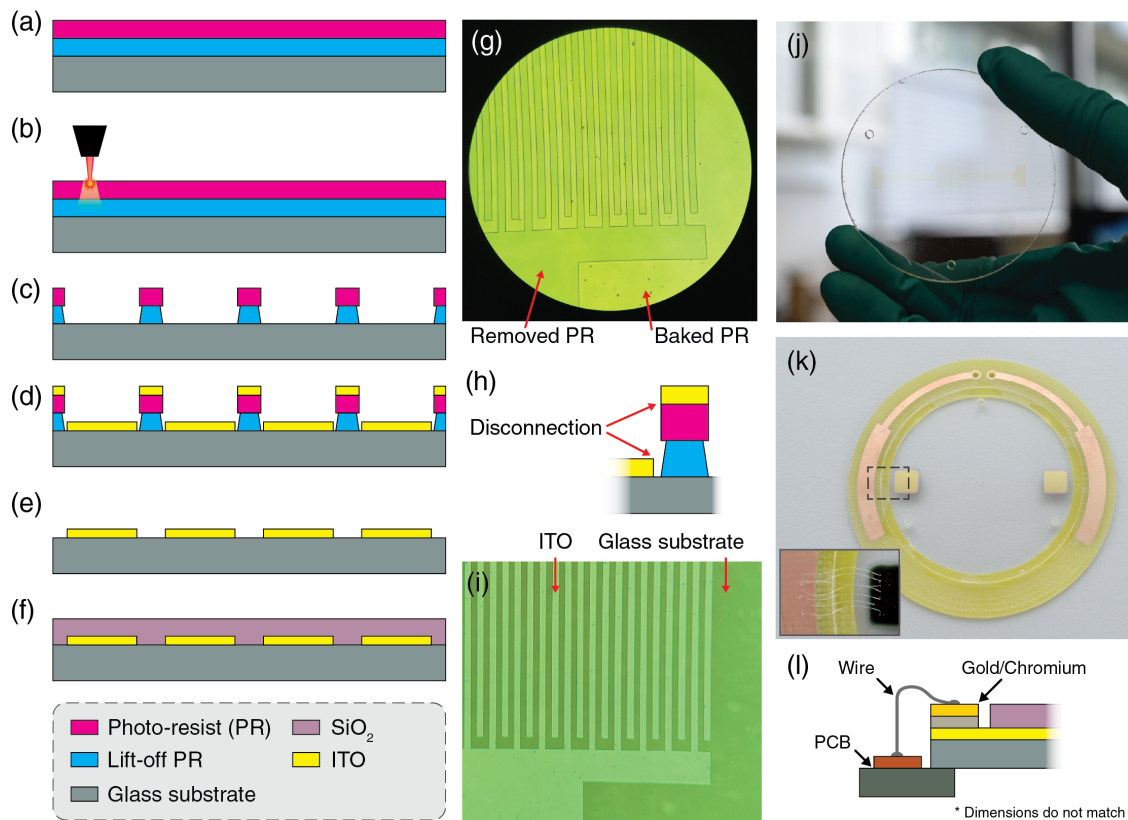


Figure 6.4: Our sensor's fabrication processes and photographs. (a) – (f) Direct laser lithography allows us to produce micropatterned electrodes. (g) The developed photo-resist layer can be observed using an optical microscope. (h) Erosion on the wall of the lift-off photo-resist (PR) allows indium tin oxide (ITO) to be disconnected, resulting in (i) clean edges of the ITO pattern after the lift-off procedure. As a result, (j) a highly transparent layer of ITO has been deposited. (k) The sensor sample is adhered to a custom ring-shaped printed circuit board (PCB), and (l) both terminals of the electrodes were then coated with gold/chromium and connected to the PCB through multiple electrical wires.

deposited ITO with a thickness of 150 nm (Fig. 6.4(d)). The patterned ITO electrodes were left on the substrate after the PR layers were removed using a Remover PG solution (MicroChem) (Fig. 6.4(e, i)). The top surface was then cleaned and coated with SiO₂ at a thickness of 500 nm, except for the terminals of the IDEs.

The terminals of the deposited electrodes must be securely connected to an external measuring instrument. Due to their small thickness and poor adherence to the substrate surface, however, they can be easily torn if the terminal region is directly soldered to an electrical wire and external forces are applied to the wire. To address this issue, we relocated the soldering point to an area of copper cladding on a printed circuit board (PCB; fabricated using an LPKF ProtoMat D104) and made a separate electrical connection between the other region of the copper plate and the terminal (see the ring-shaped PCB in Fig. Sensor:fig:process(k)). LOCTITE 401 from Henkel was used to adhere the PCB to the bottom of the sensor sample.

For a better electrical connection between the IDE's terminal and a region on the copper plate, the terminal region requires extra metal depositions. Therefore, we deposited 10 nm of chromium using a sputtering system (LEICA EM ACE600) because it can improve the adhesion between the sandwiching surfaces. We subsequently sputtered a 120nm-thick gold layer, which has a lower sheet resistance (see two gold squares in Fig. 6.4(k)). Multiple thin aluminum wires (diameter: 33 μm) were used to connect the gold/chromium deposited terminal and the copper plate using a wire-bonder (HB 16 from TP). Figure 6.4(k) illustrates the completed transparent moisture sensor attached to the PCB. The resistance between each gold layer and the printed circuit board was less than 1 Ω . Finally, the tip of a thick electrical wire is soldered to each of the PCB's two holes.

6.1.3 Impedance Measurement and Circuit Optimization

We investigated the change in impedance based on electrochemical impedance spectroscopy (EIS) in order to determine an equivalent electrical circuit for the sensor and the hydrated outer layer of a finger (Barsoukov and Macdonald, 2005; Macdonald, 1992). We then connected our moisture sensor to an impedance analyzer (MFIA from Zurich Instruments). We configured the impedance analyzer to generate sinusoidal voltage signals of 3 V peak-to-peak at 200 logarithmic frequencies over a broad frequency range. One frequency sweep measurement took approximately five seconds. By evaluating the shape and size of the impedance measurements plotted in the complex plane, EIS studies provide methods for identifying an equivalent electrical circuit. MATLAB's Zfit function derives the optimal coefficients for the circuit's electrical components (Jean-Luc Dellis, 2021).

6.1.4 Measurement with a Human Finger

To validate the independent effects of pressing force and moisture on impedance, we performed frequency sweeps under controlled finger conditions. First, the experimenter conditioned his fingerpad to either dry, natural, or moist. For conditioning the dry finger, it was cleaned with alcohol and thoroughly dried with air. For the moist finger, the experimenter exercised by doing jumping jacks and was sweating naturally. Each finger moisture condition was ensured with a value measured from the Corneometer. In terms of the value of the Corneometer, a dry finger is 35 – 45 (arbitrary unit), a natural finger is 65 – 75, and a moist finger is 95 – 105; these values span almost the whole moisture range (0 – 130) of the moisture sensor.

The experimenter sat in front of the apparatus in the experimental room (23°C, relative humidity of 40%) and conditioned his left index finger to be dry. Then, the moisture of the fingerpad was measured three times with the Corneometer. Next, the subject applied a normal force of 0.5 N to the sensor with his finger (Fig. 6.1). During pressing, the impedance representing the sensor and the fingerpad was measured across a wide frequency range (200 logarithmic frequency points between 1 kHz and 1 MHz). After completing the impedance measurement, the subject measured the moisture of their fingerpad three more times. The aforementioned procedure was repeated with natural and moist finger conditions and at normal force values of 1.0 N and 1.5 N for a total of nine conditions.

6.2 Results

6.2.1 Finding the Equivalent Circuit

When plotted in the complex plane, the impedance measurements of the sensor drew a half circle for a frequency sweep. This shape can be represented by a simplified Randles circuit (a parallel RC circuit coupled to a series resistance; see the circuit in the inset of Fig. 6.5(a)) (Abbas *et al.*, 2016). On the basis of fitting the circuit model to the impedance data, the optimal values of the electrical components produce consistent results with minimum variance, as depicted in the inset of Fig. 6.5(a).

Nonetheless, the finger's contact with the sensor generated different impedance readings (Fig. 6.5(b)). At low frequency, both the imaginary and real parts of the impedance were significantly different from those of the impedance measurement without contact. (refer to Fig. 6.5(b) for the direction of the input frequency ω). A circuit model corresponding to the measured impedance consisted of a parallel CPE and R circuit coupled in series with an additional resistance, where CPE stands for constant phase element.

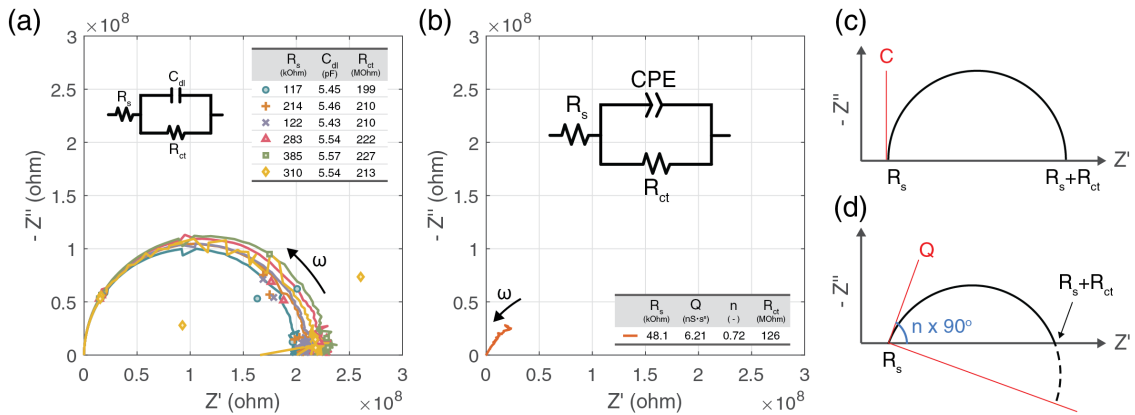


Figure 6.5: Impedance measurements are shown in the complex plane, with the equivalent circuit and optimal component values. (a) The left figure presents the results when the impedance analyzer measures the sensor, and (b) the middle figure shows the results when a natural finger presses the sensor with 1.0 N. The used frequency range was between 1 Hz and 1 MHz. (c,d) The representation of a typical impedance graph for the circuit model depicted in (a) and (b) is shown in (c) and (d), respectively.

6.2.2 Impedance Measurements of a Human Finger during Pressing on the Sensor

Figure 6.6 presents measured impedance values conditioned by the finger's moisture and pressing force, where the values are plotted in the complex plane. The trajectory length of the values measured with a dry finger was the longest across the three levels of finger moisture, and it reduced as finger moisture increased. In addition, the length decreased as the finger's pressing force increased. The length change was more reliant on moisture than pressing force. The angle between the line created by impedance at high frequencies and the y-axis was increased by moisture (see α in Fig. 6.6(a)). However, the angle did not significantly differ among pressing forces under the same moisture condition.

In accordance with the equivalent circuit model depicted in Fig. 6.5(b), we optimized the circuit values with the measured impedance. Table 6.1 displays the optimized parameters. The calculated impedance using the parameters is also plotted as a red line in each figure of Fig. 6.6. Root-mean-square errors (RMSEs) between observed and calculated impedance values are shown in the second last column of Table 6.1. In general, increased moisture reduces R_s , n , and R_{ct} , but increases Q . Unfortunately, the trend among force conditions is uncertain.

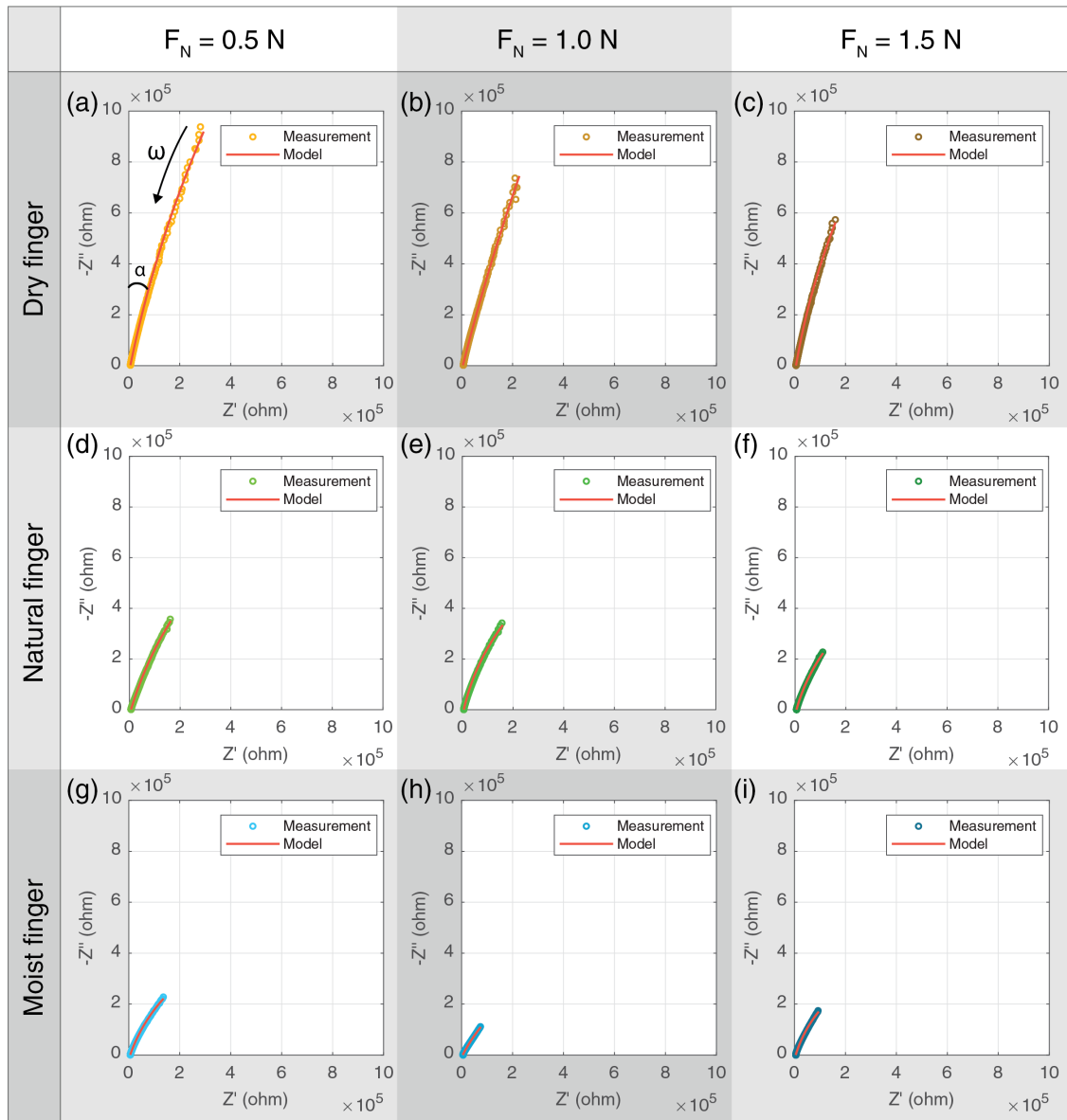


Figure 6.6: Impedance measurements across a range of frequencies (1 kHz – 1 MHz), plotted by finger moisture and pressing force.

Table 6.1: Optimal circuit parameters determined by fitting the circuit to impedance measurements, RMSE between the observed and calculated impedance, and the real part of the impedance observed at 1 MHz.

Finger moisture	Normal force (N)	R_s (k Ω)	Q (nS·s ⁿ)	n (-)	R_{ct} (M Ω)	RMSE (k Ω)	Real(Z) at 1 MHz (k Ω)
Dry	0.5	6.00	0.493	0.872	9.23	5.09	6.65
	1.0	4.68	0.799	0.843	17.5	2.89	6.64
	1.5	6.00	0.680	0.893	5.71	2.86	6.17
Natural	0.5	6.00	1.97	0.816	2.79	2.05	6.25
	1.0	6.00	1.37	0.860	1.71	2.50	5.85
	1.5	5.25	2.70	0.829	1.40	1.35	5.73
Moist	0.5	5.41	3.56	0.789	1.21	1.22	6.04
	1.0	4.18	15.8	0.700	1.14	0.859	5.76
	1.5	4.80	3.91	0.813	0.958	1.32	5.54

6.3 Discussion

6.3.1 Interpretation of Optimized Parameters

First of all, the simplified Randles circuit describes electrochemical reactions of electrolytes (Randles, 1947). Therefore, the interpretation of this circuit is enhanced when there is simply an electrolyte between electrodes. However, the circuit representing our sensor takes into account electrochemical interactions of all materials in the fringing electric field, such as the insulating cover layer, sweat, skin, and the air. Therefore, we believe that the optimized parameters should not be interpreted as the electrochemical responses of an electrolyte to input voltages.

Traditionally, R_s denotes the resistance to the movement of an ion in an electrolyte. In the case of our sensor, the optimized R_s can include both the resistive movement of ions in eccrine sweat and the resistance of the thin electrodes. If a finger is not in contact with the sensor, R_s can be an integrated resistance from air and electrodes. Because the resistance of air is higher than that of sweat, it makes sense that moisture would reduce R_s (See Table 6.1). Moreover, R_s should decrease when the normal force increases, since an increase in force causes the contact area with sweat to expand. This trend can be observed by reading the real part of impedance at 1 MHz (the last column in Table 6.1). Here, an ideally optimized R_s should be close to the real part of impedance at an extremely high frequency as both values reflect a horizontal shift of the impedance graph from the zero point.

A CPE is utilized to represent an imperfect capacitor, which is prevalent in real-world systems (Orazem and Tribollet, 2017; McAdams *et al.*, 2006; Kalia and Guy, 1995). It seems that such a component is created in our system from the standard pure capacitor

when the sensor is pressed by a finger (See Fig. 6.5(a,b)). Therefore, we believe the outermost layer of a finger and sweat contribute to the formation of the CPE. Q , a component composing CPE, can be thought of as the capacitance of the sensing area because both C and Q values contribute to the enlargement of a semi-circle (See Fig. 6.5(c,d)). Consequently, it is logical that moisture increases the Q value.

n is the other component that represents imperfect capacitance in the sensing region. Importantly, this value is related to the angle (α) that an impedance graph draws at zero point (See how n determines the angle α in Fig. 6.5(d)). The optimal n values in Table 6.1 decrease as moisture content increases, but there is no significant difference across forces. Similarly, the angles in Fig. 6.6 demonstrated a sharper distinction between moisture conditions than the forces.

Lastly, R_{ct} is known as charge transfer resistance. This is closely related to the ionization of metal electrodes (Mei *et al.*, 2018). Given that our sensor's electrodes are insulated by a SiO_2 layer, this resistance must be extremely large. Therefore, the optimized R_{ct} values are approximately 1000 times larger than R_s (Table 6.1). Assuming a small amount of metal ionization occurs, the R_{ct} value should be dependent on the contact area and moisture. Consequently, the decrease in R_{ct} in Table 6.1 could be due to an increase in moisture.

6.3.2 Continuous Measurements

Continuously reading impedance at 1 kHz can be a simple method for providing continuous moisture measurements. As demonstrated in Fig. 6.6, the value of the impedance at 1 kHz actively shifts according to moisture and force. A change in pressing force can present a change in distance to the zero point in the complex plane. Furthermore, an increase in skin moisture produces an increase in angle (α) in addition to a decrease in length. Therefore, only a shift in angle without any length change implies a moisture change without fluctuations in pressing force.

6.3.3 Preventing ITO from Delaminating

Long-term use of the developed sensor resulted in the delamination of the electrode (ITO) layer from the substrate. As indicated in Fig. 6.7(a), we were able to identify the areas of delamination. In most cases, the damaged locations were along the inter-digital ITO electrodes. Once these locations have been delaminated, the invasion of sweat during finger contacts renders the surface more vulnerable. This finding implies weak adhesion between the ITO layer and the substrate. Second, we thought the relaxation of residual stress might have caused the ITO layer to buckle and delaminate.

To improve the adhesion, we carefully cleaned the substrate and coated the entire surface with SiO_2 to reduce surface roughness. The coating thickness was 300 nm (Fig. 6.7(a)). Even if the adhesion is sufficiently high, residual stress can cause delamination in the end. This difficulty can often be resolved by annealing the sample. We

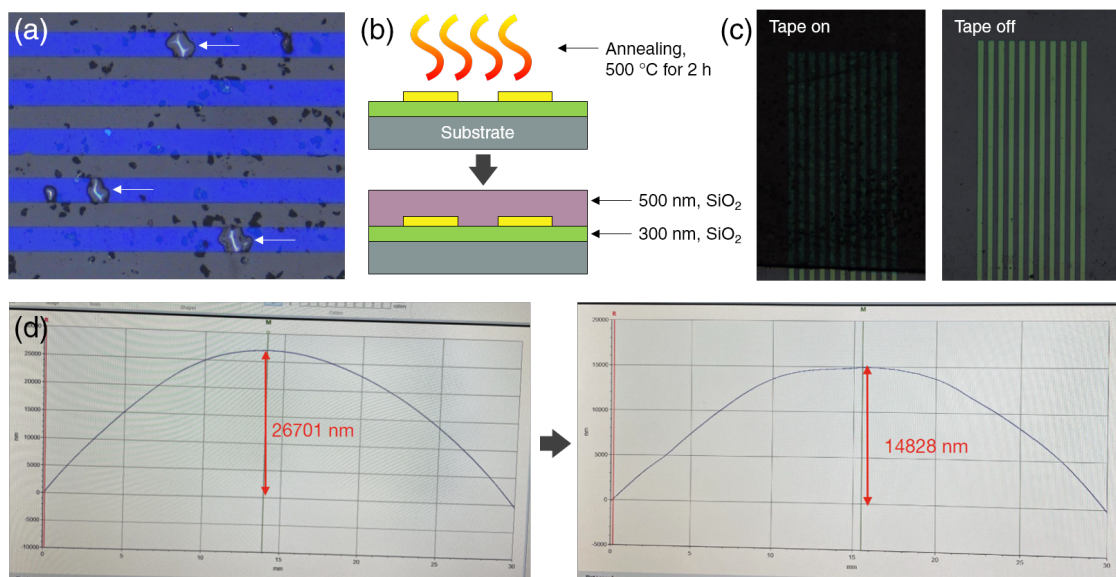


Figure 6.7: (a) Weak adhesion between the ITO layer and the glass substrate causes delamination to spread over time. (b) To prevent this problem, we coated the substrate with SiO₂, conducted annealing, and thickened the insulating cover layer. (c) A tape removal test revealed that the adhesion between the ITO layer and the substrate had improved. (d) The removal of residual stress from layers was enhanced by annealing.

first carried out fabrication steps until the preparation of the ITO layer. Next, we placed it in an oven at 500°C for two hours to anneal it (Fig. 6.7(b)).

To test the effectiveness of annealing, we prepared a tiny wafer and coated its surface with 150 nm-thick ITO. Using Bruker's Dektak, we then measured the height profile of the wafer before and after annealing. Fig. 6.7(d) demonstrated that annealing flattened a wafer that was previously more deformed due to the ITO's residual stress. As the last step, we increased the sensor's insulation thickness to 500 nm (Fig. 6.7(b)).

We performed a Scotch tape test on an old sample and a new, improved sample to see whether the adhesion had been enhanced. We attached a piece of the tape to the surface of both samples and removed it in the same manner. We confirmed that the Scotch tape was able to remove some electrode components from the old sample (not shown), but it was unable to remove any components from the new sample (Fig. 6.7(c)), even when the test was repeated. Thus, we believe the reported methods can be used to successfully fabricate transparent moisture sensors for future investigations of finger-surface interaction.

Chapter 7

Conclusion

7.1 Summary

Given the high rate at which humans contact everyday objects, the fact that skin naturally sweats, and the deep insights that earlier researchers have demonstrated about finger-surface interactions, there is still a need for further research into finger mechanics and the finger's characteristics during interactions. A negligible amount of moisture excreted from eccrine sweat glands allows people to feel stickiness. Additionally, moisture hydrates a finger, which softens its constituent elements. Moisture has a crucial role in friction enhancement. It contributes to the formation of a finger's contact area and facilitates the formation of micro stick-slips. The invention of a transparent moisture sensor that provides continual readings has made it possible to quantify sweat excretion in response to a variety of physical and psychological stimuli, albeit with room for improvement.

Recent technological advances in optics have created an opportunity to quantify the impact of minute changes in moisture content. Until the late 1990s, the primary approach for researching the tribology of human skin was measuring force with strain gauges, which provide only one-dimensional information. However, a high-resolution camera with a fast frame rate and the reflection-based contact area measuring technique, such as FTIR, have enabled two-dimensional measurements during finger-surface interactions. In addition, the evolution of computer-vision algorithms and hardware's computing power enabled us to extract more significant information from data in less time.

Taking advantage of this evolution, I was able to investigate the effects of moisture on the perception of stickiness, friction of a finger, and its material properties. I also developed a moisture sensor based on direct laser lithography, which is also an example of cutting-edge optics technology. With this overview, the following text summarizes the methods and findings of each chapter. This dissertation ends with a discussion of future work.

7.1.1 Influence of Moisture on Stickiness Perception

In Chapter 3, we investigated the physical variables that affect the perception of light stickiness. A custom-made apparatus recorded 3-DoF forces over time, contact area over time, and the moisture level of the subject's fingerpad before and after each trial. The recorded data yielded sixteen physical variables, including RMS forces in the three directions, impulses in the three directions, and finger detachment rates. Based on the data from a total of 324 trials by nine participants and their corresponding stickiness ratings, we computed Spearman's correlation coefficients both within and across subjects. We found that the finger's predetachment pressing time (t_{hold}), the time taken for the finger to detach (t_{pull}), and the impulse in the pressing (normal) direction during the finger detachment after the normal force changes sign (I_z) were significantly related to stickiness. We believe that a longer pressing duration caused a larger impulse during the detachment of the finger from the glass surface and thus a more vivid stickiness sensation. Overall, our results imply that perceptual stickiness may be different from mechanical stickiness.

7.1.2 Influence of Hydration on the Material Properties of the Finger

Chapter 4 used careful experimental measurements and a lumped-parameter FE model to investigate how the material properties of the human finger vary with moisture. After bringing the subject's finger into a dry, natural, or moist state, we recorded its moisture level, pressing normal forces over time, and contact images over time with a custom-made apparatus. The finger-contact images were further processed to calculate gross contact area over time. We then generated an axially symmetric 3D FE finger model with a rigid bone, a deformable fingernail, SLS-Kelvin lumped parameters for the viscoelastic bulk tissue, and a linearly elastic outer layer (epidermis). This model simulates contact area development when the finger is dynamically pressed into a glass plate with a specified force trajectory over time. Particle swarm optimization for each moisture condition identified the values of the four lumped parameters that best match the set of fifteen experimentally measured contact area trajectories for that moisture condition. The three sets of optimized values show that the finger's bulk tissue becomes softer as it becomes hydrated, that Young's modulus of the epidermis is the lowest in the moist condition, and that damping is highest in the natural condition. We believe that these research results can help elucidate why human fingers are so good at securely grasping flat objects in diverse conditions.

7.1.3 Effect of Moisture on Friction

In Chapter 5, we set different finger-surface interaction conditions (finger moisture, pressing time, and glass heating) and measured friction when a finger begins full-slip. Our analysis from the extensive human subject study with thirteen participants revealed that a long pressing time increases finger friction significantly, whereas drying finger de-

creases friction. This study suggests that the contact area formed primarily by moisture has a considerable impact on the occurrence of friction and that the occlusion effect is also crucial. In general, heating the contact surface produces a slippery surface, but in certain circumstances, it can enhance friction and produce micro stick-slips. Overall, micro stick-slips enhance friction. This phenomenon implies that fingerprints are important in creating high levels of friction between the skin and manipulated objects.

7.1.4 Development of a Transparent Moisture Sensor

We created a transparent moisture sensor capable of continuous measurements. We deposited transparent and thin inter-digital electrodes on a glass plate and measured the sensor's impedance when materials contacted the sensor surface. On the basis of electrochemical impedance spectroscopy, we were able to ascertain the equivalent circuit not only for the sensor but also for moist finger skin contact. A change in moisture results in a change in the measured impedance value. In addition, reading the impedance value at 1 kHz provides continual data across time. By placing this sensor inside an apparatus that captures images of a contacting finger and its pressing forces over time, it will be possible to record the amount of sweat secretion under various pressing situations.

7.2 Future Work

Signals from mechanoreceptors are closely related to the perception of finger contacts (Edin, 2004). Recently, neuroscientists have begun measuring tactile signals as the local compressions and deformations of a finger's skin (Delhayé *et al.*, 2021a). If this method of signal sensing is standardized, it will be possible to compare the differences in tactile signals between sticky and non-sticky contact. Such signals could be useful for virtually recreating sticky sensations that make the person feel as if they had touched a sticky object.

Due to the computational complexity of simulating a finger pressing, we were unable to build a three-dimensional finger model for the research in Chapter 4. In addition, we could not include fingerprints on the model for the same reason. This limitation forced us to ignore the real contact area and focus only on the gross contact area, somewhat degrading the quality of the measurement. Since a fingertip model that includes fingerprints is essential, developing a method for fast simulations with a complex model will advance research in finger contact mechanics.

Developing a fingerprint model for simulation will also be helpful in validating a finger's micro stick-slips. Simulating a finger sliding is significantly more complex than simulating a finger pressing due to the dynamically changing morphology of the fingerprint surface. Therefore, a method that simplifies the expression of fingerprint sliding will attract attention.

Lastly, there are numerous ways to improve the transparent moisture sensor. Due to the relatively simple design of the electrodes, the measured impedance comprises information that is difficult to evaluate and interpret independently. For example, both the angle (α) and the length of the impedance trajectory changed similarly. Similarly, the effects of fingerprint ridge width and fingerprint shape across individuals must be characterized. Currently, we have produced three additional moisture sensors based on the improved design. We must re-characterize the sensor using the same methods and conduct additional analysis to determine how moisture and finger pressure affect the improved sensor's impedance.

Appendix A

Correlation heatmaps within participants

We present the Spearman's correlation coefficients between the sixteen physical variable values and the stickiness ratings across trials for each participant. Including self-correlations and the correlations between the physical variables, a total of 136 correlation coefficients (ρ) and corresponding probability values (p) were obtained per participant. Every participant's figure shows a heatmap with cells that are labeled and colored by the correlation coefficients; the lower number in each cell is the associated p-value.

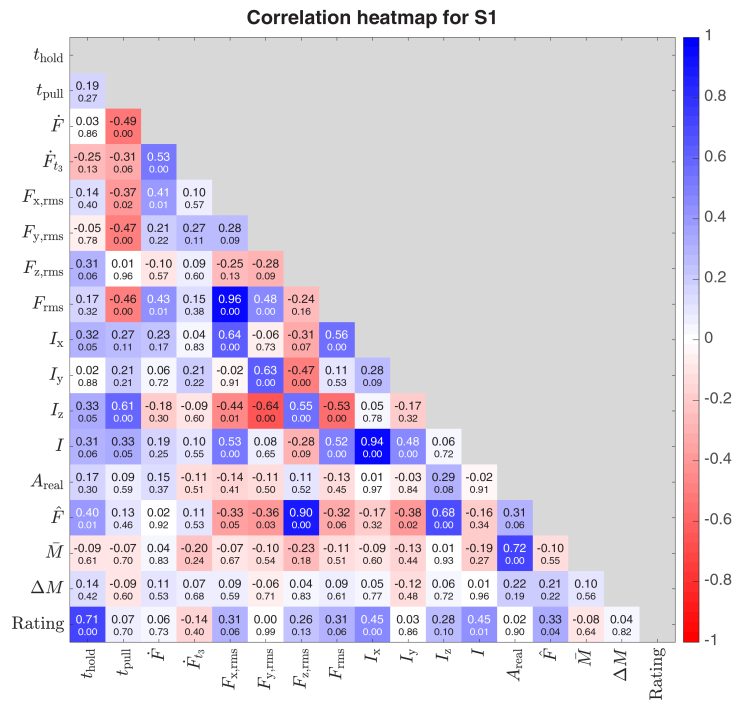


Figure A.1: Correlation heatmap for S1.

Appendix A Correlation heatmaps within participants

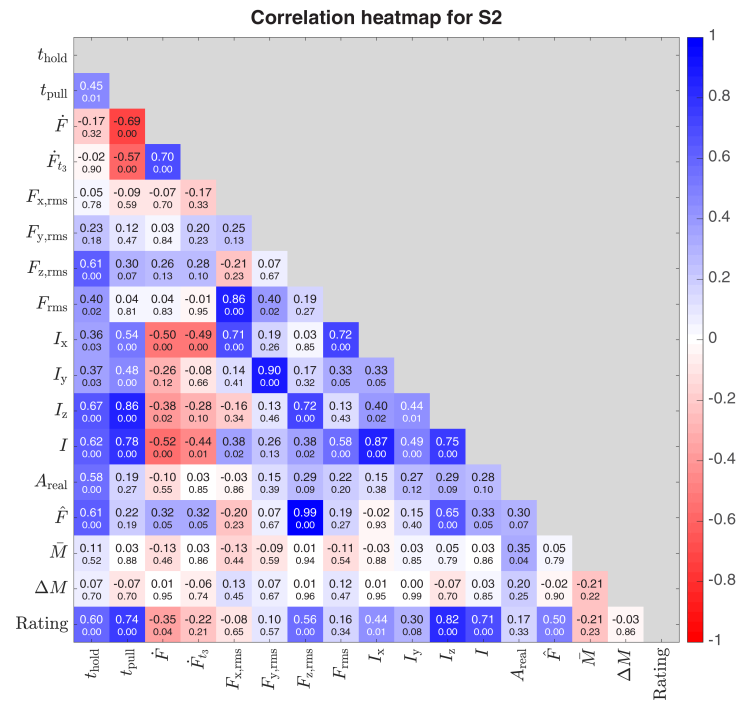


Figure A.2: Correlation heatmap for S2.

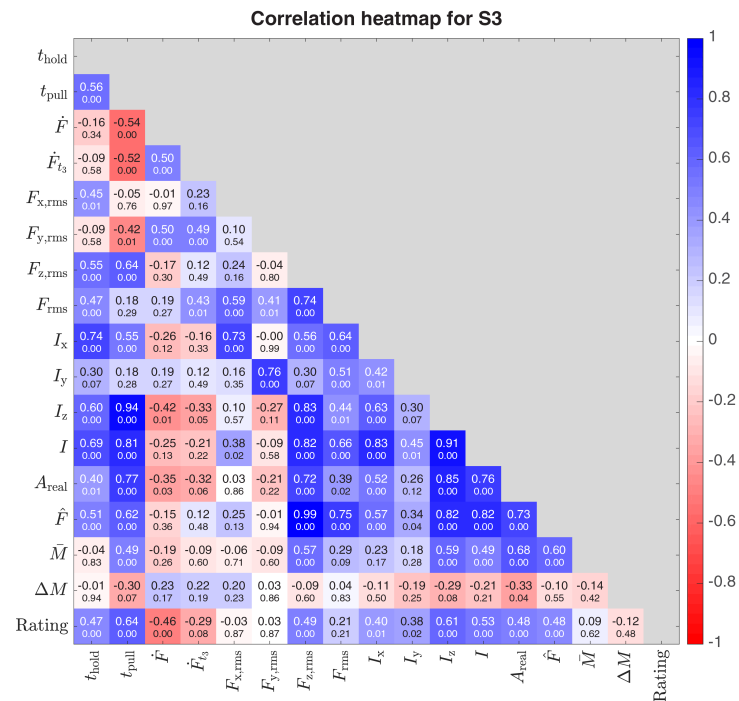


Figure A.3: Correlation heatmap for S3.

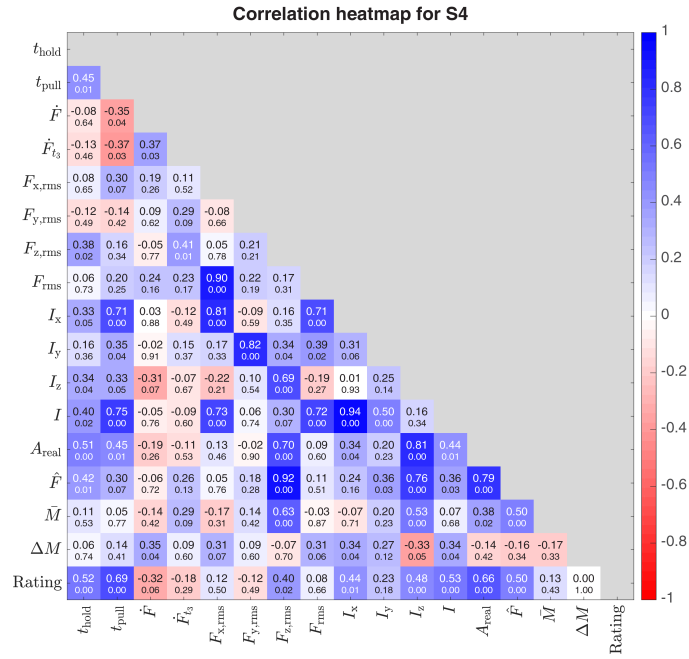


Figure A.4: Correlation heatmap for S4.

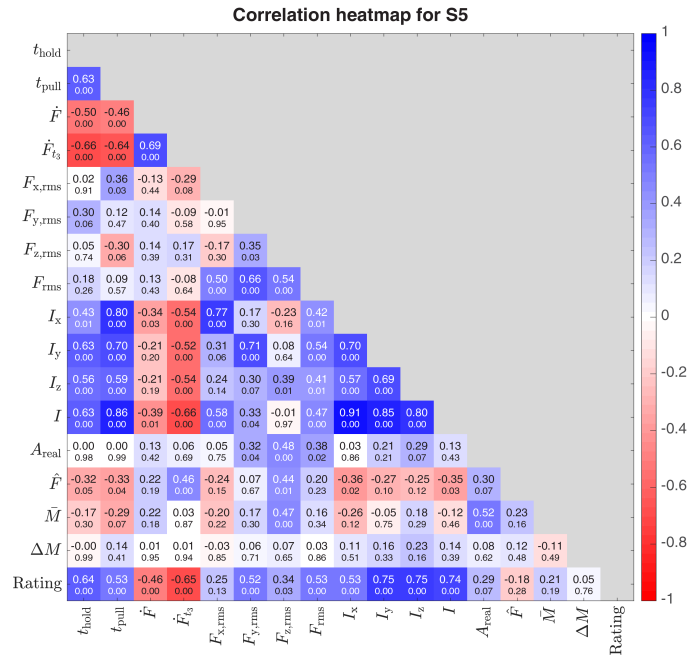


Figure A.5: Correlation heatmap for S5

Appendix A Correlation heatmaps within participants

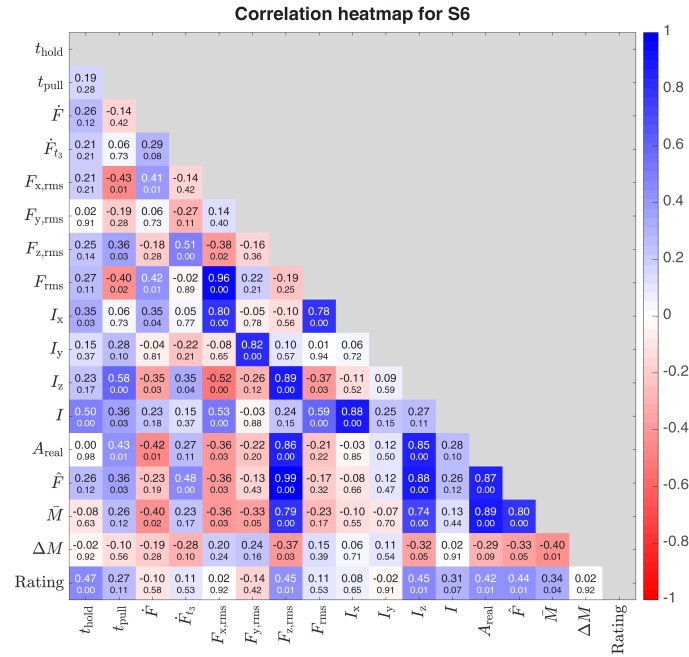


Figure A.6: Correlation heatmap for S6

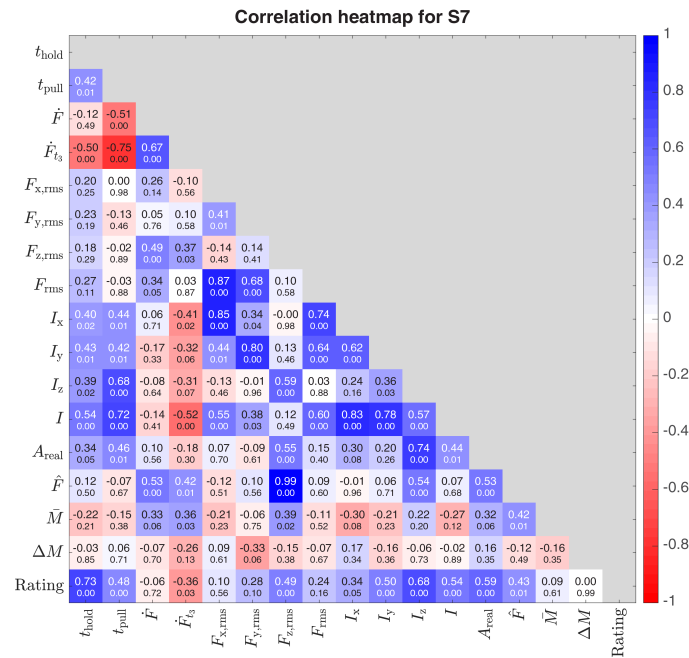


Figure A.7: Correlation heatmap for S7

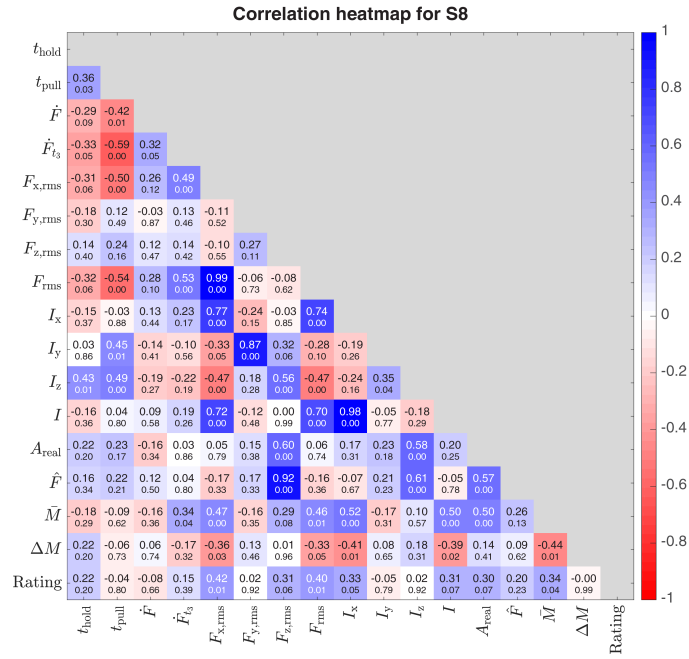


Figure A.8: Correlation heatmap for S8

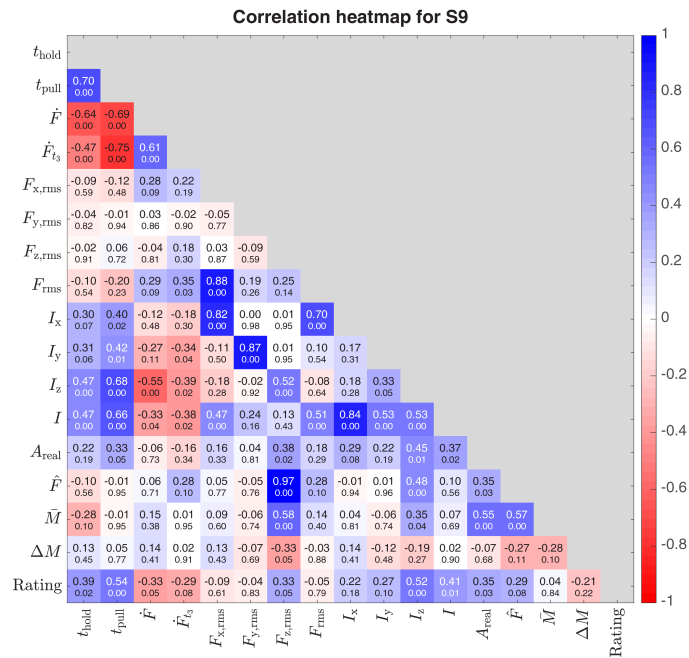


Figure A.9: Correlation heatmap for S9

Appendix B

Statistical analysis by the skin moisture group

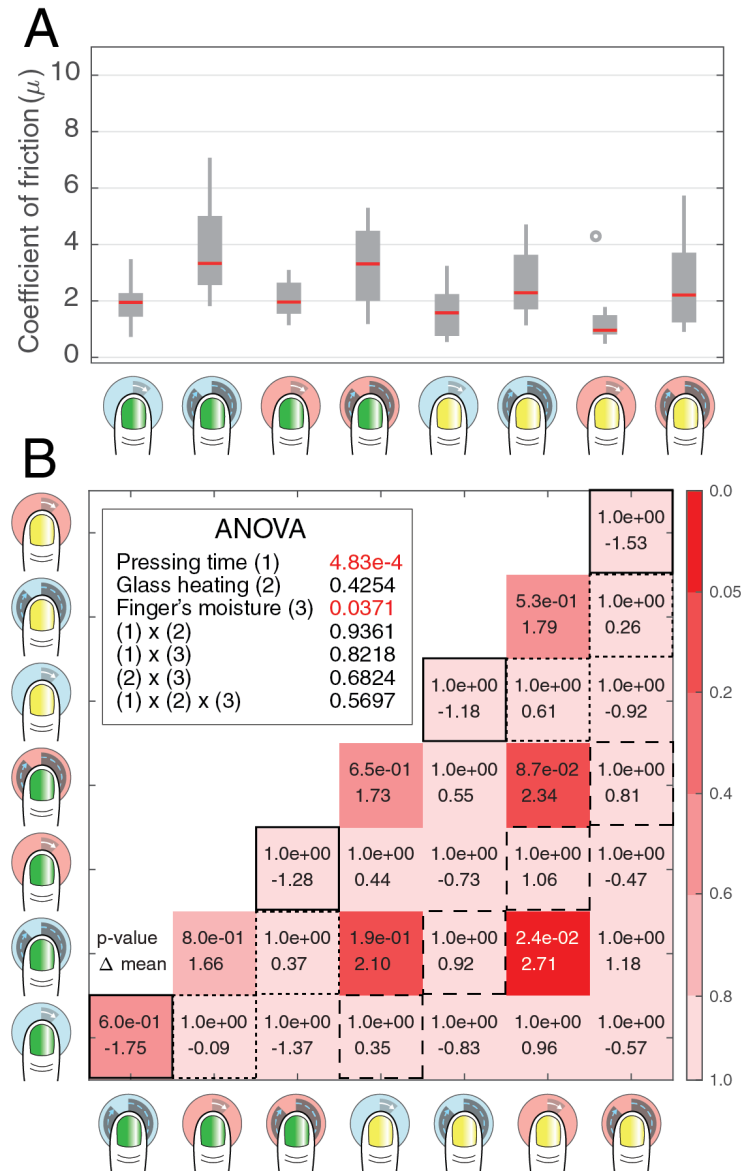


Figure B.1: The coefficient of friction measured from the **dry skin group** and the associated statistical analyses. (A) The box plots of measured friction data by the contact conditions. (B) The p-values from the three-way ANOVA test (inset) and the posthoc tests, where the top values in the confusion matrix indicate p-values from Student's t-distribution after applying Bonferroni correction, and the bottom values are the difference between the mean friction coefficient in the y-axis condition and the mean friction coefficient in the x-axis condition. The pictograms for the contact conditions are explained in Fig. 5.3(A). Note that the black boxes with solid lines represent a comparison where only the pressing time differs, the black boxes with dotted lines represent a comparison where only the plate heating differs, and the black boxes with dashed lines represent a comparison where only the finger's moisture differs.

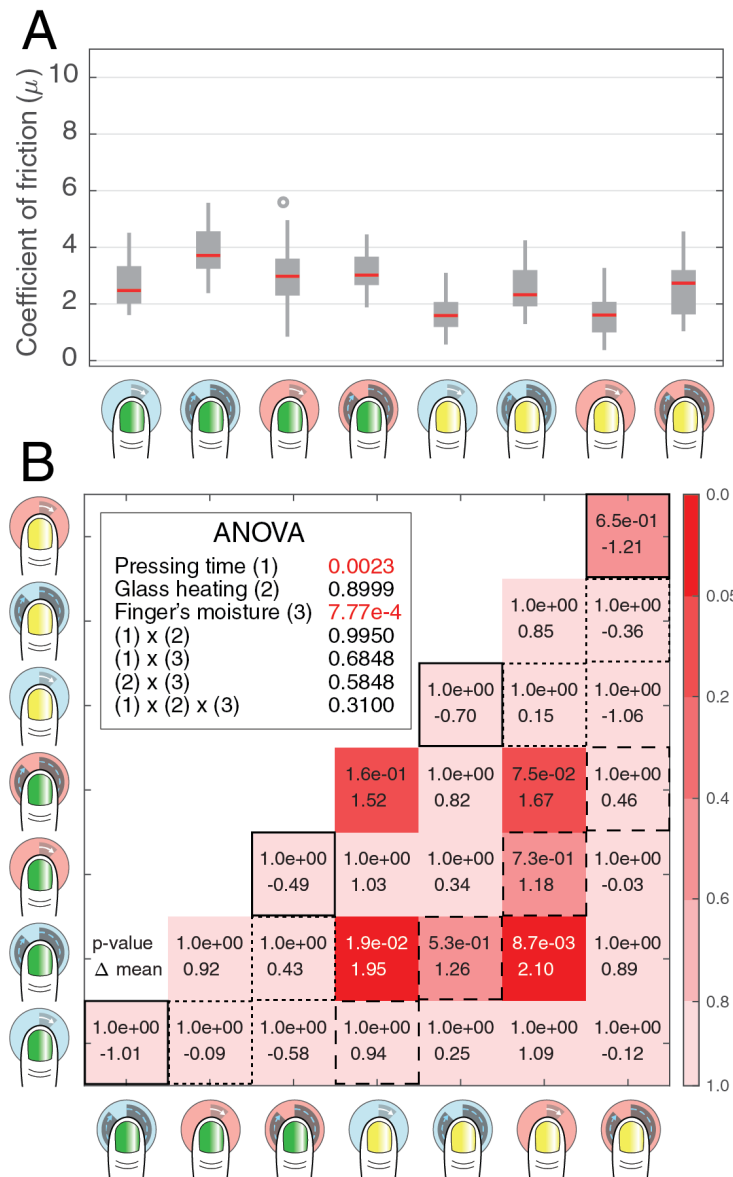


Figure B.2: The coefficient of friction measured from the **typical skin group** and the associated statistical analyses. (A) The box plots of measured friction data by the contact conditions. (B) The p-values from the three-way ANOVA test (inset) and the posthoc tests, where the top values in the confusion matrix indicate p-values from Student's t-distribution after applying Bonferroni correction, and the bottom values are the difference between the mean friction coefficient in the y-axis condition and the mean friction coefficient in the x-axis condition. The pictograms for the contact conditions are explained in Fig. 5.3(A). Note that the black boxes with solid lines represent a comparison where only the pressing time differs, the black boxes with dotted lines represent a comparison where only the plate heating differs, and the black boxes with dashed lines represent a comparison where only the finger's moisture differs.

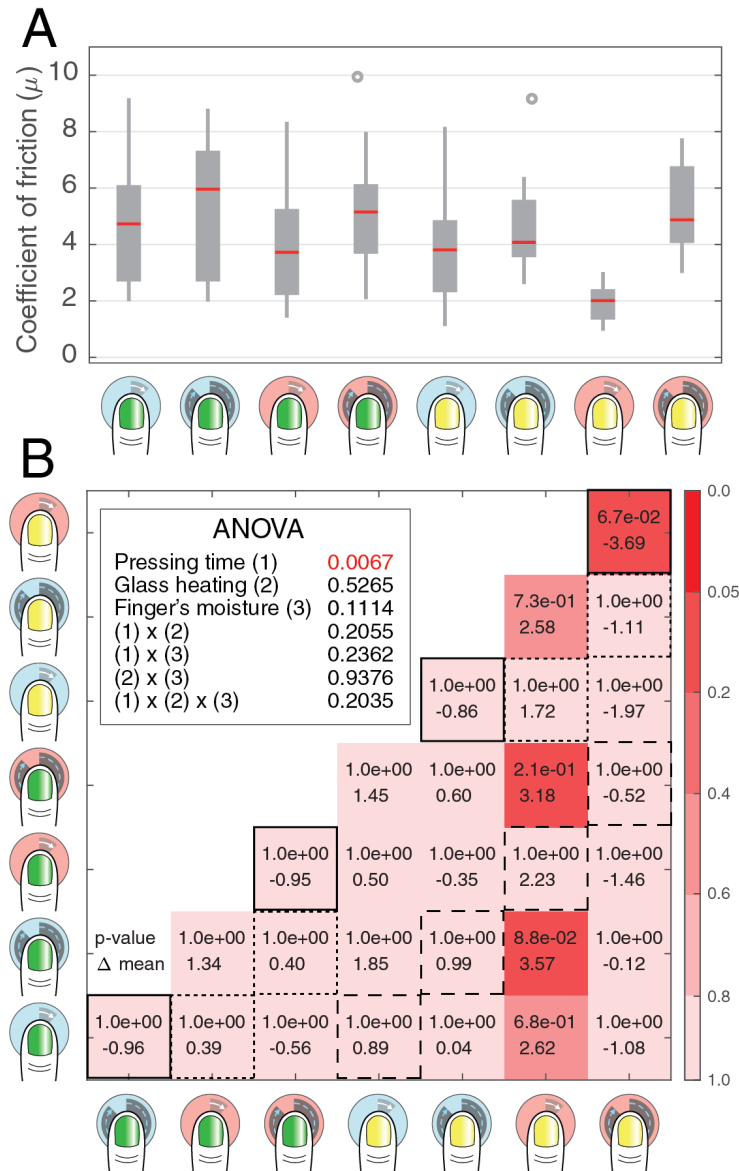


Figure B.3: The coefficient of friction measured from the **moist skin group** and the associated statistical analyses. (A) The box plots of measured friction data by the contact conditions. (B) The p-values from the three-way ANOVA test (inset) and the posthoc tests, where the top values in the confusion matrix indicate p-values from Student's t-distribution after applying Bonferroni correction, and the bottom values are the difference between the mean friction coefficient in the y-axis condition and the mean friction coefficient in the x-axis condition. The pictograms for the contact conditions are explained in Fig. 5.3(A). Note that the black boxes with solid lines represent a comparison where only the pressing time differs, the black boxes with dotted lines represent a comparison where only the plate heating differs, and the black boxes with dashed lines represent a comparison where only the finger's moisture differs.

Symbols

A	Measured area
\hat{A}	Simulated area
A_{real}	The maximum real contact area before detachment
A_c	Contact area
$A_{c_{\text{end}}}$	The real contact area at the ending time of the finger's pressing
$A_{c_{\text{start}}}$	The real contact area at the starting time of the finger's pressing
α	The angle between the line created by impedance at high frequencies and the y-axis
$^{\circ}\text{C}$	Celsius degree
Δ	Difference
E_0	Serial Young's modulus for the bulk tissue
E_1	Young's modulus parallel to the relaxation time for the bulk tissue
E_2	Young's modulus for epidermis
ε	Strain
η_1	Viscosity
€	Euro
f	Focal length
\dot{F}	Detachment rate
\dot{F}_{t_3}	Detachment rate at t_3
\hat{F}	Peak pull-off force
F_N	Applied normal force
F_{rms}	RMS of force during the pull-off
F_x	Force in x-axis
$F_{x,\text{rms}}$	Root mean square of force in the x-direction during the pull-off
F_y	Force in y-axis
$F_{y,\text{rms}}$	RMS of force in the y-direction during the pull-off
F_z	Force in z-axis
$F_{z,\text{rms}}$	RMS of force in the z-direction during the pull-off
G_1	Shear modulus
I	Total impulse during the pull-off
I_x	Impulse in the x-direction during the pull-off
I_y	Impulse in the y-direction during the pull-off
I_z	Impulse in the z-direction during the pull-off
J	Sums of MSE

Symbols

k	Kilo (10^3)
M	Mega (10^6)
\bar{M}	Mean moisture value
ΔM	Change in moisture after finger detachment
μ	Micro (10^{-6})
n	Constant phase
n	Nano (10^{-9})
ν_1	Poisson's ratio
ω	Angular frequency
p	Percentage value
$\%$	Percentage
π	The ratio of a circle's circumference to its diameter
Q	Constant phase element
r	Radius
R_{ct}	Charge transfer resistance
ρ	Spearman's correlation of a pair
$\bar{\rho}$	Mean participant-specific correlation coefficients
ρ_g	Gradual stuck ratio
ρ_i	Instant stuck ratio
R_s	Electrolyte resistance
σ	Stress
σ_d	Deviatoric stress
SiO_2	Silicon dioxide
t_0	The time the finger starts to contact the plate
t_1	The time the normal force reaches 1.5 N
t_2	The time the pressing finger starts to detach by reducing its normal force
t_3	The time when the force is closest to 0 N
t_4	The first time when the finger is completely detached
τ_1	Relaxation time
t_{hold}	The finger holding duration while the pressing force is kept around 1.5 N
t_{pull}	Detaching duration of the finger after force changes sign

Abbreviations

3D	Three-dimensional
ANOVA	Analysis of variance
COVID	Coronavirus disease
CPE	Constant phase element
DC	Direct current
DMT	Derjaguin-Muller-Toporov
DoF	Degree of freedom
EIS	Electrochemical impedance spectroscopy
FA	Fast adapting
FE	Finite element
fMRI	Functional magnetic resonance imaging
FTIR	Frustrated total internal reflection
h	Hour(s)
HI	Haptic Intelligence
IDE	Inter-digital electrode
IMPRS-IS	International Max Planck Research School for Intelligent Systems
ITO	Indium tin oxide
JKR	Johnson-Kendall-Roberts
LED	Light-emitting diode
LF	Lateral force
MPI-IS	Max Planck Institute for Intelligent Systems
MSE	Mean squared error
NF	Normal force
NI	National Instruments
ODE	Ordinary differential equation
PC	Personal computer
PCB	Printed circuit board
PCI	Peripheral component interconnect
PDMS	Polydimethylsiloxane
Ph.D.	Doctor of Philosophy
PR	Photo-resist
PSO	Particle swarm optimization
RC	Resistance and capacitance
RMS	Root mean square

Abbreviations

rpm	Rotations per minute
s	Second(s)
SD	Standard deviation
SLS	Standard linear solid
VR	Virtual reality

List of Tables

- 4.1 Constant parameter values for the FE finger model. 35
- 6.1 Optimal circuit parameters determined by fitting the circuit to impedance measurements, RMSE between the observed and calculated impedance, and the real part of the impedance observed at 1 MHz. 66

List of Figures

2.1	A soft finger's contact area develops in various ways depending on its material properties and how it is pressed into the surface (Photo by Nam and Kuchenbecker / CC BY).	7
3.1	Apparatus for measuring the moisture content, contact force vector, and real contact area of a finger actively pressing on a glass plate. Note that three small rectangular regions were pixelated in the fingerprint image before publication to conceal the identity of this participant (Illustration by Nam, Vardar, Gueorguiev, and Kuchenbecker / CC BY).	12
3.2	The chronological procedure of one trial of the experiment. After (a) three measurements of the fingerpad's moisture, (b) the participant places his or her finger on a clean glass plate and reaches a normal force of 1.5 N. After a preprogrammed pressing duration (0, 1.5, or 3 s), a visual cue appears on the screen prompting the participant to detach the finger. (c) The participant detaches his or her finger and judges the stickiness of the glass using a nine-point scale. (d) The participant's fingerpad moisture level is measured three more times (Illustration by Nam, Vardar, Gueorguiev, and Kuchenbecker / CC BY).	14
3.3	(a) Procedure for calculating the real finger contact area from a raw image. The camera calibration step corrects the lens distortion. Next, image transformation rectifies the slanted finger image. Two different threshold methods applied in parallel appropriately distinguish the finger contact area from the non-contact area without being confused by (b) condensed moisture around the finger. In such cases, taking (c) the global threshold identifies condensation as part of the contact finger area, but applying a local adaptive threshold removes the condensation area to produce (d) the final image. Note that three small rectangular regions were pixelated in each fingerprint image before publication to conceal the identity of this participant (Illustration by Nam, Vardar, Gueorguiev, and Kuchenbecker / CC BY).	15
3.4	(a) The measured force in the z-direction and (b) the real contact area as a function of time from a sample trial, including parameter definitions (Illustration by Nam, Vardar, Gueorguiev, and Kuchenbecker / CC BY).	17

3.5	Boxplots of the sixteen physical variables calculated for each participant (S1 to S9), ordered by ascending median value with all subjects combined at the end. The data are color-coded by participant. In each distribution, the black line shows the median, the box shows the second and third quartiles, the whiskers show the range up to 1.5 times the interquartile range, and the + symbol indicates outliers. The plotted variables are (a) t_{hold} , (b) t_{pull} , (c) \hat{F} , (d) \hat{F}_{t_3} , (e) $F_{x,\text{rms}}$, (f) $F_{y,\text{rms}}$, (g) $F_{z,\text{rms}}$, (h) F_{rms} , (i) I_x , (j) I_y , (k) I_z , (l) I , (m) A_{real} , (n) \hat{F} , (o) \bar{M} , and (p) ΔM (Illustration by Nam, Vardar, Gueorguiev, and Kuchenbecker / CC BY).	22
3.6	Distributions of stickiness ratings across participants. (a) The numbers in the heatmap represent the percentage of trials that received each rating. (b) The entire distribution of ratings per participant is shown as a boxplot (Illustration by Nam, Vardar, Gueorguiev, and Kuchenbecker / CC BY).	23
3.7	A heatmap showing the mean participant-specific correlation coefficients ($\bar{\rho}$) among the physical variables and the stickiness ratings. The second line of text in each cell lists the proportion of subjects whose correlations showed high significance ($p < 0.05$). The bar chart located below the heatmap shows the means and standard deviations of ρ across participants, plus the p-values of the four paired t-tests reported in the text (Illustration by Nam, Vardar, Gueorguiev, and Kuchenbecker / CC BY).	24
3.8	Correlations between the physical variables across participants based on the median variable value for each participant. A high value means that the nine participants are ranked in approximately the same order in the two corresponding subplots of Fig. 3.5. A dot appears under the coefficient when the correlation is significant ($p < 0.05$) (Illustration by Nam, Vardar, Gueorguiev, and Kuchenbecker / CC BY).	26
3.9	Sensory relevance between I_z and I_x by comparing correlations between stickiness and the impulse that participants felt. (a) A clear sensory relevance is shown by a high correlation between the directional correlation between stickiness and the z-impulse and the median z-impulse value experienced by participants. (b) There is no trend in the same correlation for the x-direction. (c) The correlation between stickiness and the x-impulse also does not correlate with the median x-impulse (Illustration by Nam, Vardar, Gueorguiev, and Kuchenbecker / CC BY).	27
4.1	(a) Our apparatus for capturing normal forces and contact images over time while a finger is pressing the glass plate (Nam <i>et al.</i> , 2020). The nearby moisture sensor measures the fingerpad’s moisture level before and after contact. (b) The processing steps used to extract gross contact area from each raw contact image. Three regions of each fingerprint have been pixelized to prevent personal identification of the participant (Illustration by Nam and Kuchenbecker / CC BY).	32

4.2	(a) Our axially symmetric 3D finger model with lumped parameters and the conditions used for the simulations. (b) One recording of gross contact area over time for a natural finger pressing (the red line) compared with a simulation of the finger model pressing (the cyan line). Here, the model was simulated with the parameters of $(E_0, E_1, \tau_1, E_2) = (140 \text{ kPa}, 20 \text{ kPa}, 0.5 \text{ s}, 2200 \text{ kPa})$; the inset image shows its deformation and von Mises stress at a time of 0.654 s (Illustration by Nam and Kuchenbecker / CC BY).	34
4.3	Measured data after the post-processing. (a) The moisture values from the 45 trials are clearly distributed into three groups. (b) The way the gross contact area increases as a function of pressing force differs somewhat across moisture conditions; the fitted equation is based on the theoretical relationship between contact area and normal force for an elastic sphere. (c) Within each condition, the subject sometimes pressed quickly and sometimes much more slowly (Illustration by Nam and Kuchenbecker / CC BY).	38
4.4	Top candidates for the lumped parameter values found by the particle swarm optimization algorithm, as well as the resulting MSE sums. The dashed lines indicate the boundaries where the sum of the MSE increases substantially compared to the fitting error of the top candidates (Illustration by Nam and Kuchenbecker / CC BY).	39
4.5	One selected trial from each experimental condition. (a) The subject increased his pressing force in a very similar way for all three trials. (b) The resulting contact area over time differs across conditions (Illustration by Nam and Kuchenbecker / CC BY).	40
5.1	A custom-built apparatus to capture the contact images and force vectors during the finger-surface interaction. The inset illustrates the working principle for how this apparatus captures contact area.	44

5.2	Key processed data from measurements of a finger sliding laterally. (A) The change of the real contact area and forces over time, (B) the flow of friction and two types of stuck ratios (ρ_g for gradual stuck ratio and ρ_i for instant stuck ratio), focused at the time of the finger's sliding (the area shaded in pink in the bottom plot of (A)), (C) the captured images and processed contact area images showing the finger's shift across frames, and (D) displacement fields in the five contiguous frames that are shaded in blue-gray in the bottom plot of (B). The fingerprint image on the left side of (C) is composed of three intensity images captured at frames marked with red, green, and blue vertical lines in the bottom plot of (B). In accordance with the color scheme, the first, second, and third images are color-coded in red, green, and blue, respectively. The same method is used to compose the binary fingerprint image in (C) (see the illustration in the bottom right). Note that the color configuration seems opposite between the two images because the contact area's color intensity is inverted. To protect the identity of the participant, three sections were pixelated in the fingerprint images.	46
5.3	Measured coefficient of friction and the associated statistical analyses. (A) Symbols indicating the two conditions for each of three variables. (B) The box plots of measured friction data by the contact conditions. (C) The p-values from the three-way ANOVA test (inset) and the posthoc tests, where the top values in the confusion matrix indicate p-values from Student's t-distribution after applying Bonferroni correction, and the bottom values are the difference between the mean friction coefficient in the y-axis condition and the mean friction coefficient in the x-axis condition.	51
5.4	(A) Changes in the coefficient of friction caused by heating the glass plate within each skin group are shown as a symbol and a value in parenthesis; the pictograms for the contact conditions are explained in Fig. 5.3(A). (B) Working principle of moisture condensation. (C) Images captured when sliding a highly moist natural finger on the non-heated surface (left) and the heated surface (right).	52
5.5	(A) The mean moisture values measured by the Corneometer immediately before (left boxplot in each pair) and after (right boxplot in each pair) finger-contact with the glass plate, plotted for all eight conditions. (B) The real contact area is separately shown at the starting time of the finger's pressing (left boxplot in each pair; $A_{C_{start}}$ in Fig. 5.2) and at the end time (right boxplot in each pair; $A_{C_{end}}$ in Fig. 5.2).	54

5.6	(A) The mean moisture values measured by Corneometer, representing the pre (preceding boxplot) and post finger-contact to the glass plate (following boxplot), plotted for the dry finger's three skin groups when pressing for 10 s on non-heated and heated plates. (B) The real contact area separately shown at the starting time of the finger's pressing (preceding boxplot; $A_{c_{start}}$ in Fig. 5.2) and at the end time (following boxplot; $A_{c_{end}}$ in Fig. 5.2).	55
6.1	The entire characterization system for the moisture sensor. The developed moisture sensor is attached to the previously built apparatus that captures the contact images and force vectors during the finger's pressing. When a finger touches the sensor, as shown in the inset, the wire-connected impedance analyzer measures impedance across a wide frequency range.	58
6.2	(a) The sensing principle based on fringing electric fields formed between electrodes and (b) a simulation of the field distribution in COMSOL Multiphysics.	59
6.3	(a) An illustration of the sensing area, (b) a microscopic image of the fabricated electrodes, and (c) a top view of the whole fabricated electrodes, where the relative brightness of the two terminals indicates the absence of a cover layer.	60
6.4	Our sensor's fabrication processes and photographs. (a) – (f) Direct laser lithography allows us to produce micropatterned electrodes. (g) The developed photo-resist layer can be observed using an optical microscope. (h) Erosion on the wall of the lift-off photo-resist (PR) allows indium tin oxide (ITO) to be disconnected, resulting in (i) clean edges of the ITO pattern after the lift-off procedure. As a result, (j) a highly transparent layer of ITO has been deposited. (k) The sensor sample is adhered to a custom ring-shaped printed circuit board (PCB), and (l) both terminals of the electrodes were then coated with gold/chromium and connected to the PCB through multiple electrical wires.	61
6.5	Impedance measurements are shown in the complex plane, with the equivalent circuit and optimal component values. (a) The left figure presents the results when the impedance analyzer measures the sensor, and (b) the middle figure shows the results when a natural finger presses the sensor with 1.0 N. The used frequency range was between 1 Hz and 1 MHz. (c,d) The representation of a typical impedance graph for the circuit model depicted in (a) and (b) is shown in (c) and (d), respectively. .	64
6.6	Impedance measurements across a range of frequencies (1 kHz – 1 MHz), plotted by finger moisture and pressing force.	65

6.7	(a) Weak adhesion between the ITO layer and the glass substrate causes delamination to spread over time. (b) To prevent this problem, we coated the substrate with SiO ₂ , conducted annealing, and thickened the insulating cover layer. (c) A tape removal test revealed that the adhesion between the ITO layer and the substrate had improved. (d) The removal of residual stress from layers was enhanced by annealing.	68
A.1	Correlation heatmap for S1.	75
A.2	Correlation heatmap for S2.	76
A.3	Correlation heatmap for S3.	76
A.4	Correlation heatmap for S4.	77
A.5	Correlation heatmap for S5	77
A.6	Correlation heatmap for S6	78
A.7	Correlation heatmap for S7	78
A.8	Correlation heatmap for S8	79
A.9	Correlation heatmap for S9	79
B.1	The coefficient of friction measured from the dry skin group and the associated statistical analyses. (A) The box plots of measured friction data by the contact conditions. (B) The p-values from the three-way ANOVA test (inset) and the posthoc tests, where the top values in the confusion matrix indicate p-values from Student's t-distribution after applying Bonferroni correction, and the bottom values are the difference between the mean friction coefficient in the y-axis condition and the mean friction coefficient in the x-axis condition. The pictograms for the contact conditions are explained in Fig. 5.3(A). Note that the black boxes with solid lines represent a comparison where only the pressing time differs, the black boxes with dotted lines represent a comparison where only the plate heating differs, and the black boxes with dashed lines represent a comparison where only the finger's moisture differs.	82

- B.2 The coefficient of friction measured from the **typical skin group** and the associated statistical analyses. (A) The box plots of measured friction data by the contact conditions. (B) The p-values from the three-way ANOVA test (inset) and the posthoc tests, where the top values in the confusion matrix indicate p-values from Student's t-distribution after applying Bonferroni correction, and the bottom values are the difference between the mean friction coefficient in the y-axis condition and the mean friction coefficient in the x-axis condition. The pictograms for the contact conditions are explained in Fig. 5.3(A). Note that the black boxes with solid lines represent a comparison where only the pressing time differs, the black boxes with dotted lines represent a comparison where only the plate heating differs, and the black boxes with dashed lines represent a comparison where only the finger's moisture differs. . . 83
- B.3 The coefficient of friction measured from the **moist skin group** and the associated statistical analyses. (A) The box plots of measured friction data by the contact conditions. (B) The p-values from the three-way ANOVA test (inset) and the posthoc tests, where the top values in the confusion matrix indicate p-values from Student's t-distribution after applying Bonferroni correction, and the bottom values are the difference between the mean friction coefficient in the y-axis condition and the mean friction coefficient in the x-axis condition. The pictograms for the contact conditions are explained in Fig. 5.3(A). Note that the black boxes with solid lines represent a comparison where only the pressing time differs, the black boxes with dotted lines represent a comparison where only the plate heating differs, and the black boxes with dashed lines represent a comparison where only the finger's moisture differs. . . 84

Bibliography

- Abbas, Y., Nutma, J. S., Olthuis, W., and van den Berg, A. (2016). Corrosion monitoring of reinforcement steel using galvanostatically induced potential transients. *IEEE Sensors Journal*, **16**(3), 693–698.
- Adams, M. J., Briscoe, B. J., and Johnson, S. A. (2007). Friction and lubrication of human skin. *Tribology Letters*, **26**(3), 239–253.
- Adams, M. J., Johnson, S. A., Lefèvre, P., Lévesque, V., Hayward, V., André, T., and Thonnard, J.-L. (2013). Finger pad friction and its role in grip and touch. *Journal of The Royal Society Interface*, **10**(80), 20120467.
- André, T., Lefèvre, P., and Thonnard, J.-L. (2008). Measurement and influence of the skin moisture in dexterous manipulation. In M. Ferre, editor, *Haptics: Perception, Devices and Scenarios*, pages 373–377, Berlin, Heidelberg. Springer Berlin Heidelberg.
- André, T., Lefèvre, P., and Thonnard, J.-L. (2009). A continuous measure of fingertip friction during precision grip. *Journal of Neuroscience Methods*, **179**(2), 224–229.
- André, T., Lefèvre, P., and Thonnard, J.-L. (2010). Fingertip moisture is optimally modulated during object manipulation. *Journal of Neurophysiology*, **103**(1), 402–408. PMID: 19906876.
- André, T., Lévesque, V., Hayward, V., Lefèvre, P., and Thonnard, J.-L. (2011). Effect of skin hydration on the dynamics of fingertip gripping contact. *Journal of The Royal Society Interface*, **8**(64), 1574–1583.
- Ayyildiz, M., Scaraggi, M., Sirin, O., Basdogan, C., and Persson, B. N. J. (2018). Contact mechanics between the human finger and a touchscreen under electroadhesion. *Proceedings of the National Academy of Sciences*, **115**(50), 12668–12673.
- Barquins, M. and Maugis, D. (1981). Tackiness of elastomers. *The Journal of Adhesion*, **13**(1), 53–65.
- Barquins, M., Maugis, D., Blouet, J., and Courtel, R. (1978). Contact area of a ball rolling on an adhesive viscoelastic material. *Wear*, **51**(2), 375–384.
- Barsoukov, E. and Macdonald, J. R. (2005). Impedance spectroscopy theory, experiment, and. *Applications, 2nd ed.*(Hoboken, NJ: John Wiley & Sons, Inc., 2005).

- Barthel, E. (2008). Adhesive elastic contacts: JKR and more. *Journal of Physics D: Applied Physics*, **41**(16), 163001.
- Ben Messaoud, W., Bueno, M.-A., and Lemaire-Semail, B. (2016). Relation between human perceived friction and finger friction characteristics. *Tribology International*, **98**, 261–269.
- Bensmaïa, S. and Hollins, M. (2005). Pacinian representations of fine surface texture. *Perception & Psychophysics*, **67**(5), 842–854.
- Bergmann Tiest, W. M. (2010). Tactual perception of material properties. *Vision Research*, **50**(24), 2775–2782.
- Blackstone, J. M. and Johnson, P. W. (2007). Children and gender-differences in exposure and how anthropometric differences can be incorporated into the design of computer input devices. *Scandinavian Journal of Work, Environment & Health*, (3), 26–32.
- Bochereau, S., Dzidek, B., Adams, M., and Hayward, V. (2017). Characterizing and imaging gross and real finger contacts under dynamic loading. *IEEE Transactions on Haptics*, **10**(4), 456–465.
- Cadoret, G. and Smith, A. M. (1996). Friction, not texture, dictates grip forces used during object manipulation. *Journal of Neurophysiology*, **75**(5), 1963–1969. PMID: 8734595.
- Caldwell, D. G., Tsagarakis, N., and Giesler, C. (1999). An integrated tactile/shear feedback array for stimulation of finger mechanoreceptor. In *Proceedings of IEEE International Conference on Robotics and Automation*, volume 1, pages 287–292.
- Cârlescu, V., Olaru, D. N., Prisăcaru, G., Opreșan, C., Știrbu, R. t., and Machado, J. (2019). Influence of the indentation speed on viscoelastic behavior of the human finger. In J. Machado, F. Soares, and G. Veiga, editors, *Innovation, Engineering and Entrepreneurship*, pages 143–150. Springer International Publishing.
- Carver, E. (2016). Fingers, hand and wrist.
- Chalmers, T. M. and Keele, C. A. (1952). The nervous and chemical control of sweating. *British Journal of Dermatology*, **64**(2), 43–54.
- Choi, C., Ma, Y., Li, X., Chatterjee, S., Sequeira, S., Friesen, R. F., Felts, J. R., and Hipwell, M. C. (2022). Surface haptic rendering of virtual shapes through change in surface temperature. *Science Robotics*, **7**(63), eabl4543.

- Comaish, S. and Bottoms, E. (1971). The skin and friction: Deviations from amonton's laws, and the effects of hydration and lubrication. *British Journal of Dermatology*, **84**(1), 37–43.
- COMSOL Inc. (2022). Generalized Kelvin viscoelastic material.
- Constantin, M.-M., Poenaru, E., Poenaru, C., and Constantin, T. (2014). Skin hydration assessment through modern non-invasive bioengineering technologies. *Maedica*, **9**(1), 33–38.
- Cornuault, P.-H., Carpentier, L., Bueno, M.-A., Cote, J.-M., and Monteil, G. (2015). Influence of physico-chemical, mechanical and morphological fingerpad properties on the frictional distinction of sticky/slippery surfaces. *Journal of The Royal Society Interface*, **12**(110), 20150495.
- Dandekar, K., Raju, B. I., and Srinivasan, M. A. (2003). 3-d finite-element models of human and monkey fingertips to investigate the mechanics of tactile sense. *Journal of biomechanical engineering*, **125**(5), 682–691.
- Davies, E. R. (2012). *Computer and Machine Vision: Theory, Algorithms, Practicalities*. Academic Press.
- Delhaye, B., Lefèvre, P., and Thonnard, J.-L. (2014). Dynamics of fingertip contact during the onset of tangential slip. *Journal of The Royal Society Interface*, **11**(100), 20140698.
- Delhaye, B., Barrea, A., Edin, B. B., Lefèvre, P., and Thonnard, J.-L. (2016). Surface strain measurements of fingertip skin under shearing. *Journal of The Royal Society Interface*, **13**(115), 20150874.
- Delhaye, B. P., Jarocka, E., Barrea, A., Thonnard, J.-L., Edin, B., and Lefèvre, P. (2021a). High-resolution imaging of skin deformation shows that afferents from human fingertips signal slip onset. *eLife*, **10**, e64679.
- Delhaye, B. P., Schiltz, F., Barrea, A., Thonnard, J.-L., and Lefèvre, P. (2021b). Measuring fingerpad deformation during active object manipulation. *Journal of Neurophysiology*, **126**(4), 1455–1464. PMID: 34495789.
- Demartine, M. L. and Cussler, E. L. (1975). Predicting subjective spreadability, viscosity, and stickiness. *Journal of Pharmaceutical Sciences*, **64**(6), 976–982.
- Derler, S. and Gerhardt, L.-C. (2012). Tribology of skin: Review and analysis of experimental results for the friction coefficient of human skin. *Tribology Letters*, **45**(1), 1–27.

- Derler, S., Rossi, R., and Rotaru, G.-M. (2015). Understanding the variation of friction coefficients of human skin as a function of skin hydration and interfacial water films. *Proceedings of the Institution of Mechanical Engineers, Part J: Journal of Engineering Tribology*, **229**(3), 285–293.
- Dey, A. and Basudhar, P. (2010). Applicability of Burger model in predicting the response of viscoelastic soil beds. In *GeoFlorida 2010: Advances in Analysis, Modeling & Design*, pages 2611–2620.
- Dinç, O. S., Ettles, C. M., Calabrese, S. J., and Scarton, H. A. (1991). Some parameters affecting tactile friction. *Journal of Tribology*, **113**(3), 512–517.
- Dinnar, U. (1970). A note on the theory of deformation in compressed skin tissues. *Mathematical Biosciences*, **8**(1), 71–82.
- Dorogin, L., Tiwari, A., Rotella, C., Mangiagalli, P., and Persson, B. N. J. (2017). Role of preload in adhesion of rough surfaces. *Physical Review Letters*, **118**, 238001.
- Dorogin, L., Tiwari, A., Rotella, C., Mangiagalli, P., and Persson, B. N. J. (2018). Adhesion between rubber and glass in dry and lubricated condition. *The Journal of Chemical Physics*, **148**(23), 234702.
- Dzidek, B., Bochereau, S., Johnson, S. A., Hayward, V., and Adams, M. J. (2017a). Why pens have rubbery grips. *Proceedings of the National Academy of Sciences*, **114**(41), 10864–10869.
- Dzidek, B. M., Adams, M. J., Andrews, J. W., Zhang, Z., and Johnson, S. A. (2017b). Contact mechanics of the human finger pad under compressive loads. *Journal of The Royal Society Interface*, **14**(127), 20160935.
- Edin, B. B. (2004). Quantitative analyses of dynamic strain sensitivity in human skin mechanoreceptors. *Journal of Neurophysiology*, **92**(6), 3233–3243. PMID: 15548636.
- Fagiani, R., Massi, F., Chatelet, E., Berthier, Y., and Akay, A. (2011). Tactile perception by friction induced vibrations. *Tribology International*, **44**(10), 1100–1110.
- Fletcher, J. W. A., Williams, S., Whitehouse, M. R., Gill, H. S., and Preatoni, E. (2018). Juvenile bovine bone is an appropriate surrogate for normal and reduced density human bone in biomechanical testing: a validation study. *Scientific reports*, **8**(1), 1–9.
- Fluhr, J. W., Gloor, M., Lazzarini, S., Kleesz, P., Grieshaber, R., and Berardesca, E. (1999). Comparative study of five instruments measuring stratum corneum hydration (corneometer cm 820 and cm 825, skicon 200, nova dpm 9003, dermalab). part i. in vitro. *Skin Research and Technology*, **5**(3), 161–170.

- Fruhstorfer, H., Abel, U., Garthe, C.-D., and Knüttel, A. (2000). Thickness of the stratum corneum of the volar fingertips. *Clinical Anatomy: The Official Journal of the American Association of Clinical Anatomists and the British Association of Clinical Anatomists*, **13**(6), 429–433.
- Fung, Y. C. (2013). *Biomechanics: Mechanical Properties of Living Tissues*. Springer Science & Business Media.
- Gao, W., Emaminejad, S., Nyein, H. Y. Y., Challa, S., Chen, K., Peck, A., Fahad, H. M., Ota, H., Shiraki, H., Kiriya, D., *et al.* (2016). Fully integrated wearable sensor arrays for multiplexed in situ perspiration analysis. *Nature*, **529**(7587), 509–514.
- Gauthier, M. M. (1995). *Engineered Materials Handbook*, volume 1. ASM International.
- Gay, C. (2002). Stickiness – some fundamentals of adhesion. *Integrative and Comparative Biology*, **42**(6), 1123–1126.
- Gay, C. and Leibler, L. (1999). On stickiness. *Physics Today*, **52**, 48–52.
- Gläser, H. J. (1999). *Dünnschichttechnologie auf Flachglas*. Hofmann.
- Goshtasby, A. (1986). Piecewise linear mapping functions for image registration. *Pattern Recognition*, **19**(6), 459–466.
- Gueorguiev, D., Vezzoli, E., Mouraux, A., Lemaire-Semail, B., and Thonnard, J.-L. (2017). The tactile perception of transient changes in friction. *Journal of The Royal Society Interface*, **14**(137), 20170641.
- He, W., Wang, C., Wang, H., Jian, M., Lu, W., Liang, X., Zhang, X., Yang, F., and Zhang, Y. (2019). Integrated textile sensor patch for real-time and multiplex sweat analysis. *Science advances*, **5**(11), eaax0649.
- Huloux, N., Willemet, L., and Wiertlewski, M. (2021). How to measure the area of real contact of skin on glass. *IEEE Transactions on Haptics*, **14**(2), 235–241.
- Jean-Luc Dellis (2021). Zfit.
- Johansson, R. S. and Cole, K. J. (1994). Grasp stability during manipulative actions. *Canadian Journal of Physiology and Pharmacology*, **72**(5), 511–524. PMID: 7954081.
- Johnson, K. L. (1987). *Contact Mechanics*. Cambridge University Press.
- Johnson, K. L. (1999). *Contact Mechanics and Adhesion of Viscoelastic Spheres*, chapter 2, pages 24–41. American Chemical Society.

- Kalia, Y. N. and Guy, R. H. (1995). The electrical characteristics of human skin in vivo. *Pharmaceutical research*, **12**(11), 1605–1613.
- KAYAKU Advanced Materials (2019). Lor/pmgI technical data sheet, rev. b.
- Kennedy, J. and Eberhart, R. (1995). Particle swarm optimization. In *Proceedings of IEEE International Conference on Neural Networks*, volume 4, pages 1942–1948. IEEE.
- Khazaka, G. (2005). Assessment of stratum corneum hydration: Corneometer cm 825. *Bioengineering of the skin: water and stratum corneum*, page 249.
- Kim, J., Yeon, J., Ryu, J., Park, Jang-Yeon and. Chung, S.-C., and Kim, S.-P. (2017). Neural activity patterns in the human brain reflect tactile stickiness perception. *Frontiers in Human Neuroscience*, **11**, 445.
- Levesque, V. and Hayward, V. (2003). Experimental evidence of lateral skin strain during tactile exploration. In *Proceedings of Eurohaptics, Dublin*, pages 261–275.
- Lucas, B. D. and Kanade, T. (1981). An iterative image registration technique with an application to stereo vision. In *Proceedings of the 7th International Joint Conference on Artificial Intelligence - Volume 2, IJCAI'81*, pages 674–679, San Francisco, CA, USA. Morgan Kaufmann Publishers Inc.
- Ludema, K. and Tabor, D. (1966). The friction and visco-elastic properties of polymeric solids. *Wear*, **9**(5), 329–348.
- Macdonald, J. R. (1992). Impedance spectroscopy. *Annals of biomedical engineering*, **20**(3), 289–305.
- Maeno, T., Kobayashi, K., and Yamazaki, N. (1997). Relationship between structure of finger tissue and location of tactile receptors. *Transactions of the Japan Society of Mechanical Engineers, Part C*, **63**(607), 881–888.
- Marques, S. P. C. and Creus, G. J. (2012). *Computational Viscoelasticity*. Springer Science & Business Media.
- MATLAB Camera Calibration Toolbox (2018). version 9.4.0 (R2018a). The MathWorks, Inc., Natick, Massachusetts, United States.
- McAdams, E., Jossinet, J., Subramanian, R., and McCauley, R. (2006). Characterization of gold electrodes in phosphate buffered saline solution by impedance and noise measurements for biological applications. In *2006 International Conference of the IEEE Engineering in Medicine and Biology Society*, pages 4594–4597.

- Mei, B.-A., Lau, J., Lin, T., Tolbert, S. H., Dunn, B. S., and Pilon, L. (2018). Physical interpretations of electrochemical impedance spectroscopy of redox active electrodes for electrical energy storage. *The Journal of Physical Chemistry C*, **122**(43), 24499–24511.
- Mith, S., Carpentier, L., and Monteil, G. (2008). Correlation between the sensorial perception and the descriptive instrumental analysis of the tackiness of silicone elastomers. *Surface and Interface Analysis*, **40**(3–4), 142–145.
- Nam, S. and Kuchenbecker, K. J. (2021). Optimizing a viscoelastic finite element model to represent the dry, natural, and moist human finger pressing on glass. *IEEE Transactions on Haptics*, **14**(2), 303–309.
- Nam, S., Vardar, Y., Gueorguiev, D., and Kuchenbecker, K. J. (2020). Physical variables underlying tactile stickiness during fingerpad detachment. *Frontiers in Neuroscience*, **14**, 235.
- National Geographic (2022). Condensation.
- Nayak, V. C., Rastogi, P., Kanchan, T., Lobo, S. W., Yoganarasimha, K., Nayak, S., Rao, N. G., Pradeep Kumar, G., Suresh Kumar Shetty, B., and Menezes, R. G. (2010). Sex differences from fingerprint ridge density in the indian population. *Journal of Forensic and Legal Medicine*, **17**(2), 84–86.
- O’goshi, K.-i. and Serup, J. (2007). Skin conductance; validation of Skicon-200EX[®] compared to the original model, Skicon-100[®]. *Skin Research and Technology*, **13**(1), 13–18.
- Orazem, M. E. and Tribollet, B. (2017). *Electrochemical Impedance Spectroscopy*. John Wiley & Sons.
- Papetti, S., Järveläinen, H., Giordano, B. L., Schiesser, S., and Fröhlich, M. (2017). Vibrotactile sensitivity in active touch: Effect of pressing force. *IEEE Transactions on Haptics*, **10**(1), 113–122.
- Pastewka, L. and Robbins, M. O. (2014). Contact between rough surfaces and a criterion for macroscopic adhesion. *Proceedings of the National Academy of Sciences*, **111**(9), 3298–3303.
- Pasumarty, S. M., Johnson, S. A., Watson, S. A., and Adams, M. J. (2011). Friction of the human finger pad: Influence of moisture, occlusion and velocity. *Tribology Letters*, **44**(2), 117–137.
- Persson, B. N. J. (2001). Theory of rubber friction and contact mechanics. *The Journal of Chemical Physics*, **115**(8), 3840–3861.

- Persson, B. N. J., Kovalev, A., and Gorb, S. N. (2013). Contact mechanics and friction on dry and wet human skin. *Tribology Letters*, **50**(1), 17–30.
- Randles, J. E. B. (1947). Kinetics of rapid electrode reactions. *Discussions of the faraday society*, **1**, 11–19.
- Rizzolatti, G. and Luppino, G. (2001). The cortical motor system. *Neuron*, **31**(6), 889–901.
- Scheibert, J., Leurent, S., Prevost, A., and Debrégeas, G. (2009). The role of fingerprints in the coding of tactile information probed with a biomimetic sensor. *Science*, **323**(5920), 1503–1506.
- SCHOTT Technical Glass Solutions GmbH (2020). Borofloat[®] 33 – optical properties.
- Serina, E. R., Mote, C. D., and Rempel, D. (1997). Force response of the fingertip pulp to repeated compression – effects of loading rate, loading angle and anthropometry. *Journal of Biomechanics*, **30**(10), 1035–1040.
- Shimoga, K. and Goldenberg, A. (1996). Soft robotic fingertips: Part II: Modeling and impedance regulation. *The International Journal of Robotics Research*, **15**(4), 335–350.
- Tang, W., Chen, N., Zhang, J., Chen, S., Ge, S., Zhu, H., Zhang, S., and Yang, H. (2015a). Characterization of tactile perception and optimal exploration movement. *Tribology Letters*, **58**(2), 28.
- Tang, W., Zhang, J., Chen, S., Chen, N., Zhu, H., Ge, S., and Zhang, S. (2015b). Tactile perception of skin and skin cream. *Tribology Letters*, **59**(1), 24.
- Taylor, N. A. and Machado-Moreira, C. A. (2013). Regional variations in transepidermal water loss, eccrine sweat gland density, sweat secretion rates and electrolyte composition in resting and exercising humans. *Extreme Physiology & Medicine*, **2**(1), 4.
- Tiwari, A., Miyashita, N., Espallargas, N., and Persson, B. N. J. (2018). Rubber friction: The contribution from the area of real contact. *The Journal of Chemical Physics*, **148**(22), 224701.
- Tomasi, C. and Kanade, T. (1991). Detection and tracking of point. *International Journal of Computer Vision*, **9**, 137–154.
- Tomlinson, S., Lewis, R., and Carré, M. (2009). The effect of normal force and roughness on friction in human finger contact. *Wear*, **267**(5), 1311–1318.
- Tomlinson, S. E., Lewis, R., Liu, X., Texier, C., and Carré, M. J. (2011). Understanding the friction mechanisms between the human finger and flat contacting surfaces in moist conditions. *Tribology Letters*, **41**(1), 283–294.

- Uematsu, M. and Frank, E. U. (1980). Static dielectric constant of water and steam. *Journal of Physical and Chemical Reference Data*, **9**(4), 1291–1306.
- Vallbo, A. B. and Johansson, R. S. (1984). Properties of cutaneous mechanoreceptors in the human hand related to touch sensation. *Human Neurobiology*, **3**(1), 3–14.
- van Dooren, M., de Vries, J. G.-J., and Janssen, J. H. (2012). Emotional sweating across the body: Comparing 16 different skin conductance measurement locations. *Physiology & Behavior*, **106**(2), 298–304.
- Warman, P. H. and Ennos, A. R. (2009). Fingerprints are unlikely to increase the friction of primate fingerpads. *Journal of Experimental Biology*, **212**(13), 2016–2022.
- Westling, G. and Johansson, R. (1984). Factors influencing the force control during precision grip. *Experimental brain research*, **53**(2), 277–284.
- Wiertlewski, M., Friesen, R. F., and Colgate, J. E. (2016). Partial squeeze film levitation modulates fingertip friction. *Proceedings of the National Academy of Sciences*, **113**(33), 9210–9215.
- Willemet, L., Kanzari, K., Monnoyer, J., Birznieks, I., and Wiertlewski, M. (2021). Initial contact shapes the perception of friction. *Proceedings of the National Academy of Sciences*, **118**(49).
- Winnick, M. (2016). Putting a finger on our phone obsession.
- Wu, J. Z., Dong, R. G., Rakheja, S., and Schopper, A. W. (2002). Simulation of mechanical responses of fingertip to dynamic loading. *Medical Engineering & Physics*, **24**(4), 253–264.
- Wu, J. Z., Krajnak, K., Welcome, D. E., and Dong, R. G. (2008). Three-dimensional finite element simulations of the dynamic response of a fingertip to vibration. *Journal of Biomechanical Engineering*, **130**(5).
- Xiao, S., Nie, J., Tan, R., Duan, X., Ma, J., Li, Q., and Wang, T. (2019). Fast-response ionogel humidity sensor for real-time monitoring of breathing rate. *Materials chemistry frontiers*, **3**(3), 484–491.
- Yeon, J., Kim, J., Ryu, J., Park, J.-Y., Chung, S.-C., and Kim, S.-P. (2017). Human brain activity related to the tactile perception of stickiness. *Frontiers in Human Neuroscience*, **11**, 8.
- Yeung, K. K., Huang, T., Hua, Y., Zhang, K., Yuen, M. M., and Gao, Z. (2021). Recent advances in electrochemical sensors for wearable sweat monitoring: A review. *IEEE Sensors Journal*.

Bibliography

- Yum, S.-M., Baek, I.-K., Hong, D., Kim, J., Jung, K., Kim, S., Eom, K., Jang, J., Kim, S., Sattorov, M., Lee, M.-G., Kim, S., Adams, M. J., and Park, G.-S. (2020). Fingerprint ridges allow primates to regulate grip. *Proceedings of the National Academy of Sciences*, **117**(50), 31665–31673.
- Zhai, H. and Maibach, H. I. (2001). Effects of skin occlusion on percutaneous absorption: an overview. *Skin Pharmacology and Physiology*, **14**(1), 1–10.
- Zhang, Z. (2000). A flexible new technique for camera calibration. *IEEE Transactions on Pattern Analysis and Machine Intelligence*, **22**, 1330–1334.
- Zigler, M. J. (1923). An experimental study of the perception of stickiness. *The American Journal of Psychology*, **34**(1), 73–84.